

LoCuSS: Comparison of Observed X-ray and Lensing Galaxy Cluster Scaling Relations with Simulations [★]

Y.-Y. Zhang^{1,2}, A. Finoguenov^{1,3}, H. Böhringer¹, J.-P. Kneib⁴, G. P. Smith⁵, R. Kneissl⁶, N. Okabe⁷ and H. Dahle⁴

¹ Max-Planck-Institut für extraterrestrische Physik, Giessenbachstraße, 85748 Garching, Germany

² Argelander-Institut für Astronomie, Universität Bonn, Auf dem Hügel 71, 53121 Bonn, Germany

³ University of Maryland, Baltimore County, 1000 Hilltop Circle, Baltimore, MD 21250, USA

⁴ OAMP, Laboratoire d'Astrophysique de Marseille, traverse du Siphon, 13012 Marseille, France

⁵ School of Physics and Astronomy, University of Birmingham, Edgbaston, Birmingham, B152TT, UK

⁶ Max-Planck-Institut für Radioastronomie, Auf dem Hügel 69, 53121 Bonn, Germany

⁷ Astronomical institute, Tohoku University, Aramaki, Aoba-ku, Sendai, 980-8578, Japan

Received 20/11/07 / Accepted 06/02/08

Abstract. The Local Cluster Substructure Survey (LoCuSS, Smith et al.) is a systematic multi-wavelength survey of more than 100 X-ray luminous galaxy clusters in the redshift range 0.14–0.3 selected from the ROSAT all sky survey. We used data on 37 LoCuSS clusters from the *XMM-Newton* archive to investigate the global scaling relations of galaxy clusters. The scaling relations based solely on the X-ray data ($S-T$, $S-Y_X$, $P-Y_X$, $M-T$, $M-Y_X$, $M-M_{\text{gas}}$, $M_{\text{gas}}-T$, $L-T$, $L-Y_X$ and $L-M$) obey empirical self-similarity and reveal no additional evolution beyond the large scale structure growth. They also reveal up to 17 per cent segregation between all 37 clusters and non-cool core clusters. Weak lensing mass measurements are also available in the literature for 19 of the clusters with *XMM-Newton* data. The average of the X-ray based mass to weak lensing mass ratio is 1.09 ± 0.08 , setting the limit of the non-thermal pressure support to 9 ± 8 per cent. The mean of the X-ray based mass to weak lensing mass ratio of these clusters is ~ 1 , indicating a good agreement between X-ray and weak lensing masses for most clusters, although with 31–51 per cent scatter. The scatter in the mass–observable relations ($M-Y_X$, $M-M_{\text{gas}}$ and $M-T$) is smaller using X-ray based masses than using weak lensing masses by a factor of 2. Using the scaled radius defined by the Y_X profile – $r_{500}^{Y_X, X}$, $r_{500}^{Y_X, wl}$ and $r_{500}^{Y_X, si}$, we obtain lower scatter in the weak lensing mass based mass–observable relations, which means the origin of the scatter is M^{wl} and M^X instead of Y_X . The normalization of the $M-Y_X$ relation using X-ray mass estimates is lower than the one from simulations by up to 18–24 per cent at 3σ significance. This is in good agreement with the $M-Y_X$ relation based on weak lensing masses, the normalization of the latter being ~ 20 per cent lower than the one from simulations at $\sim 2\sigma$ significance. Such difference between observations and simulations is also indicated in the $M-M_{\text{gas}}$ and $M-T$ relations. Despite the large scatter in the X-ray to lensing comparison, the agreement between these two completely independent observational methods is an important step towards controlling astrophysical and measurement systematics in cosmological scaling relations.

Key words. Cosmology: observations – Galaxies: clusters: general – X-rays: galaxies: clusters – (Cosmology:) dark matter – Gravitational lensing

1. Introduction

The gravitational growth of fluctuations in the matter density distribution can be traced by the evolution of the galaxy cluster mass function (e.g. Schuecker et al. 2003). The mass function of luminous galaxy clusters probes the cosmic evolution of large-scale structure (LSS) and is an extremely effective test of cosmological models. It is sensitive to the matter density, Ω_m , and the amplitude of the cosmic power spectrum on cluster scales, σ_8 (e.g. Schuecker et al. 2003).

The construction of the mass function of galaxy clusters for large cosmological cluster samples is based on robust calibration of cluster mass–observable scaling relations for representative galaxy cluster samples using reliable mass measurements (e.g. Reiprich & Böhringer 2002; Voit 2005; Stanek et al. 2006).

Deep X-ray observations using *XMM-Newton* and *Chandra* can recover precisely the intra-cluster medium (ICM) density and temperature distributions. *XMM-Newton* (also *Chandra*) allows us for the first time to measure mass distributions for relaxed nearby clusters with statistical uncertainties below 15 per cent up to r_{500} which yields a tight $M_{500}-T$ relation with only 8 per cent scatter (Arnaud et al. 2005). Using *Chandra* data, Vikhlinin et al. (2006a) measured precise mass distribu-

Send offprint requests to: Y.-Y. Zhang

[★] This work is based on observations made with the *XMM-Newton*, an ESA science mission with instruments and contributions directly funded by ESA member states and the USA (NASA).

tions up to radii of r_{2500} , which provides a tight $M_{2500}-T$ relation for relaxed nearby clusters with its scatter also within 8 per cent. However, relaxed clusters only represent a small fraction of the cluster population in the local Universe and an even smaller fraction at high redshifts (Jeltema et al. 2005; Smith et al. 2005; Vikhlinin et al. 2006b) and the cluster mass estimates from X-ray observations are limited by additional physical processes in the ICM. Recent simulations (e.g. Rasia et al. 2004, 2006; Nagai et al. 2007a) show that the X-ray total mass measured via hydrostatic equilibrium can be biased low by up to 20 per cent for nearby relaxed clusters and therefore the normalization of the mass–temperature relation can be biased low by up to 30 per cent. The bias is more significant (up to ~ 30 per cent) for un-relaxed clusters.

Gravitational lensing provides a direct probe of the total cluster mass without needing to invoke the symmetry and equilibrium assumptions required in the X-ray analysis. However lensing yields direct constraints on the mass projected along the line-of-sight through the cluster and may therefore be prone to projection effects. It is therefore very powerful to use both X-ray and lensing methods to measure cluster mass and thus investigate systematic uncertainties in mass measurements and their impact on cosmological parameter estimation. Early X-ray versus strong lensing mass comparisons revealed large discrepancies between the methods (Miralda-Escude & Babul 1995), which were subsequently attributed to the absence of a cool core in, and thus presumed more disturbed dynamical state of, the discrepant clusters (Allen 1998; Wu 2000). More recent analysis of *Chandra* and *Hubble Space Telescope* data suggest a picture that is broadly consistent with Allen (1998) in that disturbed, likely merging, clusters dominate the scatter in the mass-temperature relation for cluster cores ($R \leq 250$ kpc/h) when using lensing to infer cluster mass (Smith et al. 2003, 2005). Wide-field weak lensing studies of cluster scaling relations have to date generally lacked the statistical precision to investigate systematic differences between disturbed and undisturbed clusters (Bardeau et al., 2007; Pedersen & Dahle 2007; Zhang et al., 2007; Hoekstra 2007). However extending the mass range of lensing-based scaling relation studies down to groups has been shown to help overcome the large scatter when trying to measure the slope of, for example, the mass-temperature relation (Bergé et al. 2007).

In summary, credible cluster cosmology experiments require well calibrated measurements of the shape, scatter and evolution of the mass-observable scaling relations based on large statistical samples of clusters that are unbiased with respect to cluster morphology. Elimination of systematic uncertainties from this calibration demands that the cluster mass measurements are cross-checked between independent mass measurement techniques, including X-ray and lensing methods. The challenges for precision cluster cosmology on the per cent level are therefore as follows: (1) construction of large ($n_{\text{clus}} \gtrsim 100$) representative cluster samples, and (2) detailed high quality X-ray and lensing mass measurements of that sample as a basis for calibrating the mass-observable scaling relations. Despite recent progress on weak lensing searches for galaxy clusters (Wittman et al., 2006; Massey et al., 2007; Miyazaki et al., 2007), the most efficient method to construct

a homogeneous sample of massive clusters is to use all sky X-ray surveys. The main attractions of this approach are the well-defined sensitivity limit of such surveys and the minimal biases towards different cluster morphologies.

The Local Cluster Substructure Survey (LoCuSS, PI: G. P. Smith; Smith et al. in prep.) is a systematic multi-wavelength survey of galaxy clusters designed to tackle the problems outlined above. LoCuSS provides a morphology-unbiased sample of ~ 100 X-ray luminous galaxy clusters in the redshift range $0.14 \leq z \leq 0.3$ selected from the ROSAT All Sky Survey catalogs (Ebeling et al. 1998, 2000; Böhringer et al. 2004). Studies of the LoCuSS sample are in progress on (1) gravitational lens modeling of the mass distribution in the cluster cores, using data from our ongoing *Hubble Space Telescope* (HST) observing program (SNAP:10881, GO:11312; Hamilton-Morris et al., in prep.); (2) the scaling relation between cluster mass inferred from lensing and the Sunyaev-Zeldovich (SZ) effect Y -parameter (Marrone et al., in prep.); (3) the distribution of the luminosity gap statistic in $10^{15} M_{\odot}$ clusters (Khosroshahi et al., in prep.); (4) wide-field weak-lensing analysis of clusters observed with Suprime-CAM on Subaru (Okabe et al., in prep.). A wide variety of follow-up observations are also underway or imminent, including recent awards of 300 ks on *Chandra* (PID:9800372), 129 ks at $24 \mu\text{m}$ with *Spitzer* (PID:40872), 60 ks on GALEX (Cycle 4, Proposal # 90), and a 0.5 Msec Key Program on ESA’s Herschel. These space-based observations are supported by ongoing ground-based programs at Keck, VLT, Subaru, Palomar, NOAO and UKIRT.

The goal of this paper is to compare X-ray and lensing cluster mass measurements of LoCuSS clusters for which archival X-ray data are available from XMM-Newton, and weak lensing masses are available in the literature. As at the end of 2006, 37 LoCuSS clusters had sufficiently high quality archival XMM-Newton data to derive precise temperature distributions for statistically reliable X-ray mass estimates. Weak lensing mass measurements are also available in the literature for 19 of these clusters (including 7 duplicates): 10 clusters from CFH12k data (Bardeau et al., 2005; 2007); 15 clusters from observations at the Nordic Optical Telescope and UH 88in (Dahle 2006); one cluster, Abell 1689, has also been studied using both CFHT and Subaru data (Limousin et al., 2007; Halkola et al. 2006; Broadhurst et al., 2005). Weak lensing measurements for an enlarged sample of LoCuSS clusters are coming, based on high quality HST and Subaru data (Okabe et al., in prep.).

This paper is organised as follows. The XMM-Newton data quality and corresponding optimized reduction method are described in § 2. § 3 shows an empirical similarity of the X-ray scaling relations for our sample and the difference in the normalization between mass–observable relations from X-ray observations and simulations. In § 4, we used a new method to determine the radial scale ($r_{500}^{Y_X-X}$) to study the scaling relations, in which the scatter can be reduced. In § 5, we present X-ray versus weak lensing mass calibration using different mass definitions to look for the one which gives least scatter in the X-ray versus weak lensing mass comparison. § 6 describes the weak lensing mass based mass–observable relations and the difference in the normalization between the weak lensing mass based mass–observable relations for 19 LoCuSS clus-

ters and the relations from simulations. In § 7, we discuss the scatter and bias in weak lensing mass estimates, the cluster mass comparison between observations and simulations, and the variation of the amplitude of cosmic power spectrum with the mass calibration. We draw our conclusions in § 8. Unless explicitly stated otherwise, we adopt a flat Λ CDM cosmology with the density parameter $\Omega_m = 0.3$ and the Hubble constant $H_0 = 70 \text{ km s}^{-1} \text{ Mpc}^{-1}$. We adopt the solar abundance table of Anders & Grevesse (1989). Confidence intervals correspond to the 68 per cent confidence level. We apply the Orthogonal Distance Regression package (ODRPACK 2.01¹, e.g. Boggs et al. 1987) taking into account measurement errors on both variables to determine the parameters and their errors of the fitting throughout this paper. We use Monte Carlo simulations for the uncertainty propagation on all quantities of interest.

2. Data description and X-ray mass modeling

Achieving the goals of this paper (§ 1), specifically identifying systematic differences between mass measurement methods, rest on being able to measure statistically reliable cluster masses using X-ray data. For this, a precise temperature distribution measurement is required. In order to obtain temperature measurements with uncertainties of ~ 15 per cent for X-ray luminous galaxy clusters, we used the criterion of ~ 2000 net counts in the 2–7 keV band per bin (Zhang et al. 2006, 2007). We therefore require that the screened *XMM-Newton* data of each cluster have more than 4000 net counts in the 2–7 keV band after the subtraction of the renormalized blank sky background to ensure at least two bins to measure the temperature profile. Up to the end of 2006, 37 LoCuSS clusters in the *XMM-Newton* archives fulfill this criterion (Fig. A.1) and Table A.1, of which 9 clusters are part of the REFLEX-DXL sample (Zhang et al. 2004, 2006; Finoguenov et al. 2005), 12 clusters are from the LoCuSS Pilot Study sample (Zhang et al. 2007), and additionally 6 clusters are from the REXCESS sample (Böhringer et al. 2007; Pratt et al. 2007; Croston et al. 2007) respectively. Since the REFLEX-DXL, LoCuSS Pilot Study, and REXCESS samples are constructed as morphology-unbiased samples, our sample, as a collective sample of them only with a redshift cut, provides an approximately unbiased cluster population. This allows us to investigate (i) the systematics of both X-ray and weak lensing cluster mass estimates, and (ii) the morphology dependence of the segregation and scatter in the scaling relations.

All 37 LoCuSS clusters in the *XMM-Newton* archives were uniformly analyzed using the optimized reduction method developed for *XMM-Newton* observations for galaxy clusters at redshifts higher than 0.14 (so that the cluster X-ray emission covers less than half of the field of view, FOV) with more than 4000 net photons emitted from the cluster in the 2–7 keV band. More details about this method can be found in Zhang et al. (2007). The outermost annulus outside the truncation radius (8–8.33' or 9.2–10' depending on the truncation radius) was used to model the residual background. The XMMSAS v6.5.0 software was used for data reduction. We present the X-ray de-

termined cluster center and observational information of the sample of all 37 LoCuSS clusters in Table A.1.

In our X-ray mass modeling, we used the de-projected spectra to measure the spatially resolved radial temperature distribution. A double- β model is adopted to fit the the ICM density distribution as follows. Firstly, the slope parameter β is derived by the local fit of the density profile at outer radii ($> 0.5r_{500}$) by a single- β model. As the inner component of the ICM density distribution is insensitive to the slope, we fixed the slope parameter β and fit the ICM density distribution to derive the inner and outer core radii of a double- β model. As the slope is locally fitted using the outer radii, there should not be a significant bias due to the β steepening in our X-ray mass modeling. We therefore only show the mass distribution derived from the spatially resolved temperature and density distributions with no extrapolation to larger radii. With deeper observations, the slope of the temperature profile can be better determined, which will improve the precision of the mass estimate. The Monte-Carlo error estimation method used for the error propagation in our X-ray mass modeling accounts for this. More details about the X-ray mass modeling can be found in Appendix A.

3. X-ray scaling relations: an empirical similarity

This section describes the detailed modeling and analysis of the X-ray data. Readers interested solely in the X-ray/lensing comparison may wish to move straight to the summary in § 3.13, and continue from there.

For this sample the cluster masses are uniformly determined using *XMM-Newton* data. This guarantees minimum scatter due to the analysis method. The scaling relations are generally parameterized by a power law ($Y = Y_0 X^\gamma$). For each relation, we performed the fitting with both normalization and slope free. Scatter describes the dispersion between observational data and the best-fit values. The scatter in the scaling relations directly measures the degree of variation of ICM properties from the self-similar behavior. We list the best-fit power law and the scatter in Table 1. The ODRPACK package weights the errors of the data, and estimates the uncertainties of the normalization parameter.

To compare the normalization between our sample and the samples from other observations and simulations, we also performed the fitting with the fixed slopes to the values as used for their samples. The uncertainty in the difference of the normalization takes into account the errors of both normalization of the two scaling relations for comparison. Using a fixed slope might enlarge the segregation when the mass range is not the same for two samples.

Based on the least scattered relations, $M_{\text{gas}}-T$ and $L_{\text{bol}}-Y_X$, for our sample we checked the self-consistency of the shapes (slopes) of the remaining scaling relations. The resulting slopes generally appear consistent with the inferred slopes for our sample. This allows us to fix the slopes to the self-consistent values inferred from our sample and to study the segregation and scatter in the scaling relations due to different cluster populations.

¹ <http://www.netlib.org/odrpac/> and references therein

3.1. Cool cores and X-ray scaling relations

We investigated the structural similarity of the scaled profiles of the X-ray properties in Appendix B in order to optimize the definition of the cluster global temperature and luminosity to obtain least scattered X-ray scaling relations with a brief description as follows. The global temperature is derived by the volume average of the radial temperature profile limited to the radial range of $0.2-0.5r_{500}$ ($T_{0.2-0.5r_{500}} = \frac{\sum_{k=1,n}(T_k/V_k)}{\sum_{k=1,n}(1/V_k)}$) as listed in Table A.2, where T_k and V_k are the temperature and volume of the k th radial shell of all the shells (from 1st to n th) between $0.2 - 0.5r_{500}$. We used the values in Table 4 in Zhang et al. (2007), and found that the volume average of the radial temperature profile gives nearly the same value as the spectroscopic temperature with a spectroscopic temperature versus volume averaged temperature ratio of 0.98. According to simulations from Rasia et al. (2005), our temperature definition will be lower than the emission measured temperature by 20-30 per cent. The core radii populate a broad range of values up to $0.2 r_{500}$. With the bolometric X-ray luminosity including and excluding the $< 0.2r_{500}$ region (Table A.2), we show the normalized cumulative cluster number count as a function of the fraction of the luminosity attributed to the cluster core ($< 0.2r_{500}$) in Fig. B.7. Up to 80 per cent of the bolometric X-ray luminosity is contributed by the cluster core ($< 0.2r_{500}$). We therefore use the X-ray luminosity corrected for the cool core for the $R < 0.2r_{500}$ region ($L_{\text{bol}}^{\text{corr}}$ in Table A.2).

3.2. Mass versus temperature

Hereafter M_{500}^X denotes the total cluster mass derived from X-ray data at a density contrast of 500. In Fig. 2, we present the M_{500}^X-T relation for our sample and its best fit, which gives a slope of 1.65 ± 0.26 .

We also performed the fitting with the slope fixed to the values 1.49 and 1.489 (consistent with our fit 1.65 ± 0.26) as used in Arnaud et al. (2005) and Vikhlinin et al (2006a). Our M_{500}^X-T relation agrees (1 ± 7 per cent) with the $M-T$ relations for 13 low-redshift clusters ($z < 0.23$, 0.7–9 keV) using *Chandra* observations (Vikhlinin et al 2006a), and for 6 relaxed nearby clusters ($z < 0.15$, $T > 3.5$ keV) using *XMM-Newton* data (Arnaud et al. 2005), respectively. No evident evolution is found for the $M-T$ relation after the redshift evolution correction due to LSS growth (defined in Appendix B).

Under the assumption that the temperature is constant within the cluster, the M_{500}^X-T relation based on ROSAT observations and the temperature measurements from literature related to the HIFLUGCS sample (Reiprich & Böhringer 2002; Popesso et al. 2005; Chen et al. 2007) gives higher normalization by $\sim (40-50) \pm 20$ per cent than the M_{500}^X-T relation based on *Chandra/XMM-Newton* observations. As the temperature distribution is used in the mass modeling to obtain the *XMM-Newton/Chandra* results, the high normalization in the ROSAT results is most probably due to the isothermal assumption in the mass modeling. We fixed the slope to 1.48 as used for the hot clusters (> 3 keV) with ASCA measured temperature profiles in Finoguenov et al. (2001), and found the normalization is higher by 19 ± 21 per cent than the value in Finoguenov et

al. (2001). It indicates the importance of well defined global temperature based on a spatially resolved temperature profile on the scaling relation studies.

We also fixed the slope to 1.59 (consistent with our fit 1.65 ± 0.26), and found that the normalization of our X-ray $M-T$ relation is lower by 19 ± 6 per cent than the one from simulations (SPH code) including radiative cooling, star formation, and SN feedback in Borgani et al. (2004). This is similar to the finding in Nagai et al. (2007a) that the X-ray measured cluster masses within r_{500} are lower than the cluster masses from simulations.

The $M-T$ relation of our observations uses the temperature comparable to the spectral-like temperature. The $M-T$ relation from simulations in Borgani et al. (2004) uses the emission-weighted temperature. As Rasia et al. (2005) mentioned that the normalization of the $M-T$ relation from simulations in Borgani et al. (2004) is higher by ~ 30 per cent using the spectral-like temperature instead of the emission-weighted temperature, 19 ± 6 per cent gives the minimum difference between our observations and simulations in Borgani et al. (2004).

Evrard et al. (1996, emission weighted temperature) simulated ROSAT observations of 58 nearby clusters ($z \sim 0.04$, 1–10 keV), for which the normalization of the $M-T$ relation is higher by 40 ± 16 per cent than ours (with the slope fixed to 1.5). It might be due to the neglect of complex gas physics (e.g. radiative cooling, star formation and SN feedback) in their simulations.

3.3. Mass versus Y_X

Simulations (Kravtsov et al. 2006) indicate that the X-ray analog of the integrated SZ flux ($Y_X = M_{\text{gas}} \cdot T$) can be used as a robust low scatter cluster mass indicator with less scatter compared to other X-ray observables. Kravtsov et al. (2006, Fig. 7 in their paper; also see Table 4 in Nagai et al. 2007b) found the $M-Y_X$ relation for the sample in Vikhlinin et al. (2006a) confirms the low scatter and shows an empirical similarity. Maughan et al. (2007) investigated the $M-Y_X$ relation using *Chandra* observations and found that the scatter varies with the data quality. It is therefore important to calibrate the $M-Y_X$ relation and to check whether Y_X does show the least scatter as a mass proxy using high quality observations from *XMM-Newton*.

Many definitions of Y_X have been used (e.g. Arnaud et al. 2007). In this work, we systematically investigate the difference in the scaling relations and their scatter using all known definitions of Y_X .

We present the $M-Y_X$ relation for the sample in Fig. 1, in which the best fit gives a slope of 0.624 ± 0.061 , consistent with 0.526 ± 0.038 derived from *Chandra* data (see Fig. 7 in Kravtsov et al. 2006 and Table 4 in Nagai et al. 2007b). We fixed the slope to 0.526, and found an agreement (2 ± 12 per cent) of the normalization between $M-Y_X$ relations for our sample and theirs. With the slope fixed to 0.548, the normalization for our sample is higher than for the sample in Arnaud et al. (2007) by 6 per cent, which is also based on *XMM-Newton*

observations. There is no obvious evolution for the M – Y_X relation after the redshift evolution correction due to LSS growth. We found that the scatter in Y_X for M – Y_X is similar to the scatter in T for M – T . The comparison between our sample and the samples in Vikhlinin et al. (2006a), Maughan et al. (2007) and Arnaud et al. (2007) might indicate that the slope of the M – Y_X relation varies as a function of the mass range of the sample.

As Y_X appears to be a good mass proxy, the cluster mass can be estimated from Y_X via the M – Y_X relation. Hereafter such a mass estimate is called the Y_X inferred cluster mass, M^{Y_X} .

We also fixed the slope to 0.568 (consistent with our fit 0.624 ± 0.061) as obtained in simulations (Nagai et al. 2007b), and found the normalization of our X-ray M – Y_X relation is lower than the one in simulations from Nagai et al. (2007b, the mass–observable relation using the spectroscopic temperature and true mass; also see Kravtsov et al. 2006) including cooling and galaxy feedback by 18 ± 4 per cent. From simulations in Nagai et al. (2007b), the hydrostatic mass estimate is about 20% lower than the true mass, similar to the differences we observe. Here we compare our mass measurements with “the truth” from simulations rather than the hydrostatic masses derived from the simulations in Nagai et al. (2007b). In part this is because it gives a consistent basis upon which to compare lensing and X-ray masses with the simulations.

3.4. Mass versus gas mass

The total mass versus gas mass relation (M – M_{gas}) for our sample is shown in Fig. 1, giving a slope of 0.906 ± 0.078 , consistent with 0.811 ± 0.067 derived from *Chandra* data (Kravtsov et al. 2006, Nagai et al. 2007b). We fixed the slope to 0.811 as derived for the sample in Kravtsov et al. (2006), and found that the normalization of the M – M_{gas} relation for our sample agrees (2 ± 11 per cent) with theirs. No evident evolution is found for the M – M_{gas} relation after the redshift evolution correction due to LSS growth.

We also fixed the slope to 0.894 (consistent with our fit 0.906 ± 0.078) as derived in Nagai et al. (2007b), and found the normalization of our X-ray M – M_{gas} relation is lower than the one in simulations in Nagai et al. (2007b) by 13 ± 4 per cent.

3.5. Gas mass versus temperature

Fig. 3 shows the $M_{\text{gas},500}$ – T relation for our sample and its best fit giving a slope of 1.859 ± 0.187 .

We obtained a slope of 1.84 for the $M_{\text{gas},500}$ – T relation for the sample in Vikhlinin et al. (2006a) using the scaling relations in Kravtsov et al. (2006). We then fixed the slope to 1.84 (consistent with our fit 1.859 ± 0.187), and found that the $M_{\text{gas},500}$ – T relation for our sample agrees (3 ± 11 per cent) with their nearby relaxed cluster sample based on *Chandra* observations. No evident evolution is found for the M_{gas} – T relation after the redshift evolution correction due to LSS growth.

Castillo-Morales & Schindler (2003) investigated a sample of 10 nearby clusters ($0.03 < z < 0.09$, 4.7–9.4 keV) observed by ROSAT and ASCA. The normalization for their samples is higher by 19 ± 3 per cent (no errors available for the normaliza-

tion in Castillo-Morales & Schindler 2003) than ours with the slope fixed to 1.8 as used in their work. The $M_{\text{gas},500}$ – T relation in Mohr et al. (1999) is based on a flux-limited sample of 45 nearby clusters spanning a temperature range of 2–10 keV also observed by ROSAT and ASCA. Their normalization is higher than ours by 81 ± 7 per cent using their slope of 1.98. Chen et al. (2007) present the $M_{\text{gas},500}$ – T relation based on the non-cool core clusters (non-CCCs) with $T > 3$ keV in HIFLUGCS, in which the normalization is higher than ours by a factor of 2 with the slope fixed to 1.8. The difference in the normalization might be due to the difficulty of performing spatially resolved temperature measurements with ROSAT/ASCA data. At that time, one had to use the r_{500} defined from simulations (e.g. Evrard et al. 1996) which is larger than the value obtained from observations based on the radial temperature profile using *XMM-Newton* data.

We also fixed the slope to 1.8 (consistent with our fit 1.859 ± 0.187) as shown in Borgani et al. (2004), and found the normalization of our X-ray M_{gas} – T relation is lower than the one from simulations in Borgani et al. (2004, emission weighted temperature) by 7 ± 11 per cent. If only considering the massive systems, we observe a slightly smaller segregation between our observations and their simulations as shown in Fig. 3.

3.6. Luminosity versus Y_X

The L_{bol} – Y_X relation for this sample is shown in Fig. 3, with a best-fit slope of 0.951 ± 0.081 .

We fixed the slope to 0.94 (consistent with our fit 0.951 ± 0.081) as used in Maughan (2007), and found that the normalization for our sample is higher than for the sample of 116 massive clusters ($0.1 < z < 1.3$) in their work by 10 ± 4 per cent. Compared to the observational errors, there is no obvious evolution in the L_{bol} – Y_X relation after the redshift evolution correction due to LSS growth.

3.7. Luminosity versus temperature

The detailed calculation of the X-ray luminosity is described in Appendix B.4. The L – T relations and their best fits, giving slopes of 2.127 ± 0.323 for $L_{0.1-2.4}^{\text{corr}}-T$ and 2.614 ± 0.319 for $L_{\text{bol}}^{\text{corr}}-T$, are shown in Fig. 4.

The L – T relation has been thoroughly investigated for nearby cluster samples based on ROSAT and ASCA observations, for example, in (i) Markevitch (1998, 30 clusters, $0.04 < z < 0.09$, $T > 3.5$ keV), (ii) Arnaud & Evrard (1999, 24 clusters, $z < 0.37$, $T > 2$ keV), (iii) Reiprich & Böhringer (2002, in which the flux-limited morphology-unbiased sample HIFLUGCS was initially constructed and investigated. The fits used here are for the whole HIFLUGCS sample including groups), (iv) Ikebe et al. (2002, a flux-limited sample of 62 clusters, $z < 0.16$, 1–10 keV), and (v) Chen et al. (2007, HIFLUGCS).

The best-fit slope 2.614 ± 0.319 for the $L_{\text{bol}}^{\text{corr}}-T$ relation for our sample rules out the standard self-similar prediction $L \propto T^2$ at 2σ significance. The normalization for our sample agrees

with the normalization for the nearby samples using representative non-CCCs in Markevitch (1998) on 6 ± 11 per cent level with the slope fixed to 2.64, in Arnaud & Evrard (1999) on 4 ± 9 per cent level with the slope fixed to 2.88, and in Chen et al. (2007) on 13 ± 22 per cent level with the slope fixed to 2.78, respectively.

The normalization of the $L_{0.1-2.4\text{keV}}^{\text{corr}}-T$ relation for our sample is slightly lower than for the nearby samples in Markevitch (1998) by 13 ± 11 per cent with the slope fixed to 2.10, but shows an agreement with the sample in Ikebe et al. (2002) on 5 ± 38 per cent level with the slope fixed to 2.44.

The observed evolution in the $L-T$ relation is consistent with the prediction of the LSS growth and is therefore not seen on the corrected relations.

There is no significant difference between the normalization of the $L-T$ relations using ROSAT/ASCA data and XMM-Newton/Chandra data, which is not the case for the $M-T$ and $M_{\text{gas}}-T$ relations. The spatial resolution is of prime importance to get precise temperature gradient for a good X-ray mass measurements. However, L and T can be derived reliably without spatially resolved spectroscopy. Therefore the $L-T$ relation from ASCA/ROSAT is more likely to be in agreement with Chandra/XMM than mass-observable relations.

The normalization is higher by 41 ± 24 per cent using a fixed slope of 2.598 for $L_{0.1-2.4\text{keV}}^{\text{corr}}-T$ and by 36 ± 23 per cent with the slope fixed to 2.98 for $L_{\text{bol}}^{\text{corr}}-T$ for the HIFLUGCS sample in Reiprich & Böhringer (2002). The temperature can be biased low and the X-ray luminosity can be biased high for CCCs in the HIFLUGCS sample. At the same time both temperature and luminosity can be boosted high for merging systems. It is difficult to predict the combined effects without looking into the detailed temperature and density profiles for the HIFLUGCS sample.

3.8. Luminosity versus mass

The $L_{\text{bol}}^{\text{corr}}-M$ relation is shown in Fig. 2 giving a best-fit slope of 2.325 ± 0.701 . The scatter in the $L-M$ relation is much larger than the scatter in the other X-ray scaling relations for our sample.

The normalization of the $L-M$ relations for our sample is higher than for the HIFLUGCS sample based on ROSAT/ASCA observations (Reiprich & Böhringer 2002; Popesso et al. 2005; Chen et al. 2007) by a factor of ~ 2 . The difference in the normalization might be due to the isothermal assumption in their mass modeling and boosting effects due to CCCs in HIFLUGCS.

We also fixed the slope to 1.572 (smaller than our fit 2.325 ± 0.701) as derived from the $L_{\text{bol}}-T$ and $M-T$ relations in Borgani et al. (2004, emission weighted temperature), and found the normalization of our X-ray $L_{\text{bol}}-M$ relation is lower than the one from simulations in Borgani et al. (2004) by 18 ± 32 per cent.

3.9. r_{500} versus global temperature

The best fit for our sample gives $r_{500} = 10^{-0.38 \pm 0.07} T_{0.2-0.5r_{500}}^{0.60 \pm 0.08} E(z)^{-1}$ Mpc. Similar to the finding in Arnaud et al. (2005) observing $r_{500} \propto T^{0.50 \pm 0.05}$ for 6 relaxed nearby clusters ($z < 0.15$, 2–9 keV, $T > 3.5$ keV) using XMM-Newton data. Pacaud et al. (2007) found $r_{500} = 0.375(T/\text{keV})^{0.63} h_{73}(z)^{-1}$ Mpc based on the measurements in Finoguenov et al. (2001), which is in agreement with ours within the uncertainty.

3.10. Self-consistent scaling relations

As shown in Table 1, both $M_{\text{gas}}-T$ and $L_{\text{bol}}-Y_X$ relations show smaller scatter than the remaining scaling relations. The errors (10 per cent) of the slope parameters are also the smallest for these 2 relations compared to the other relations. We therefore checked the self-consistency of the empirical scaling relations based on these 2 relations ($M_{\text{gas}} \propto T^{1.859 \pm 0.187}$ and $L_{\text{bol}} \propto Y_X^{0.951 \pm 0.081}$) for our sample as follows.

The definition of the X-ray bolometric luminosity gives $L_{\text{bol}} \propto M_{\text{gas}}^2 T^{0.5} M^{-1}$. Combining with $L_{\text{bol}} \propto Y_X^{0.951}$, we derive $M_{\text{gas}}^2 T^{0.5} M^{-1} = (M_{\text{gas}} \cdot T)^{0.951}$. Given $M_{\text{gas}} \propto T^{1.859}$, the $M-T$ relation is $M \propto T^{1.499}$, and the $M-M_{\text{gas}}$ relation is $M \propto M_{\text{gas}}^{0.806}$, respectively.

Combining $M_{\text{gas}} \propto T^{1.859}$ and $M \propto T^{1.499}$ yields $M \propto Y_X^{0.524}$.

We obtain $L_{\text{bol}} \propto T^{2.719}$ on the basis of $L_{\text{bol}} \propto Y_X^{0.951}$ and $M_{\text{gas}} \propto T^{1.859}$, and $L_{\text{bol}} \propto M^{1.814}$ on the basis of $L_{\text{bol}} \propto T^{2.719}$ and $M \propto T^{1.499}$, respectively.

The slopes of the empirical scaling relations for our sample inferred from $M_{\text{gas}} \propto T^{1.859 \pm 0.256}$ and $L_{\text{bol}} \propto Y_X^{0.951 \pm 0.081}$ are in agreement with the best-fit slope values in Table 1. This indicates that our sample shows a self-consistent, empirical similarity in the scaling relations.

3.11. Cool core dependence of the normalization and scatter

Different cluster populations might show different normalization and scatter in the scaling relations. Most CCCs show simpler morphologies than non-CCCs, though this is not always the case, e.g. Abell 2390 (Allen et al., 2001; Swinbank et al., 2006). We checked the cool core dependence of the normalization and scatter using our sample. There is no significant bimodal distributions in the X-ray scaling relations. However, the CCCs and non-CCCs defined in Appendix A are still used to divide the sample into two subsets in order to quantify the segregation in the scaling relations due to cool cores. We fixed the slope parameters to the prediction in § 3.10 on the basis of $M_{\text{gas}} \propto T^{1.859 \pm 0.256}$ and $L_{\text{bol}} \propto Y_X^{0.951 \pm 0.081}$, and compared the normalization and scatter in the scaling relations between the whole sample and non-CCC² (Table 1). The normaliza-

² The CCC subsample only consists of 9 clusters as shown in Table B.1, which is statistically less sufficient compared to the non-CCC subsample to investigate the scatter, specially for the mean determined using a Gaussian model fit to the scatter histogram.

tion agrees to better than 17 per cent. The difference in scatter is most marked in the L – M relations (also cf. Chen et al. 2007). This may be due to the use of the hydrostatic equilibrium assumption for the determination of the X-ray cluster mass.

3.12. Mass–observable relations from X-ray observations and simulations

In the section we summarized the comparison between our sample and the samples from numerical simulations. Given a large variety of sources of the simulated data, we provide here a comparison between different methods, employed and also comment on the sensitivity of various predictions towards the adopted schemes. In simulations the measurements, such as the total mass and gas mass, are known precisely, some measurements, such as the X-ray luminosity, are calculated straight forward, and some measurements, such as the observed temperature, are method dependent. For example, Rasia et al. (2005) mentioned that the normalization of the M – T relation from simulations in Borgani et al. (2004) is higher by ~ 30 per cent using the spectral-like temperature instead of the emission weighted temperature. We used the following simulations in the comparison – Evrard et al. (1996, emission weighted temperature), Borgani et al. (2004, emission weighted temperature), and Nagai et al. (2007b, spectroscopic temperature). Further details regarding the numerical resolution, cosmological parameters, codes (grid versus particle) of simulations can be found in the papers cited above.

The normalization of the X-ray mass–observable relations is lower than the one from simulations (M – Y_X and M – M_{gas} in Nagai et al. 2007b; M – T and L_{bol} – M in Borgani et al. 2004, emission weighted temperature) by (1) 18 ± 4 per cent for M – Y_X , (2) 13 ± 4 per cent for M – M_{gas} , (3) 19 ± 6 per cent for M – T , and (4) 18 ± 32 per cent for L_{bol} – M , respectively.

The upward correction for the X-ray masses was suggested to be due to the steepening of the ICM density and temperature distributions assuming hydrostatic equilibrium by the comparison between *Chandra* observations (Kravtsov et al. 2006) and simulations (Nagai et al. 2007b). For our sample, the density profiles are well spatially resolved (> 100 bins) while the temperature profiles are poorly spatially resolved (≥ 2 bins). Luckily, the universal temperature profile in Vikhlinin et al. (2005) is based on the spatially well resolved temperature profiles for 13 low redshift galaxy clusters. We therefore investigated the steepening of the ICM density and temperature profiles in the outer region using our sample for the density distribution, and the sample in Vikhlinin et al. (2005) for the temperature distribution. We found that the mass can be higher by up to 25 per cent at r_{500} taking into account our ICM density steepening and the temperature steepening using the universal temperature profile in Vikhlinin et al. (2005) in the hydrostatic equilibrium assumption. One should be cautious with this point since we have almost no resolution on temperature profiles between $0.5r_{500}$ and r_{500} , where the temperature profile steepening can not be verified. One requires deep X-ray observations with 8–10 radial bins for the temperature measurements on the per cent precision level covering the area of more than $3/4r_{500}$

for a representative sample of more than 30 clusters to sufficiently verify the steepening of the ICM temperature profiles to investigate the bias.

3.13. Summary of the X-ray scaling relations

The above comparison of the X-ray scaling relations between this sample and published nearby and more distant samples shows that the evolution of the scaling relations can be accounted for by the redshift evolution due to LSS growth as given in Appendix B.

Based on our sample, the scatter in the X-ray mass–observable scaling relations is 7–40% (0.03–0.15dex).

The normalization agrees to better than 17 per cent for the scaling relations between the sample and the non-CCC subsample, with by far the worst case being the L_{bol} – M relation. In general, the slopes of the scaling relations (e.g. 1.859 ± 0.187 for M_{gas} – T) indicate the need for non-gravitational processes. This fits a general opinion that galaxy clusters show an empirical similarity.

The normalization of the X-ray mass–observable relations (i.e. M – T , M – Y_X and M – M_{gas}) for our sample is lower by 13–19 per cent with less than 6 per cent uncertainties than the relations from simulations (Borgani et al. 2004; Kravtsov et al. 2006; Nagai et al. 2007b).

4. $r_{500}^{Y_X, X}$ and the reduced scatter in the mass–observable relations and L_{bol} – Y_X relation

As shown in the left panels in Figs. 1–2, a few merging systems show significant deviation from the best-fit mass–observable relations. Since simulations (Nagai et al. 2007b) have shown that Y_X is claimed to be a good mass proxy even for merging clusters in which hydrodynamical equilibrium may be disturbed, we may improve the radial scaling by using a mass profile based on Y_X as a mass estimator. We used the following method to reduce the deviation in mass–observable relations for merging clusters by using the measured masses and X-ray observables at a new radial scale, $r_{500}^{Y_X, X}$.

The radial scale $r_{500}^{Y_X, X}$ is derived as follows. The procedure is initiated by deriving the best-fit M – Y_X relation using the X-ray masses M_{500} and Y_X parameters at the X-ray determined r_{500} for the 37 LoCuSS clusters with the slope fixed to 0.568, the prediction from simulations in Nagai et al. (2007). This best fit is used to calculate the mass profile $M^{Y_X}(r)$ from the profile $Y_X(r) = M_{\text{gas}}(r) * T_{0.2-0.5r_{500}}$. The radial scale, within which the density contrast derived from the mass profile $M^{Y_X}(r)$ is 500, is called r^{test} .

We re-fit the M – Y_X relation but using the X-ray masses and Y_X parameters at r^{test} for the 37 LoCuSS clusters with the fixed slope of 0.568. This best fit is used to re-derive the mass profile $M^{Y_X}(r)$ from the profile $Y_X(r)$, and $M^{Y_X}(r)$ can then be used to re-determine the radial scale r^{test} , within which the density contrast, derived from the mass profile $M^{Y_X}(r)$, is 500. We iteratively re-fit the M – Y_X relation using the X-ray masses and Y_X parameters at r^{test} , and re-determine the radial scale r^{test} using $M^{Y_X}(r)$ till the best fit of the M – Y_X relation does not vary any

more for our sample. The iteration is less than 10 times to fulfill the goal. The radial scale, $r_{500}^{Y_X, X}$, is the final r^{test} . The radial scale $r_{500}^{Y_X, X}$ and the X-ray mass and Y_X parameter at $r_{500}^{Y_X, X}$ for each cluster are listed in Table C.1.

In Figs. 5–6, we show the mass–observable scaling relations using the X-ray masses and observables at $r_{500}^{Y_X, X}$ for our sample. The deviation from the best fit is indeed reduced for merging systems.

The normalization of the mass–observable relations using X-ray masses and observables measured at $r_{500}^{Y_X, X}$ is lower than the one from simulations by, (1) 24 ± 3 per cent for M – Y_X , (2) 17 ± 4 per cent for M – M_{gas} , (3) 17 ± 5 per cent for M – T , and (4) 17 ± 31 per cent for L_{bol} – M , respectively. The difference in the normalization from X-ray observations and simulations does not vary significantly compared to the investigation using the X-ray masses and observables measured at r_{500} . This difference in the normalization is relatively independent of the scatter in the X-ray scaling relations.

5. Weak lensing versus X-ray mass comparison

Weak lensing and X-ray approaches provide independent cluster mass estimates. Comparison of X-ray and weak lensing masses is a powerful test of systematic errors in cluster mass determination. In total, weak lensing mass estimates are available in the literature for 19 of the total sample of 37 clusters. Ten of the 19 were observed over a wide-field (i.e. out to $R > r_{200}$) with CFHT by Bardeau et al., (2005; 2007 – hereafter the B07 sample).

Fifteen of the 19 were studied by Dahle (2006 – hereafter the D06 subsample) using the shear estimator based on the method in Kaiser (2000) but applied for small-field (2k chip, typically to $0.4r_{500}$) data from NOT and UH88. For this shear estimator, the polarizability includes calculating various derivatives with respect to galaxy flux, size and ellipticity. In practice, this is done numerically by binning the observed galaxies in a 3-D flux-size-shape space. For small-field data from NOT and UH88, there are only $\sim 10^3$ suitable background galaxies available for each cluster, which gives sparsely populated bins and thus introduces some additional uncertainties to the calculation of the polarizability. This shear estimator overcomes the problem by including galaxy information from a number of different fields before the binning and polarizability calculation, and produces more stable results. The overlap between the D06 and B07 samples is 6 clusters, giving a net literature-based weak lensing sample of 19 clusters.

The following sections describe the mass comparison using M_{500} (§ 5.1), and the mass measured at $r_{500}^{Y_X, X}$ (§ 5.2).

5.1. M_{500} comparison

To avoid the uncertainties caused by the extrapolation of the X-ray measured mass profile beyond r_{500} in the projection, we present the weak lensing versus X-ray mass calibration using spherical masses within radii of a density contrast of 500 (M_{500}). Hereafter M_{500}^{wl} denotes the weak lensing mass within weak lensing measured r_{500} . The average ratio of M_{500}^{wl} to M_{500}^{X} gives 1.7 ± 0.2 for the D06 subsample, and 1.1 ± 0.2 for the

B07 subsample, respectively. The better agreement obtained from B07 subsample arises from the large field of view of the CFHT data used by B07 (see above), in contrast the D06 data do not reach r_{500} , and thus the D06 masses require extrapolation. This shows the advantage of the LoCuSS project using uniformly observed and reduced data with large FOV to calibrate the weak lensing and X-ray masses and to investigate the scaling relations and their scatter.

The parameter Y_X shows less scatter than the X-ray mass as shown in the M – Y_X relation. To check whether the scatter in the weak lensing versus X-ray mass comparison is due to the scatter in X-ray masses, we replace the X-ray mass estimates by the mass given by Y_X at r_{500} and the X-ray M_{500} – Y_X relation, $M_{500}^{Y_X} = M(Y_X(r_{500}))$.

In the upper panels in Fig. 7, we show M_{500}^{wl} against M_{500}^{X} and $M_{500}^{Y_X}$, respectively, for the D06 and B07 subsamples. The scatter is reduced using $M_{500}^{Y_X}$ compared to the scatter using M_{500}^{X} . The slope of the best-fit power law is 1.61 ± 0.39 ($\chi^2 = 0.06/23$) for the M_{500}^{wl} versus M_{500}^{X} relation, and 1.57 ± 0.38 ($\chi^2 = 21.2/23$) for the M_{500}^{wl} versus $M_{500}^{Y_X}$ relation. The reduced χ^2 for the M_{500}^{wl} versus M_{500}^{X} relation is much smaller than 1, which might indicate the over-estimation of the errors of M_{500}^{X} . When the slope is fixed to 1, the normalization of the best-fit power law is 1.28 ± 0.14 for the M_{500}^{wl} versus M_{500}^{X} relation, and 1.21 ± 0.13 for the M_{500}^{wl} versus $M_{500}^{Y_X}$ relation, respectively. On average, the weak lensing masses (M_{500}^{wl}) are higher than the X-ray masses (M_{500}^{X}) by 28 ± 14 per cent according to the normalization. Systematically higher weak lensing masses than X-ray masses at r_{500} have also been reported by Mahdavi et al. (2007).

The weak lensing to X-ray mass ratio derived above takes into account the error weighting in both X-ray and weak lensing masses. The error in X-ray masses does not vary much from cluster to cluster. However, for a few clusters, the error in the weak lensing mass is a few times as large as for the remaining clusters. This may introduce a bias in the derived weak lensing to X-ray mass ratio using the above error weighted method. To avoid such a bias, we checked the mean of the M_{500}^{wl} to M_{500}^{X} ratios and M_{500}^{wl} to $M_{500}^{Y_X}$ ratios as follows. In the lower panels in Fig. 7, we show the normalized differential cluster number count as a function of the M_{500} ratio. It can be fitted by a Gaussian model $Y = Y_0 \exp(-((X-X_0)/W)^2/2)$. The histogram of $M_{500}^{\text{wl}}/M_{500}^{\text{X}}$ gives $Y_0 = 0.15 \pm 0.01$, $X_0 = 0.99 \pm 0.05$, and $W = 0.51 \pm 0.05$. And the histogram of $M_{500}^{\text{wl}}/M_{500}^{Y_X}$ gives $Y_0 = 0.15 \pm 0.01$, $X_0 = 1.00 \pm 0.05$, and $W = 0.45 \pm 0.05$. In logarithmic space, the best Gaussian fit provides mean values lower than the values obtained in linear space by ~ 15 per cent for both cases. In linear space, the mean is 0.99 with 51 per cent scatter in $M_{500}^{\text{wl}}/M_{500}^{\text{X}}$, and 1.00 with 45 per cent scatter in $M_{500}^{\text{wl}}/M_{500}^{Y_X}$, respectively. As shown in the lower part of the lower panels in Fig. 7, the discrepancy between M_{500}^{wl} and M_{500}^{X} (or $M_{500}^{Y_X}$) can be up to 5 times the errors of M_{500}^{wl} for individual clusters. To our surprise, the clusters in the tails of the Gaussian distribution show both pronounced mass discrepancies and very small errors in weak lensing masses. It indicates that the clusters showing large mass discrepancies may

be over-weighted in the determination of the weak lensing to X-ray mass ratio using the error weighted method. As a consequence, the deviation of the weak lensing to X-ray mass ratio from 1 can be biased high using the error weighted method. On the contrary, the Gaussian fit to the histogram of the weak lensing to X-ray mass ratio gives the value of the dominant population.

In the above test, we used the best-fit X-ray M – Y_X relation for our sample with the slope fixed to 0.568 predicted from simulations (Nagai et al. 2007b) to derive $M_{500}^{Y_X}$ from $Y_{X,500}$. We made an additional attempt to repeat such tests by using the best-fit X-ray M – Y_X relations for our sample with (i) a free slope, and (ii) the slope fixed to 0.524 as predicted from the empirical self-similarity of our sample described in § 3.10, respectively. The mean of the M_{500}^{wl} to $M_{500}^{Y_X}$ ratios varies within 14 per cent, and the scatter varies within 7 per cent in the tests via different X-ray M – Y_X relation. Within the scatter, it holds that the mean of the weak lensing to X-ray M_{500} ratio is about 1.

5.2. Mass comparison at $r_{500}^{Y_X,X}$

In the above mass comparison, we used M_{500} for X-rays taken at the X-ray determined r_{500} and M_{500} for weak lensing taken from the weak lensing determined r_{500} . This can introduce two sources of difference, (1) the normalization of the mass profile, and (2) the radius up to which the mass is integrated. To reduce such differences, we investigated the mass comparison using the masses measured at the same radius as follows.

Despite the mass comparison using both weak lensing masses and X-ray masses measured at the radial scale of $r_{500}^{Y_X,X}$, we also made a comparison the weak lensing mass estimates and the mass given by Y_X at $r_{500}^{Y_X,X}$ and the X-ray M_{500} – Y_X relation, $M^{Y_X}(r_{500}^{Y_X,X}) = M(Y_X(r_{500}^{Y_X,X}))$, as shown in Fig. 8. When the slope is fixed to 1, the normalization of the best-fit power law for the $M_{500}^{wl}(r_{500}^{Y_X,X})$ versus $M^X(r_{500}^{Y_X,X})$ relation is 1.09 ± 0.08 , and for the $M_{500}^{wl}(r_{500}^{Y_X,X})$ versus $M^{Y_X}(r_{500}^{Y_X,X})$ relation is 1.04 ± 0.08 , respectively. On average, the weak lensing masses, $M_{500}^{wl}(r_{500}^{Y_X,X})$, are higher than the X-ray masses, $M^X(r_{500}^{Y_X,X})$, by 9 ± 8 per cent according to the normalization. Following the arguments presented in Churazov et al. (2007), the current comparison limits the non-thermal pressure support to 9 ± 8 per cent according to the ratio between the weak lensing and X-ray mass estimates.

With a Gaussian fit $Y = Y_0 \exp^{-(X-X_0)/W)^2/2}$, the histogram of $M_{500}^{wl}(r_{500}^{Y_X,X})/M^X(r_{500}^{Y_X,X})$ gives $Y_0 = 0.19 \pm 0.02$, $X_0 = 1.16 \pm 0.04$, and $W = 0.42 \pm 0.04$. And the histogram of $M_{500}^{wl}(r_{500}^{Y_X,X})/M^{Y_X}(r_{500}^{Y_X,X})$ gives $Y_0 = 0.22 \pm 0.02$, $X_0 = 1.01 \pm 0.03$, and $W = 0.33 \pm 0.03$. The scatter is therefore reduced to 33–42 per cent compared to 45–51 per cent for $M_{500}^{wl}/M_{500}^{Y_X}$ and M_{500}^{wl}/M_{500}^X .

6. Weak lensing mass M_{500}^{wl} based mass–observable relations

We now investigate the scaling relations between weak lensing mass and four representative X-ray observable proxies of the cluster mass: (1) Y_X , which has been suggested as the

mass proxy with least scatter on the basis of simulations (e.g. Kravtsov et al. 2006), (2) gas mass, which is an observable almost independent of X-ray mass, (3) global temperature, and (4) X-ray bolometric luminosity. We present the mass–observable relations using weak lensing masses for the subsample of the 19 clusters on the right column of panels in Figs. 1–2.

6.1. Scatter and systematics

The scatter using weak lensing masses is larger than the scatter using X-ray masses by about a factor of 2 (Table 2). This difference is probably caused by a combination of (i) larger measurement errors on the weak lensing mass measurements than on the X-ray mass estimates, and (ii) possible under-estimation of the scatter in the X-ray scaling relation due to intrinsic correlation between the axes when both are based on the same dataset.

We also seek a physical origin of the scatter in the lensing relation, by dividing the clusters into single and merger X-ray morphologies (defined in Appendix A.2). The single clusters only show significantly less scatter in mass at fixed observable than the merger clusters in the luminosity–mass relation, the reduction in scatter being $\sim 50\%$. This indicates that, in general, merging systems introduce insignificant scatter in the weak lensing mass based mass–observable relations at r_{500} . The larger scatter in the luminosity–mass relation of merger clusters may indicate shock heating of gas in merger clusters, although it is odd that this effect does not also affect the mass–temperature relation. There is also no evidence for a difference in normalization between single and merger clusters in any of the scaling relations examined above except for the L_{bol} – M relation, showing 32 per cent difference. This might indicate that boost effects are significant on the X-ray luminosity than on the temperature for merging systems.

The scatter in the scaling relations is nearly symmetric using weak lensing masses irrespective of being classified as CCCs or non-CCCs (Figs. 1–2). The normalization is nearly the same using weak lensing masses between all 19 clusters and the non-CCC subsample, giving up to 7 per cent difference (i.e. 7 per cent difference in the L_{bol} – M relation). This indicates low systematics in the weak lensing mass based mass–observable scaling relations concerning being CCCs and non-CCCs.

6.2. Observations versus simulations

To study the difference in the normalization between the mass–observable relations using weak lensing masses and the one from simulations, we fixed the slope to the value derived from simulations and fitted the normalization for the 19 LoCuSS clusters.

6.2.1. First Attempt

First we use weak lensing masses computed within r_{500} derived from the lensing data with X-ray observables measured at the X-ray determined r_{500} .

We fixed the slope to 0.568 as obtained from simulations (Nagai et al. 2007b) for the M – Y_X relation, and found that the normalization using weak lensing masses is marginally lower than the one from simulations (AMR code) in Nagai et al. (2007b, also see Kravtsov et al. 2006) by 1 ± 10 per cent.

With the slope fixed to 0.894 predicted from simulations (Nagai et al. 2007b) for the M – M_{gas} relation, we found a marginally higher normalization of the M – M_{gas} relation using weak lensing masses than the one from simulations (AMR code) in Nagai et al. (2007b) by 3 ± 11 per cent.

Using the slope fixed to 1.59, we found that the normalization of the weak lensing mass based M – T relation is marginally higher by 4 ± 12 per cent than the one from simulations (SPH code) including radiative cooling, star formation, and SN feedback in Borgani et al. (2004).

The L_{bol} – M relation from simulations can be derived from the M – T and L_{bol} – T relations from simulations (SPH code) in Borgani et al. (2004), which shows a slope of 1.572. With the slope fixed to 1.572, we found the normalization of the L_{bol} – M relation using weak lensing masses is lower than the one from simulations by 52 ± 34 .

In summary, there is no statistically significant difference between the normalization of the observed and simulated relations when using lensing mass and X-ray observables derived from within r_{500} obtained from each respective dataset.

6.2.2. All measurements within $r_{500}^{Y_X, X}$

In § 6.2.1, the scatter in the weak lensing mass based scaling is so much larger than the difference in the normalization between observations and simulation. It is therefore not clear whether there is consistency between weak lensing mass based mass–observable relations and mass–observable relations from simulations. In Table 3, we present the best-fit normalization of weak lensing mass based mass–observable relations using the measurements at $r_{500}^{Y_X, X}$ listed in Table C.1. As shown in Figs. 9–10, the scatter is greatly reduced compared to the relations using the weak lensing masses M_{500}^{wl} at the weak lensing determined r_{500} and X-ray observables measured at the X-ray determined r_{500} .

As derived in § 4, the normalization of the mass–observable relations using X-ray masses and observables measured at $r_{500}^{Y_X, X}$ is lower than the one from simulations by, (1) 24 ± 3 per cent for M – Y_X , (2) 17 ± 4 per cent for M – M_{gas} , (3) 17 ± 5 per cent for M – T , and (4) 17 ± 31 per cent for L_{bol} – M , respectively. The normalization of the mass–observable relations using the weak lensing masses and X-ray observables measured at $r_{500}^{Y_X, X}$ is lower than the one from simulations by, i.e. (1) 18 ± 8 per cent for M – Y_X , (2) 17 ± 8 per cent for M – M_{gas} , (3) 6 ± 10 per cent for M – T , and (4) 25 ± 32 per cent for L_{bol} – M , respectively. At $r_{500}^{Y_X, X}$, we found a similar difference in the normalization between simulations and observations using either X-ray masses or weak lensing masses.

We also derived the weak lensing mass based and X-ray mass based mass–observable relations at $r_{500}^{Y_X, X}$ without the LSS evolution correction (Figs. 9–10). For M – Y_X , M – M_{gas} , the conclusions are relatively similar as for those with the LSS evolu-

tion correction as the LSS evolution correction has the same impact on both variables. However, the LSS evolution correction gives an opposite impact on L_{bol} and Y_X (also M). Therefore the L_{bol} – Y_X relation comparison between our sample and the sample in Maughan et al. (2007) shows that the LSS evolution correction is required to account for the evolutionary effect of the scaling relations and the scatter is significantly reduced using Y_X measured at $r_{500}^{Y_X, X}$ (Fig. C.5).

6.2.3. All measurements within $r_{500}^{Y_X, \text{wl}}$

We followed a similar procedure outlined in § 4, to derive iteratively the radius r_{500} for each cluster, but using the mass derived from the weak lensing data. Hereafter we call it $r_{500}^{Y_X, \text{wl}}$.

The procedure is initiated by deriving the mass profile $M^{Y_X}(r)$ from the profile $Y_X(r) = M_{\text{gas}}(r) * T_{0.2-0.5r_{500}}$ using the M_{500}^{wl} – Y_X relation (see Table 2). The radial scale, within which the density contrast derived from the mass profile $M^{Y_X}(r)$ is 500, is called r^{test} . We re-fit the M^{wl} – Y_X relation but using the weak lensing masses and Y_X parameters at r^{test} for the 37 LoCuSS clusters with the slope fixed to 0.568. This best fit is used to re-derive the mass profile $M^{Y_X}(r)$ from the profile $Y_X(r)$, and $M^{Y_X}(r)$ can then be used to re-determine the radial scale r^{test} , within which the density contrast, derived from the mass profile $M^{Y_X}(r)$, is 500. We iteratively re-fit the M^{wl} – Y_X relation using the weak lensing masses and Y_X parameters at r^{test} , and re-determine the radial scale r^{test} using $M^{Y_X}(r)$ till the best fit of the M^{wl} – Y_X relation does not vary any more for our sample. The radial scale, $r_{500}^{Y_X, \text{wl}}$, is the final r^{test} . The X-ray and weak lensing masses at $r_{500}^{Y_X, \text{wl}}$ are listed in Table. C.2. The X-ray mass and weak lensing mass based mass–observable relations at $r_{500}^{Y_X, \text{wl}}$ are shown in Figs. C.1–C.2 and Table 4. The normalization of the mass–observable relations using the X-ray masses and X-ray observables measured at $r_{500}^{Y_X, \text{wl}}$ is lower than the one from simulations by, i.e. (1) 20 ± 3 per cent for M – Y_X , (2) 16 ± 4 per cent for M – M_{gas} , (3) 18 ± 5 per cent for M – T , and (4) 13 ± 31 per cent for L_{bol} – M , respectively. The normalization of the mass–observable relations using the weak lensing masses and X-ray observables measured at $r_{500}^{Y_X, \text{wl}}$ is lower than the one from simulations by, i.e. (1) 17 ± 8 per cent for M – Y_X , (2) 14 ± 8 per cent for M – M_{gas} , (3) 14 ± 10 per cent for M – T , and (4) 9 ± 32 per cent for L_{bol} – M , respectively.

6.2.4. All measurements within $r_{500}^{Y_X, \text{si}}$

We also derived r_{500} , the radius by combing the $Y_X(r)$ profile with the M – Y_X relation from simulations in Nagai et al. (2007b). The M_{500} – Y_X relation in Nagai et al. (2007b) can be used to derive the mass profile $M^{Y_X}(r)$ from the profile $Y_X(r) = M_{\text{gas}}(r) * T_{0.2-0.5r_{500}}$. The radius, within which the density contrast derived from the mass profile $M^{Y_X}(r)$ is 500, is the radial scale. Hereafter we call it $r_{500}^{Y_X, \text{si}}$. The X-ray and weak lensing masses at $r_{500}^{Y_X, \text{wl}}$ are listed in Table. C.3. The X-ray mass and weak lensing mass based mass–observable relations at $r_{500}^{Y_X, \text{si}}$ are shown in Figs. C.3–C.4 and Table 5. The normalization of the mass–observable relations using the X-ray masses and X-ray observables measured at $r_{500}^{Y_X, \text{si}}$ is lower than

the one from simulations by, i.e. (1) 15 ± 3 per cent for $M-Y_X$, (2) 16 ± 5 per cent for $M-M_{\text{gas}}$, (3) 8 ± 5 per cent for $M-T$, and (4) 26 ± 31 per cent for $L_{\text{bol}}-M$, respectively. The normalization of the mass–observable relations using the weak lensing masses and X-ray observables measured at $r_{500}^{Y_X, \text{si}}$ is lower than the one from simulations by, i.e. (1) 15 ± 8 per cent for $M-Y_X$, (2) 21 ± 8 per cent for $M-M_{\text{gas}}$, (3) 6 ± 10 per cent for $M-T$, and (4) 25 ± 32 per cent for $L_{\text{bol}}-M$, respectively.

We thus draw similar conclusions concerning the scatter and normalization in the mass–observable relations using the weak lensing masses at $r_{500}^{Y_X, \text{wl}}$ and $r_{500}^{Y_X, \text{si}}$, respectively, as for those measured at $r_{500}^{Y_X, X}$. As precisely shown above, the normalization of the $M-Y_X$, $M-M_{\text{gas}}$, and $M-T$ relations using X-ray mass estimates is lower than the values from simulations by ~ 20 per cent at 3σ significance. In good agreement, these relations based on weak lensing masses also show lower normalization by ~ 20 per cent than the values from simulations but at $\sim 2\sigma$ significance.

In Fig. C.5, we also summarize the luminosity– Y_X relations at $r_{500}^{Y_X, X}$, $r_{500}^{Y_X, \text{wl}}$ and $r_{500}^{Y_X, \text{si}}$. The upper panels show that the LSS evolution correction accounts for the segregation of the Luminosity versus Y_X relations between cluster samples at different redshifts.

7. Discussion

7.1. Scatter and bias in weak lensing mass estimates

Since we observed a large scatter in weak lensing masses for the sample, we summarize the possible sources which can enlarge scatter in weak lensing mass estimates as follows.

(1) Accuracy of the faint galaxy shape measurements. Residuals in the removal of the point spread function (PSF) can masquerade as spurious shear signal, and/or introduce strong systematic errors, often referred to as B-models. Future LoCuSS weak lensing studies will use multiple shape measurement techniques to validate the fidelity of the PSF removal.

(2) Size of FOV. Ideally the FOV should extend beyond the virialized region of each cluster, which for a $10^{15} M_{\odot}$ cluster at $z \approx 0.2$ corresponds to $r_{200} \approx 2.0$ Mpc, or $\gtrsim 10'$. Small FOV weak lensing observations typically incur systematic errors in cluster mass determination due to the mass-sheet degeneracy and the need to extrapolate the observed shear signal out to larger radii. Dahle’s (2006) data are a good example of this; the NOT and UH 88in observations reach a maximum radius of just $\sim 7'$. In contrast, the LoCuSS pilot study used wide field data from CFHT (Bardeau et al. 2007), and LoCuSS is using Suprime-CAM on Subaru to make weak lensing measurements (Okabe et al., in prep.) – both reach out to $r \gtrsim 15'$. This will therefore not be a major concern for future LoCuSS papers.

(3) Accuracy of the background galaxy redshifts. The weak lensing mass estimate depends on the assumed redshift distribution of background galaxies, including the extent to which the background galaxy catalog is contaminated by faint cluster members and foreground galaxies. Several color-selection techniques have been developed recently (Broadhurst et al. 2005; Limousin et al. 2007) to deal with this issue. We will

apply these methods within LoCuSS weak lensing analysis and explore refined techniques to measure reliable photometric redshifts to minimize contamination of the shear catalogs.

(4) Projection of LSS. The scatter in the weak lensing masses could be slightly boosted by effects of projection due to LSS. For example, Hoekstra (2003) investigated effects of uncorrelated LSS on weak lensing mass measurements, showing that the accuracy of the measured mass of an NFW model does not improve once the outer radius for the fitting reaches the angular scale $\sim 15'$. Fortunately, the LoCuSS clusters are at redshift around 0.2, which places their virial radii at $r \lesssim 13'$. A similar investigation of the impact of correlated LSS is also required.

(5) Mass models. The weak lensing mass measurements using a tangential shear fitting are dependent on the assumed mass model, e.g. NFW model or SIS model. Usually an NFW model is considered to be more representative for the mass distribution in clusters than an SIS model. However, for some clusters, especially merging clusters, a NFW model is not favored statistically, and the SIS model has only been ruled out at large significance in a small number of cases (e.g. Kneib et al., 2003). LoCuSS weak lens modeling will test for the presence of substructures and attempt to fit multi-component models. The superb image quality of Subaru, and consequently higher number density of background galaxies will also increase the probability that we can discriminate between NFW and SIS models.

(6) Effects of triaxiality and interior substructures. Clowe et al. (2004) investigated effects of cluster triaxiality and substructures on the mass measurements and found that the triaxiality is more dominant. The value of r_{200} obtained by fitting the shear profile with an NFW model can vary by 10–15 per cent due to different projection, which corresponds to a mass (M_{200}) change of ~ 40 per cent. King et al. (2001) show that the mass measurement can be affected by interior substructures by up to 10 per cent.

7.2. Cluster mass comparison between observations and simulations

The cluster mass estimates using different approaches can be different as e.g. boost effects caused by merging systems might be different on the X-ray and weak lensing masses. For the purpose of precise cluster cosmology, one requires accurate knowledge of the systematics in X-ray cluster mass estimates and weak lensing cluster mass estimates and the difference between cluster mass estimates from simulations and observations.

Despite the larger individual measurement uncertainties in weak lensing masses, the normalization agrees between mass–observable relations using X-ray mass estimates and weak lensing mass estimates. The mean of the weak lensing to X-ray mass ratios is about 1 with up to 51 per cent scatter (Fig. 7 and Fig. 8).

Therefore the X-ray and weak lensing approaches provide a very valuable tool to cross calibrate the normalization and to constrain the systematics of the mass–observable relations. The systematics in the calibration of cluster mass estimates can

be reduced by using a sufficiently large sample of galaxy clusters with good statistic. The average of the weak lensing versus X-ray mass discrepancy is about two times the errors of the weak lensing masses (Fig. 7). This indicates either that the true errors in the weak lensing masses might be two times as large as the value quoted or that the difference is a real discrepancy. Therefore, one really needs a sufficiently large sample of galaxy clusters with both X-ray and weak lensing mass measured by large FOV observations to reduce the scatter in weak lensing mass estimates. This point will be more obvious with the progress of the LoCuSS project – the completion of the X-ray (*XMM-Newton*) and weak lensing (HST and Subaru) observations.

At the radial scale of $r_{500}^{Y_X, X}$, both the X-ray determined masses and the weak lensing determined masses systematically lie below the prediction from the mass–observable relations (i.e. $M-Y_X$, $M-M_{\text{gas}}$ and $M-T$) from simulations (Borgani et al. 2004; Kravtsov et al. 2006; Nagai et al. 2007b) by up to ~ 20 per cent with $\sim 3\sigma$ significance for the X-ray masses and $\sim 2\sigma$ significance for the weak lensing masses (Figs. 5–6, Figs. C.1–C.4). If one believes that the two independent approaches, weak lensing and X-ray, give reliable mass estimates, more real physics has to be included in simulations to reproduce the real galaxy clusters. This can be further verified by comparing the mass–observable relations between simulations and observations using a sufficiently large sample of galaxy clusters with both X-ray and weak lensing mass measurements. Since the difference in the normalization is only up to 20 per cent between mass–observable relations from observations and simulations, it is important to pursue a few per cent level systematics in the mass estimates. Therefore one has to improve the statistic for both simulation and observational samples by using a large sample (e.g. ~ 100 galaxy clusters). And one also has to reduce the errors in observations by using both (1) deep X-ray observations (e.g. an accuracy of the ICM temperature measurements on the per cent level precision for 8–10 radial bins) performed with a large FOV (e.g. covering the area of more than r_{500}), and (2) weak lensing observations performed with an instrument with a good PSF and a large FOV (e.g. covering the area of more than r_{200}) together with a photo-z database to characterize the background source galaxy redshift distribution.

7.3. Mass calibration and σ_8

Based on (1) the number density of clusters with $T > 6$ keV (Henry 2004, Ikebe et al. 2002) and (2) three bins of the cluster density with certain velocity dispersion from Rines et al (2007), Evrard et al. (2007) found a high amplitude of cosmic power spectrum, $S_8 = \sigma_8(\Omega_m/0.3)^{0.35} = 0.8$ using the Mass–temperature relation ($M'-T'$) from simulations combined with the gas mass–temperature relation ($M'_{\text{gas}}-T'$) from ROSAT and ASCA observations in Mohr et al. (1999) also regarding massive clusters in the similar temperature range. Our comparison shows that the normalization of the mass–temperature relation in Evrard et al. (1996) is higher than ours (M'_{500}^X-T) by 40 per cent, and the normalization of the gas mass–temperature rela-

tion in Mohr et al. (1999) is higher than ours ($M_{\text{gas},500}-T$) by 81 per cent. The gas mass to mass ratio in Evrard et al. (2007) is $M'_{\text{gas}}/M' = (1.81/1.4) \times M_{\text{gas}}/M$. According to the gas mass to mass ratio, $M'_{\text{gas}}/M' = 0.083 h_{70}^{-1.5} S_8'^{-5/3}$, in Evrard et al. (2007), we obtained $M_{\text{gas}}/M = 0.083 \times (1.4/1.81) h_{70}^{-1.5} S_8^{-5/3}$. For our sample, we then found $S_8 = 0.857174 S_8'$, where S_8' is 0.8 for the sample in Evrard et al. (2007). We thus obtained $S_8 = 0.69$ for our sample. The X-ray mass calibration using M'_{500}^X for our sample supports a lower amplitude of cosmic power spectrum on the basis of the comparison between observations and simulations.

To be conservative, we repeated the above calculation using the mass–temperature and gas mass–temperature relations at the radius $r_{500}^{Y_{X,si}}$, which is determined by our Y_X profile and the mass– Y_X relation from simulations in Nagai et al. (2007b). In this case, the normalization of the mass–temperature relation in Evrard et al. (1996) is higher than ours by 28 per cent, and the normalization of the gas mass–temperature relation in Mohr et al. (1999) is higher than ours by 58 per cent. Therefore the gas mass to mass ratio in Evrard et al. (2007) is $M'_{\text{gas}}/M' = (1.58/1.28) M_{\text{gas}}/M$. According to the gas mass to mass ratio, $M'_{\text{gas}}/M' = 0.083 h_{70}^{-1.5} S_8'^{-5/3}$, in Evrard et al. (2007), we obtained $M_{\text{gas}}/M = 0.083 \times (1.28/1.58) h_{70}^{-1.5} S_8^{-5/3}$. For our sample, we then found $S_8 = 0.88 S_8' = 0.70$.

Assuming weak lensing masses agree better with cluster masses from simulations, we also derived the S_8 parameter using the weak lensing mass based mass–temperature relation ($M'_{500}^{wl}-Y_X$) with the slope fixed to 1.5, which normalization is $4.49 \times 10^{13} M_\odot$. It gives $S_8 = 0.77$, similar to the value obtained from simulations in Evrard et al. (2007).

The above three experiments show the importance of the calibration of the scaling relations for the cluster cosmology. Depending on the mass calibration (e.g. via X-ray or weak lensing approach) the derived value of the amplitude of cosmic power spectrum varies by 10 per cent between 0.69 and 0.77 for our sample.

8. Summary and conclusions

We performed a systematic analysis to measure the X-ray quantities based on *XMM-Newton* observations for a sample of 37 LoCuSS clusters. We investigated (1) the empirical similarity of the X-ray scaling relations, (2) the scatter in X-ray and weak lensing mass estimates, (3) the difference in the normalization between mass–observable relations from observations (using X-ray masses and weak lensing masses, respectively) and simulations, and (4) the impact of the mass calibration on the determination of the amplitude of cosmic power spectrum. We summarize the main conclusions as follows.

(i) The self-consistent X-ray scaling relations for our sample support an empirical similarity for massive galaxy clusters. The X-ray scaling relations of our sample show no evident evolution compared to the nearby and more distant samples after the redshift evolution correction due to LSS growth. Specially, the X-ray $M-T$ relations agree on 1 per cent level between our

sample and the samples in Arnaud et al. (2005) and Vikhlinin et al. (2006a).

The cluster cores ($< 0.2r_{500}$) contribute up to 80 per cent to the bolometric X-ray luminosity. Using X-ray luminosity corrected for the cool core and temperature excluding the cool core, leads both to less scatter (7–40 per cent) in the X-ray scaling relations and to better than 17 per cent agreement of the normalization between the sample and the non-CCC sub-sample.

(ii) Using a Gaussian fit to the histogram of the weak lensing to X-ray M_{500} ratios, the mean weak lensing to X-ray M_{500} ratios is about 1, indicating a good agreement between X-ray and weak lensing mass estimates for most clusters. Therefore the weak lensing approach can be a very valuable tool to cross calibrate the systematics in cluster mass estimates and the normalization of the mass–observable relations together with the X-ray approach. The comparison between weak lensing and X-ray mass estimates shows a large scatter of the individual results. The most robust way to characterize this scatter is by the width of the Gaussian fit to the distribution of deviations which is 31–51 per cent. The large scatter is mostly due to uncertainties in the weak lensing mass caused in part by the LSS into which the clusters are embedded. For the purpose of precise cosmology, one requires a sufficiently large sample with both X-ray and weak lensing measurements to verify (1) the scatter in X-ray and weak lensing mass estimates on a few per cent level precision, and (2) the difference in the normalization between mass–observable relations between observations and simulations on per cent level accuracy.

(iii) The scatter in the mass–observable relations is larger using weak lensing masses than using X-ray masses by a factor of 2. However, the scatter using weak lensing masses is irrespective to being classified as CCCs and non-CCCs, or as “single”s and “merger”s. Using our method, we can define a radial scale $r_{500}^{Y_X, X}$, which can not only reduce the scatter in the mass–observable scaling relations, but also provide consistency between weak lensing mass based and X-ray mass based mass–observable scaling relations.

(iv) The X-ray mass estimates are about 20 per cent lower than the prediction of the mass–observable relations (i.e. $M-Y_X$, $M-M_{\text{gas}}$ and $M-T$) from simulations with $\sim 3\sigma$ significance. The comparison between the observed mass-observable relations (i.e. $M-Y_X$, $M-M_{\text{gas}}$ and $M-T$ at $r_{500}^{Y_X, X}$, $r_{500}^{Y_X, \text{wl}}$ or $r_{500}^{Y_X, \text{si}}$) and the relations from simulations (Borgani et al. 2004; Kravtsov et al. 2006; Nagai et al. 2007b) shows that weak lensing mass estimates, similar to X-ray mass estimates, are about 20 per cent lower than the cluster masses predicted by the mass–observable relations from simulations, but with $\sim 2\sigma$ significance. Since the X-ray and weak lensing approaches are independent, this might indicate that more complex physics is required in simulations to reproduce the real physics in galaxy cluster.

(v) With a fixed slope to 1, the normalization of the best-fit power law for the $M^{\text{wl}}(r_{500}^{Y_X, X})$ versus $M^X(r_{500}^{Y_X, X})$ relation is 1.09 ± 0.08 . On average, the weak lensing masses, $M^{\text{wl}}(r_{500}^{Y_X, X})$,

are higher than the X-ray masses, $M^X(r_{500}^{Y_X, X})$, by 9 ± 8 per cent according to the normalization. Following the arguments presented in Churazov et al. (2007), the current comparison limits the non-thermal pressure support to 9 ± 8 per cent according to the ratio between the weak lensing and X-ray mass estimates.

(vi) Depending on the mass calibration (e.g. via X-ray or weak lensing approaches), the derived value of the amplitude of cosmic power spectrum varies by 10 per cent between 0.69 and 0.77 for our sample.

Since the weak lensing mass determination is expected to be unbiased on average for a large sample of clusters, it is also very important to compare the agreement between lensing and X-ray mass for the sample average. We find that the results are consistent with an agreement of both methods. But different approaches to characterize the distribution of the deviation gives slightly different results. Taking these differences as a very conservative measure of systematic uncertainties we conclude that the two methods of mass determination agree within an uncertainty of less than 20 per cent for the sample average.

It is clear from this result that the latter conclusion, which is very important for the cosmological application of clusters, will benefit very much from an increase of the sample size, in addition to the currently happening improvements of lensing mass determinations. The present paper therefore highlights the crucial importance of the completion of the entire LoCuSS sample, which is planned to comprise in the end about 100 clusters.

Acknowledgements. The *XMM-Newton* project is an ESA Science Mission with instruments and contributions directly funded by ESA Member States and the USA (NASA). The *XMM-Newton* project is supported by the Bundesministerium für Wirtschaft und Technologie/Deutsches Zentrum für Luft- und Raumfahrt (BMWI/DLR, FKZ 50 OX 0001) and the Max-Planck Society. We acknowledge the anonymous referee for very useful suggestions led to improvement in our understanding. YYZ acknowledges G. W. Pratt, A. Vikhlinin, T. J. Ponman, A. E. Evrard, T. H. Reiprich, A. Babul, O. Czoske, P. Mazzotta, G. Hasinger, and D. Pierini for useful discussions. YYZ acknowledges support from the German BMBF through the Verbundforschung under grant No. 50 OR 0601 and MPG. AF acknowledges support from BMBF/DLR under grant No. 50 OR 0207 and MPG. HB and AF acknowledge support through the funding of the DfG for the Excellence Cluster Universe EXC153. GPS acknowledges support from a Royal Society University Research Fellowship. NO acknowledges Grants-in-Aid for the 21st Century COE Program “Exploring New Science by Bridging Particle-Matter Hierarchy” at Tohoku University, funded by the Ministry of Education, Science, Sports and Culture of Japan.

References

- Allen, S. W. 1998, *MNRAS*, 296, 392
- Allen, S. W., Schmidt, R. W., & Fabian, A. C. 2001, *MNRAS*, 328, L37
- Allen, S. W., Schmidt, R. W., & Fabian, A. C. 2002, *MNRAS*, 334, L11
- Allen, S. W., Schmidt, R. W., Ebeling, H., Fabian, A. C., & van Speybroeck, L. 2004, *MNRAS*, 353, 457

- Anders, E., & Grevesse, N. 1989, *Geochimica et Cosmochimica Acta*, 53, 197
- Arnaud, M., & Evrard, A. E. 1999, *MNRAS*, 305, 631
- Arnaud, M., Aghanim, N., & Neumann, M. 2002, *A&A*, 389, 1
- Arnaud, M., Pointecouteau, E., & Pratt, G. W. 2005, *A&A*, 441, 893
- Arnaud, M., Pointecouteau, E., & Pratt, G. W. 2007, *A&A*, submitted
- Bahcall, N. A. 1999, *Formation of Structure in the Universe*, ed. J. P. Ostriker & A. Dekel, Cambridge University Press, 135
- Bardeau, S., Kneib, J.-P., Czoske, O., et al. 2005, *A&A*, 434, 433
- Bardeau, S., Soucaill, G., Kneib, J.-P., et al. 2007, *A&A*, 470, 449
- Berg/e, J.; Pacaud, F.; R'efr'egier, A, et al. 2007, *MNRAS*, submitted, astro-ph/0712.3293
- Boggs, P. T., Byrd, R. H., & Schnabel, R. B. 1987, *SIAM J. Sci. Stat. Comput.*, 8(6), 1052
- Böhringer, H., Schuecker, P., Guzzo, L., et al. 2004, *A&A*, 425, 367
- Böhringer, H., Schuecker, P., Pratt, G. W., et al. 2007, *A&A*, 469, 363
- Borgani, S., Murante, G., Springel, V., et al. 2004, *MNRAS*, 348, 1078
- Broadhurst, T., Takada, M., Umetsu, K., et al. 2005, *ApJ*, L619, 143
- Bryan, G. L., & Norman, M. L. 1998, *ApJ*, 495, 80
- Castillo-Morales, A., & Schindler, S. 2003, *A&A*, 403, 433
- Cavaliere, A., & Fusco-Femiano, R. 1976, *A&A*, 49, 137
- Chen, Y., Reiprich, T. H., Böhringer, H., Ikebe, Y., & Zhang, Y.-Y. 2007, *A&A*, 466, 805
- Churazov E., Forman W., Vikhlinin A., et al. 2007, *MNRAS*, in press, astro-ph/0711.4686
- Clowe, D., & Schneider, P. 2002, *A&A*, 395, 385
- Clowe, D., De Lucia, G., & King, L. 2004, *MNRAS*, 350, 1038
- Cohn, J. D. & White, M. 2005, *Astroparticle Physics*, 24, Issue 4-5, 316
- Croston, J. et al. 2007, *A&A*, to be submitted
- Dahle, H., 2006, *ApJ*, 653, 954
- De Grandi, S., & Molendi, S. 2002, *ApJ*, 567, 163
- Dickey, J. M., & Lockman, F. J. 1990, *ARA&A*, 28, 215
- Dunn, R. J. H., & Fabian, A. C. 2006, *MNRAS*, 373, 959
- Ebeling, H., Edge, A. C., Böhringer, H., et al. 1998, *MNRAS*, 301, 881
- Ebeling, H., Edge, A. C., Allen, S. W., et al. 2000, *MNRAS*, 318, 333
- Ettori, S., Fabian, A. C., Allen, S. W., & Johnstone, R. M. 2002, *MNRAS*, 331, 635
- Ettori, S., Tozzi, P., & Rosati, P. 2003, *A&A*, 398, 879
- Evrard, A. E., Metzler, C. A., & Navarro, J. F. 1996, *ApJ*, 469, 494
- Evrard, A. E., Bialek, J., Busha, M., et al. 2007, *ApJ*, submitted, astro-ph/0702241
- Finoguenov, A., Reiprich, T. H., & Böhringer, H. 2001, *A&A*, 368, 749
- Finoguenov, A., Böhringer, H., & Zhang, Y.-Y., 2005, *A&A*, 442, 827
- Gastaldello, F., Buote, D. A., Humphrey, P. J., et. al. 2007, *ApJ*, submitted, astro-ph/0610134
- Halkola, A., Seitz, S., & Pannella, M. 2006, *MNRAS*, 372, 1425
- Henry, J. P. 2004, *ApJ*, 609, 603
- Hoekstra, H. 2003, *MNRAS*, 339, 1155
- Hoekstra, H. 2007, *MNRAS*, 379, 317
- Horner, H. 2001, Ph.D. Thesis, X-ray Scaling Laws for Galaxy Clusters and Groups
- Ikebe, Y., Reiprich, T. H., & Böhringer, H. 2002, *A&A*, 383, 773
- Jeltema, T. E., Canizares, C. R., Bautz, M. W., & Buote, D. A. 2005, *ApJ*, 624, 606
- Jones, C., & Forman, W. 1984, *ApJ*, 276, 38
- Kaiser, N., 2000, *ApJ*, 537, 555
- Kay, S. T. 2004, *MNRAS*, 347, L13
- King, L. J., Schneider, P., & Springel, V. 2001, *A&A*, 378, 748
- Kneib, J.-P., Hudelot, P., Ellis, R. S., et al. 2003, *ApJ*, 598, 804
- Kotov, O., & Vikhlinin, A. 2005, *ApJ*, 633, 781
- Kravtsov, A. V., Nagai, D., & Vikhlinin, A. 2005, *ApJ*, 625, 588
- Kravtsov, A. V., Vikhlinin, A., & Nagai, D. 2006, *ApJ*, 650, 128
- Limousin, M., Richard, J., Jullo, E., et al. 2007, *ApJ*, 668, 643
- Lloyd-Davies, E. J., Ponman, T. J., & Cannon, D. B. 2000, *MNRAS*, 315, 689
- Mahdavi, A., Hoekstra, H., Babul, A., & Henry, J. P. 2007, *MNRAS*, submitted, astro-ph/0710.4132
- Majerowicz, S., Neumann, D. M., & Reiprich, T. H. 2002, *A&A*, 394, 77
- Markevitch, M. 1998, *ApJ*, 504, 27
- Markevitch, M., Forman, W. R., Sarazin, C. L., & Vikhlinin, A. 1998, *ApJ*, 503, 77
- Massey, R., Rhodes, J., Ellis, R., et al. 2007, *Nature*, 445, 286
- Maughan, B. J., Jones, L. R., Ebeling, H., et al. 2003, *ApJ*, 587, 589
- Maughan, B. J. 2007, *ApJ*, in press, astro-ph/0703504
- Miralda-Escude, J. & Babul, A. 1995, *ApJ*, 449, 18
- Miyazaki, S., Hamana, T., Ellis, R. S., et al. 2007, *ApJ*, 669, 714
- Mohr, J. J., Mathiesen, B., & Evrard, A. E. 1999, *ApJ*, 517, 627
- Nagai, D., Vikhlinin, A. & Kravtsov, A. 2007a, *ApJ*, 655, 98
- Nagai, D., Kravtsov, A. & Vikhlinin, A. 2007b, *ApJ*, 688, 1
- Navarro, J. F., Frenk, C. S., & White, S. D. M. 1997, *ApJ*, 490, 493 (NFW)
- Navarro, J. F., Hayashi, E., Power, C., et al. 2004, *MNRAS*, 349, 1039
- Neumann, D., & Arnaud, M. 2001, *A&A*, 373, L33
- Pacaud F., Pierre, M., Adami, C., et al. 2007, *MNRAS*, in press, astro-ph/0709.1950
- Pearce, F. R., Thomas, P. A., Couchman, H. M. P., & Edge, A. C. 2000, *MNRAS*, 317, 1029
- Pedersen, K. & Dahle, H. 2007, *ApJ*, 667, 26
- Piffaretti, R., Jetzer, Ph., Kaastra, J. S., & Tamura, T. 2005, *A&A*, 433, 101

- Ponman, T. J., Cannon, D. B., & Navarro, J. F. 1999, *Natur*, 397, 135
- Ponman, T. J., Sanderson, A. J. R., & Finoguenov, A. 2003, *MNRAS*, 343, 331
- Poole, G. B., Fardal, M. A., Babul, A., & McCarthy, I. G. 2006, *MNRAS*, 373, 881
- Poole, G. B., Babul, A., McCarthy, I. G., & Fardal, M. A. 2007, *MNRAS*, submitted, astro-ph/0701586
- Popesso, P., Biviano, A., Böhringer, H., Romaniello, M., & Voges, W. 2005, *A&A*, 433, 431
- Pratt, G. W., Böhringer, H., & Finoguenov, A. 2005, *A&A*, 433, 777
- Pratt, G. W., Arnaud, M., & Pointecouteau, E. 2006, *A&A*, 446, 429
- Pratt, G. W., Böhringer, H., Croston, J. H., et al. 2007, *A&A*, 461, 71
- Rasia, E., Tormen, G., & Moscardini, L. 2004, *MNRAS*, 351, 237
- Rasia, E., Mazzotta, P., Borgani, S., et al. 2005, *ApJ*, 618, L1
- Rasia, E., Ettori, S., Moscardini, L., et al. 2006, *MNRAS*, 369, 2013
- Reiprich, T. H., & Böhringer, H. 2002, *ApJ*, 567, 716
- Rines, K., Diaferio, A., & Natarajan, P. 2007, *ApJ*, 657, 183
- Sanderson, A. J. R., Ponman, T. J., & O'Sullivan, E. 2006, *MNRAS*, 372, 1496
- Schuecker, P., Böhringer, H., Collins, C. A., & Guzzo, L. 2003, *A&A*, 398, 867
- Smith, G. P., Edge, A. C., Eke, V. R., et al. 2003, *ApJ*, 590, L79
- Smith, G. P., Kneib, J.-P., Smail, I., et al. 2005, *MNRAS*, 359, 417
- Spergel, D. N., Bean, R., Dore, O., et al. 2006, *ApJ*, in press, astro-ph/0603449
- Stanek, R., Evrard, A. E., Böhringer, H., Schuecker, P., & Nord, B. 2006, *ApJ*, 648, 956
- Sunyaev, R. A., & Zeldovich, Y. B. 1972, *Comm. on Ap. Sp. Phys.* 4, 173
- Swinbank, A. M., Bower, R. G., Smith, Graham P., et al. 2006, *MNRAS*, 368, 1631
- Tozzi, P., & Norman, C. 2001, *ApJ*, 546, 63
- Vikhlinin, A., Forman, W., & Jones, C. 1999, *ApJ*, 525, 47
- Vikhlinin, A., VanSpeybroeck, L., Markevitch, M., Forman, W., & Grego, L. 2002, *ApJ*, 578, L107
- Vikhlinin, A., Voevodkin, A., Mullis, C. R., et al. 2003, *ApJ*, 590, 15
- Vikhlinin, A., Markevitch, M., Murray, S. S., et al. 2005, *ApJ*, 628, 655
- Vikhlinin, A., Kravtsov, A., Forman, W., et al. 2006a, *ApJ*, 640, 691
- Vikhlinin, A., Burenin, R., Forman, W. R., et al. 2006b, *Proc. Heating vs. Cooling in Galaxies and Clusters of Galaxies*, eds. H. Böhringer, P. Schuecker, G. W. Pratt & A. Finoguenov, astro-ph/0611438
- Voit, G. M. 2005, *Rev. Mod. Phys.* 77, 207
- White, S. D. M., Navarro, J. F., Evrard, A. E., & Frenk, C. S. 1993, *Natur*, 366, 429
- Wittman, D., Dell'Antonio, I. P., Hughes, J. P., et al. 2006, *ApJ*, 643, 128
- Wu, X.-P. 2000, *MNRAS*, 316, 299
- Zhang, Y.-Y., Finoguenov, A., Böhringer, H., et al. 2004, *A&A*, 413, 49
- Zhang, Y.-Y., Böhringer, H., Mellier, Y., Soucail, G., & Forman, W. 2005a, *A&A*, 429, 85
- Zhang, Y.-Y., Böhringer, H., Finoguenov, A., et al. 2005b *Adv. Space Res.*, 36/4, 667
- Zhang, Y.-Y., Böhringer, H., Finoguenov, A., et al. 2006, *A&A*, 456, 55
- Zhang, Y.-Y., Finoguenov, A., Böhringer, H., et al. 2007, *A&A*, 467, 437

Table 1. Power law, $Y = Y_0 X^\gamma$, parameterized X-ray scaling relations. The mean of the scatter is determined by a Gaussian model fit to the histogram of the scatter.

X	Y	Y_0	γ	Scatter (dex)				Sample
				mean		average		
				X	Y	X	Y	
$\frac{Y_X}{M_\odot \text{ keV}} E(z)$	$\frac{M_{500}^X}{M_\odot} E(z)$	$10^{7.10 \pm 0.02} h_{70}^{-1}$	0.524 (fixed)	0.06	0.12	0.15	0.14	whole sample
		$10^{7.12 \pm 0.02} h_{70}^{-1}$	0.524 (fixed)	0.07	0.13	0.15	0.14	non-CCC subsample
		$10^{5.63 \pm 0.90} h_{70}^{-1}$	0.624 ± 0.061	0.08	0.13	0.13	0.13	whole sample
		$10^{5.03 \pm 1.07} h_{70}^{-1}$	0.666 ± 0.072	0.05	0.12	0.12	0.13	non-CCC subsample
$\frac{M_{\text{gas},500}}{M_\odot} E(z)$	$\frac{M_{500}^X}{M_\odot} E(z)$	$10^{3.62 \pm 0.02} h_{70}^{-1}$	0.806 (fixed)	0.03	0.13	0.10	0.14	whole sample
		$10^{3.65 \pm 0.02} h_{70}^{-1}$	0.806 (fixed)	0.03	0.13	0.10	0.14	non-CCC subsample
		$10^{2.23 \pm 1.08} h_{70}^{-1}$	0.906 ± 0.078	0.03	0.13	0.09	0.14	whole sample
		$10^{1.44 \pm 1.32} h_{70}^{-1}$	0.965 ± 0.095	0.03	0.13	0.08	0.13	non-CCC subsample
$\frac{T_{0.2-0.5r_{500}}}{\text{keV}} E(z)$	$\frac{M_{500}^X}{M_\odot} E(z)$	$10^{13.55 \pm 0.02} h_{70}^{-1}$	1.499 (fixed)	0.03	0.13	0.06	0.13	whole sample
		$10^{13.58 \pm 0.02} h_{70}^{-1}$	1.499 (fixed)	0.03	0.13	0.06	0.13	non-CCC subsample
		$10^{13.42 \pm 0.22} h_{70}^{-1}$	1.654 ± 0.256	0.03	0.13	0.06	0.14	whole sample
		$10^{13.40 \pm 0.25} h_{70}^{-1}$	1.718 ± 0.298	0.03	0.13	0.06	0.13	non-CCC subsample
$\frac{T_{0.2-0.5r_{500}}}{\text{keV}} E(z)$	$\frac{M_{\text{gas},500}}{M_\odot} E(z)$	$10^{12.33 \pm 0.01} h_{70}^{-1}$	1.859 (fixed)	0.03	0.03	0.04	0.08	whole sample
		$10^{12.33 \pm 0.02} h_{70}^{-1}$	1.859 (fixed)	0.03	0.03	0.04	0.08	non-CCC subsample
		$10^{12.33 \pm 0.16} h_{70}^{-1}$	1.859 ± 0.187	0.03	0.11	0.04	0.08	whole sample
		$10^{12.39 \pm 0.18} h_{70}^{-1}$	1.792 ± 0.215	0.07	0.13	0.04	0.08	non-CCC subsample
$\frac{T_{0.2-0.5r_{500}}}{\text{keV}} E(z)^{-1}$	$\frac{L_{0.1-2.4\text{keV}}^{\text{cor}}}{\text{erg s}^{-1}} E(z)^{-1}$	$10^{42.67 \pm 0.03} h_{70}^{-1}$	2.219 (fixed)	0.03	(0.03, 0.20)	0.06	0.13	whole sample
		$10^{42.65 \pm 0.04} h_{70}^{-1}$	2.219 (fixed)	0.04	0.18	0.06	0.13	non-CCC subsample
		$10^{42.75 \pm 0.28} h_{70}^{-1}$	2.127 ± 0.323	0.03	(0.03, 0.14)	0.06	0.13	whole sample
		$10^{42.84 \pm 0.31} h_{70}^{-1}$	1.994 ± 0.362	0.04	0.15	0.07	0.13	non-CCC subsample
$\frac{T_{0.2-0.5r_{500}}}{\text{keV}} E(z)^{-1}$	$\frac{L_{\text{bol}}^{\text{cor}}}{\text{erg s}^{-1}} E(z)^{-1}$	$10^{42.65 \pm 0.03} h_{70}^{-1}$	2.719 (fixed)	0.05	(0.03, 0.18)	0.05	0.13	whole sample
		$10^{42.62 \pm 0.03} h_{70}^{-1}$	2.719 (fixed)	0.03	0.16	0.05	0.13	non-CCC subsample
		$10^{42.74 \pm 0.27} h_{70}^{-1}$	2.614 ± 0.319	0.05	(0.03, 0.15)	0.05	0.13	whole sample
		$10^{42.85 \pm 0.31} h_{70}^{-1}$	2.457 ± 0.354	0.04	0.15	0.05	0.13	non-CCC subsample
$\frac{Y_X}{M_\odot \text{ keV}} E(z)$	$\frac{L_{\text{bol}}^{\text{cor}}}{\text{erg s}^{-1}} E(z)^{-1}$	$10^{30.92 \pm 0.02} h_{70}^{-1}$	0.951 (fixed)	0.07	0.03	0.09	0.09	whole sample
		$10^{30.89 \pm 0.02} h_{70}^{-1}$	0.951 (fixed)	0.05	0.03	0.09	0.09	non-CCC subsample
		$10^{30.92 \pm 1.19} h_{70}^{-1}$	0.951 ± 0.081	0.07	0.03	0.09	0.09	whole sample
		$10^{31.42 \pm 1.38} h_{70}^{-1}$	0.915 ± 0.093	0.06	0.03	0.10	0.09	non-CCC subsample
$\frac{M_{500}^X}{M_\odot} E(z)$	$\frac{L_{\text{bol}}^{\text{cor}}}{\text{erg s}^{-1}} E(z)^{-1}$	$10^{18.03 \pm 0.05} h_{70}^{-1}$	1.814 (fixed)	0.13	(0.06, 0.25)	0.15	0.21	whole sample
		$10^{17.96 \pm 0.06} h_{70}^{-1}$	1.814 (fixed)	0.13	(0.03, 0.18)	0.16	0.22	non-CCC subsample
		$10^{10.46 \pm 10.39} h_{70}^{-1}$	2.325 ± 0.701	0.13	0.09	0.15	0.26	whole sample
		$10^{15.12 \pm 10.91} h_{70}^{-1}$	2.005 ± 0.735	0.13	(0.03, 0.19)	0.16	0.24	non-CCC subsample

Here we provide the mean scatter derived by a Gaussian fit to the histogram, in which double values are from the histogram with a bi-modal Gaussian distribution. In Zhang et al. (2006, 2007), we only presented the average scatter due to the limited data points.

Table 2. Power law, $Y = Y_0 X^\gamma$, parameterized mass–observable scaling relations using weak lensing masses (M_{500}^{wl}) for the 19 LoCuSS clusters having weak lensing masses.

X	Y	Y_0	γ	Scatter (dex)				Sample
				mean		average		
				X	Y	X	Y	
$\frac{Y_X}{M_\odot \text{ keV}} E(z)$	$\frac{M_{500}^{\text{wl}}}{M_\odot} E(z)$	$10^{6.53 \pm 0.04} h_{70}^{-1}$	0.568 (fixed)	0.09	0.24	0.32	0.35	all
		$10^{6.54 \pm 0.06} h_{70}^{-1}$	0.568 (fixed)	0.25	0.23	0.37	0.32	non-CCC
		$10^{6.51 \pm 0.05} h_{70}^{-1}$	0.568 (fixed)	0.32	0.24	0.26	0.35	single
		$10^{6.58 \pm 0.08} h_{70}^{-1}$	0.568 (fixed)	0.30	0.24	0.40	0.38	merger
$\frac{M_{\text{gas},500}}{M_\odot} E(z)$	$\frac{M_{500}^{\text{wl}}}{M_\odot} E(z)$	$10^{2.48 \pm 0.04} h_{70}^{-1}$	0.894 (fixed)	0.11	0.24	0.20	0.35	all
		$10^{2.48 \pm 0.06} h_{70}^{-1}$	0.894 (fixed)	0.34	0.22	0.23	0.32	non-CCC
		$10^{2.46 \pm 0.05} h_{70}^{-1}$	0.894 (fixed)	0.08	0.23	0.16	0.34	single
		$10^{2.52 \pm 0.08} h_{70}^{-1}$	0.894 (fixed)	0.31	0.23	0.26	0.36	merger
$\frac{T_{0.2-0.5r_{500}}}{\text{keV}} E(z)$	$\frac{M_{500}^{\text{wl}}}{M_\odot} E(z)$	$10^{13.57 \pm 0.05} h_{70}^{-1}$	1.59 (fixed)	0.06	0.26	0.12	0.37	all
		$10^{13.57 \pm 0.06} h_{70}^{-1}$	1.59 (fixed)	0.09	0.23	0.14	0.33	non-CCC
		$10^{13.55 \pm 0.06} h_{70}^{-1}$	1.59 (fixed)	0.04	0.27	0.10	0.35	single
		$10^{13.62 \pm 0.09} h_{70}^{-1}$	1.59 (fixed)	0.10	0.33	0.14	0.39	merger
$\frac{M_{500}^{\text{wl}}}{M_\odot} E(z)$	$\frac{L_{\text{bol}}^{\text{corr}}}{\text{erg s}^{-1}} E(z)^{-1}$	$10^{21.51 \pm 0.07} h_{70}^{-1}$	1.572 (fixed)	0.24	0.26	0.35	0.29	all
		$10^{21.48 \pm 0.09} h_{70}^{-1}$	1.572 (fixed)	0.21	0.34	0.32	0.31	non-CCC
		$10^{21.58 \pm 0.09} h_{70}^{-1}$	1.572 (fixed)	0.22	0.19	0.33	0.24	single
		$10^{21.41 \pm 0.13} h_{70}^{-1}$	1.572 (fixed)	0.17	0.31	0.37	0.39	merger

In Col. Sample, “merger” (which denotes “primary with small secondary”, “elliptical”, “off-center” and “complex”) and “single” are classified as described in Jones & Forman (1992). Here we provide the mean scatter derived by a Gaussian fit to the histogram, in which double values are from the histogram with a bi-modal Gaussian distribution.

Table 3. See the caption in Table 2 except that the weak lensing masses, X-ray masses and Y_X parameters are determined within the radii ($r_{500}^{Y_X, X}$) determined by the method described in § 4.

X	Y	Y_0	γ	Scatter (dex)				Sample
				mean		average		
				X	Y	X	Y	
$\frac{Y_X(r_{500}^{Y_X, X})}{M_\odot \text{ keV}} E(z)$	$\frac{M^X(r_{500}^{Y_X, X})}{M_\odot} E(z)$	$10^{6.45 \pm 0.01} h_{70}^{-1}$	0.568 (fixed)	0.07	0.13	0.14	0.20	all
		$10^{6.47 \pm 0.01} h_{70}^{-1}$	0.568 (fixed)	0.07	0.13	0.14	0.20	non-CCC
$\frac{Y_X(r_{500}^{Y_X, X})}{M_\odot \text{ keV}} E(z)$	$\frac{M^{\text{wl}}(r_{500}^{Y_X, X})}{M_\odot} E(z)$	$10^{6.47 \pm 0.03} h_{70}^{-1}$	0.568 (fixed)	0.07	0.22	0.32	0.35	all
		$10^{6.47 \pm 0.04} h_{70}^{-1}$	0.568 (fixed)	0.09	0.20	0.32	0.31	non-CCC
$\frac{M_{\text{gas}}(r_{500}^{Y_X, X})}{M_\odot} E(z)$	$\frac{M^X(r_{500}^{Y_X, X})}{M_\odot} E(z)$	$10^{2.40 \pm 0.01} h_{70}^{-1}$	0.894 (fixed)	0.03	0.13	0.10	0.20	all
		$10^{2.42 \pm 0.02} h_{70}^{-1}$	0.894 (fixed)	0.03	0.13	0.09	0.20	non-CCC
$\frac{M_{\text{gas}}(r_{500}^{Y_X, X})}{M_\odot} E(z)$	$\frac{M^{\text{wl}}(r_{500}^{Y_X, X})}{M_\odot} E(z)$	$10^{2.40 \pm 0.03} h_{70}^{-1}$	0.894 (fixed)	0.03	0.18	0.20	0.35	all
		$10^{2.39 \pm 0.04} h_{70}^{-1}$	0.894 (fixed)	0.03	0.03	0.32	0.31	non-CCC
$\frac{T_{0.2-0.5r_{500}}}{\text{keV}} E(z)$	$\frac{M^X(r_{500}^{Y_X, X})}{M_\odot} E(z)$	$10^{13.48 \pm 0.02} h_{70}^{-1}$	1.59 (fixed)	0.03	0.13	0.05	0.20	all
		$10^{13.49 \pm 0.02} h_{70}^{-1}$	1.59 (fixed)	0.01	0.12	0.05	0.20	non-CCC
$\frac{T_{0.2-0.5r_{500}}}{\text{keV}} E(z)$	$\frac{M^{\text{wl}}(r_{500}^{Y_X, X})}{M_\odot} E(z)$	$10^{13.53 \pm 0.04} h_{70}^{-1}$	1.59 (fixed)	0.09	0.24	0.12	0.37	all
		$10^{13.53 \pm 0.04} h_{70}^{-1}$	1.59 (fixed)	0.10	0.22	0.32	0.31	non-CCC
$\frac{M^X(r_{500}^{Y_X, X})}{M_\odot} E(z)$	$\frac{L_{\text{bol}}^{\text{corr}}}{\text{erg s}^{-1}} E(z)^{-1}$	$10^{21.62 \pm 0.03} h_{70}^{-1}$	1.572 (fixed)	0.13	0.03	0.20	0.14	all
		$10^{21.58 \pm 0.03} h_{70}^{-1}$	1.572 (fixed)	0.13	0.03	0.20	0.15	non-CCC
$\frac{M^{\text{wl}}(r_{500}^{Y_X, X})}{M_\odot} E(z)$	$\frac{L_{\text{bol}}^{\text{corr}}}{\text{erg s}^{-1}} E(z)^{-1}$	$10^{21.59 \pm 0.05} h_{70}^{-1}$	1.572 (fixed)	0.13	0.03	0.35	0.29	all
		$10^{21.56 \pm 0.06} h_{70}^{-1}$	1.572 (fixed)	0.21	0.19	0.32	0.31	non-CCC

Table 4. See the caption in Table 2 except that the weak lensing masses, X-ray masses and Y_X parameters are determined within the radii ($r_{500}^{Y_X, \text{wl}}$) determined by the method described in § 6.2.3.

X	Y	Y_0	γ	Scatter (dex)				Sample
				mean		average		
				X	Y	X	Y	
$\frac{Y_X(r_{500}^{Y_X, \text{wl}})}{M_\odot \text{ keV}} E(z)$	$\frac{M^X(r_{500}^{Y_X, \text{wl}})}{M_\odot} E(z)$	$10^{6.44 \pm 0.01} h_{70}^{-1}$	0.568 (fixed)	0.08	0.13	0.13	0.20	all
		$10^{6.46 \pm 0.01} h_{70}^{-1}$	0.568 (fixed)	0.07	0.12	0.13	0.20	non-CCC
$\frac{Y_X(r_{500}^{Y_X, \text{wl}})}{M_\odot \text{ keV}} E(z)$	$\frac{M^{\text{wl}}(r_{500}^{Y_X, \text{wl}})}{M_\odot} E(z)$	$10^{6.46 \pm 0.03} h_{70}^{-1}$	0.568 (fixed)	0.05	0.19	0.22	0.38	all
		$10^{6.46 \pm 0.04} h_{70}^{-1}$	0.568 (fixed)	0.14	0.14	0.26	0.36	non-CCC
$\frac{M_{\text{gas}}(r_{500}^{Y_X, \text{wl}})}{M_\odot} E(z)$	$\frac{M^X(r_{500}^{Y_X, \text{wl}})}{M_\odot} E(z)$	$10^{2.39 \pm 0.01} h_{70}^{-1}$	0.894 (fixed)	0.03	0.12	0.09	0.20	all
		$10^{2.41 \pm 0.02} h_{70}^{-1}$	0.894 (fixed)	0.03	0.12	0.09	0.20	non-CCC
$\frac{M_{\text{gas}}(r_{500}^{Y_X, \text{wl}})}{M_\odot} E(z)$	$\frac{M^{\text{wl}}(r_{500}^{Y_X, \text{wl}})}{M_\odot} E(z)$	$10^{2.40 \pm 0.03} h_{70}^{-1}$	0.894 (fixed)	0.02	0.15	0.15	0.38	all
		$10^{2.40 \pm 0.04} h_{70}^{-1}$	0.894 (fixed)	0.12	0.06	0.17	0.36	non-CCC
$\frac{T_{0.2-0.5r_{500}}}{\text{keV}}$	$\frac{M^X(r_{500}^{Y_X, \text{wl}})}{M_\odot} E(z)$	$10^{13.47 \pm 0.02} h_{70}^{-1}$	1.59 (fixed)	0.03	0.13	0.05	0.20	all
		$10^{13.49 \pm 0.02} h_{70}^{-1}$	1.59 (fixed)	0.01	0.12	0.05	0.20	non-CCC
$\frac{T_{0.2-0.5r_{500}}}{\text{keV}}$	$\frac{M^{\text{wl}}(r_{500}^{Y_X, \text{wl}})}{M_\odot} E(z)$	$10^{13.49 \pm 0.04} h_{70}^{-1}$	1.59 (fixed)	0.08	0.24	0.09	0.39	all
		$10^{13.49 \pm 0.04} h_{70}^{-1}$	1.59 (fixed)	0.10	0.23	0.11	0.38	non-CCC
$\frac{M^X(r_{500}^{Y_X, \text{wl}})}{M_\odot} E(z)$	$\frac{L_{\text{bol}}^{\text{corr}}}{\text{erg s}^{-1}} E(z)^{-1}$	$10^{21.63 \pm 0.03} h_{70}^{-1}$	1.572 (fixed)	0.13	0.03	0.20	0.14	all
		$10^{21.59 \pm 0.03} h_{70}^{-1}$	1.572 (fixed)	0.13	0.07	0.20	0.15	non-CCC
$\frac{M^{\text{wl}}(r_{500}^{Y_X, \text{wl}})}{M_\odot} E(z)$	$\frac{L_{\text{bol}}^{\text{corr}}}{\text{erg s}^{-1}} E(z)^{-1}$	$10^{21.65 \pm 0.05} h_{70}^{-1}$	1.572 (fixed)	0.21	0.03	0.38	0.20	all
		$10^{21.61 \pm 0.06} h_{70}^{-1}$	1.572 (fixed)	0.19	0.14	0.37	0.24	non-CCC

Table 5. See the caption in Table 2 except that the weak lensing masses, X-ray masses and Y_X parameters are determined within the radii ($r_{500}^{Y_X, \text{sl}}$) determined by the method described in § 6.2.4.

X	Y	Y_0	γ	Scatter (dex)				Sample
				mean		average		
				X	Y	X	Y	
$\frac{Y_X(r_{500}^{Y_X, \text{sl}})}{M_\odot \text{ keV}} E(z)$	$\frac{M^X(r_{500}^{Y_X, \text{sl}})}{M_\odot} E(z)$	$10^{6.47 \pm 0.01} h_{70}^{-1}$	0.568 (fixed)	0.08	0.13	0.14	0.20	all
		$10^{6.49 \pm 0.02} h_{70}^{-1}$	0.568 (fixed)	0.08	0.13	0.13	0.20	non-CCC
$\frac{Y_X(r_{500}^{Y_X, \text{sl}})}{M_\odot \text{ keV}} E(z)$	$\frac{M^{\text{wl}}(r_{500}^{Y_X, \text{sl}})}{M_\odot} E(z)$	$10^{6.47 \pm 0.03} h_{70}^{-1}$	0.568 (fixed)	0.07	0.22	0.23	0.34	all
		$10^{6.47 \pm 0.04} h_{70}^{-1}$	0.568 (fixed)	0.09	0.20	0.27	0.32	non-CCC
$\frac{M_{\text{gas}}(r_{500}^{Y_X, \text{sl}})}{M_\odot} E(z)$	$\frac{M^X(r_{500}^{Y_X, \text{sl}})}{M_\odot} E(z)$	$10^{2.40 \pm 0.02} h_{70}^{-1}$	0.894 (fixed)	0.03	0.13	0.09	0.20	all
		$10^{2.43 \pm 0.02} h_{70}^{-1}$	0.894 (fixed)	0.03	0.13	0.10	0.20	non-CCC
$\frac{M_{\text{gas}}(r_{500}^{Y_X, \text{sl}})}{M_\odot} E(z)$	$\frac{M^{\text{wl}}(r_{500}^{Y_X, \text{sl}})}{M_\odot} E(z)$	$10^{2.40 \pm 0.03} h_{70}^{-1}$	0.894 (fixed)	0.03	0.18	0.15	0.34	all
		$10^{2.40 \pm 0.04} h_{70}^{-1}$	0.894 (fixed)	0.15	0.09	0.17	0.32	non-CCC
$\frac{T_{0.2-0.5r_{500}}}{\text{keV}}$	$\frac{M^X(r_{500}^{Y_X, \text{sl}})}{M_\odot} E(z)$	$10^{13.52 \pm 0.02} h_{70}^{-1}$	1.59 (fixed)	0.05	0.12	0.05	0.19	all
		$10^{13.53 \pm 0.02} h_{70}^{-1}$	1.59 (fixed)	0.02	0.13	0.06	0.20	non-CCC
$\frac{T_{0.2-0.5r_{500}}}{\text{keV}}$	$\frac{M^{\text{wl}}(r_{500}^{Y_X, \text{sl}})}{M_\odot} E(z)$	$10^{13.53 \pm 0.04} h_{70}^{-1}$	1.59 (fixed)	0.09	0.24	0.09	0.35	all
		$10^{13.53 \pm 0.04} h_{70}^{-1}$	1.59 (fixed)	0.10	0.22	0.11	0.33	non-CCC
$\frac{M^X(r_{500}^{Y_X, \text{sl}})}{M_\odot} E(z)$	$\frac{L_{\text{bol}}^{\text{corr}}}{\text{erg s}^{-1}} E(z)^{-1}$	$10^{21.56 \pm 0.03} h_{70}^{-1}$	1.572 (fixed)	0.13	0.14	0.20	0.15	all
		$10^{21.51 \pm 0.03} h_{70}^{-1}$	1.572 (fixed)	0.13	0.14	0.20	0.18	non-CCC
$\frac{M^{\text{wl}}(r_{500}^{Y_X, \text{sl}})}{M_\odot} E(z)$	$\frac{L_{\text{bol}}^{\text{corr}}}{\text{erg s}^{-1}} E(z)^{-1}$	$10^{21.59 \pm 0.05} h_{70}^{-1}$	1.572 (fixed)	0.18	0.03	0.34	0.21	all
		$10^{21.56 \pm 0.06} h_{70}^{-1}$	1.572 (fixed)	0.21	0.17	0.33	0.24	non-CCC

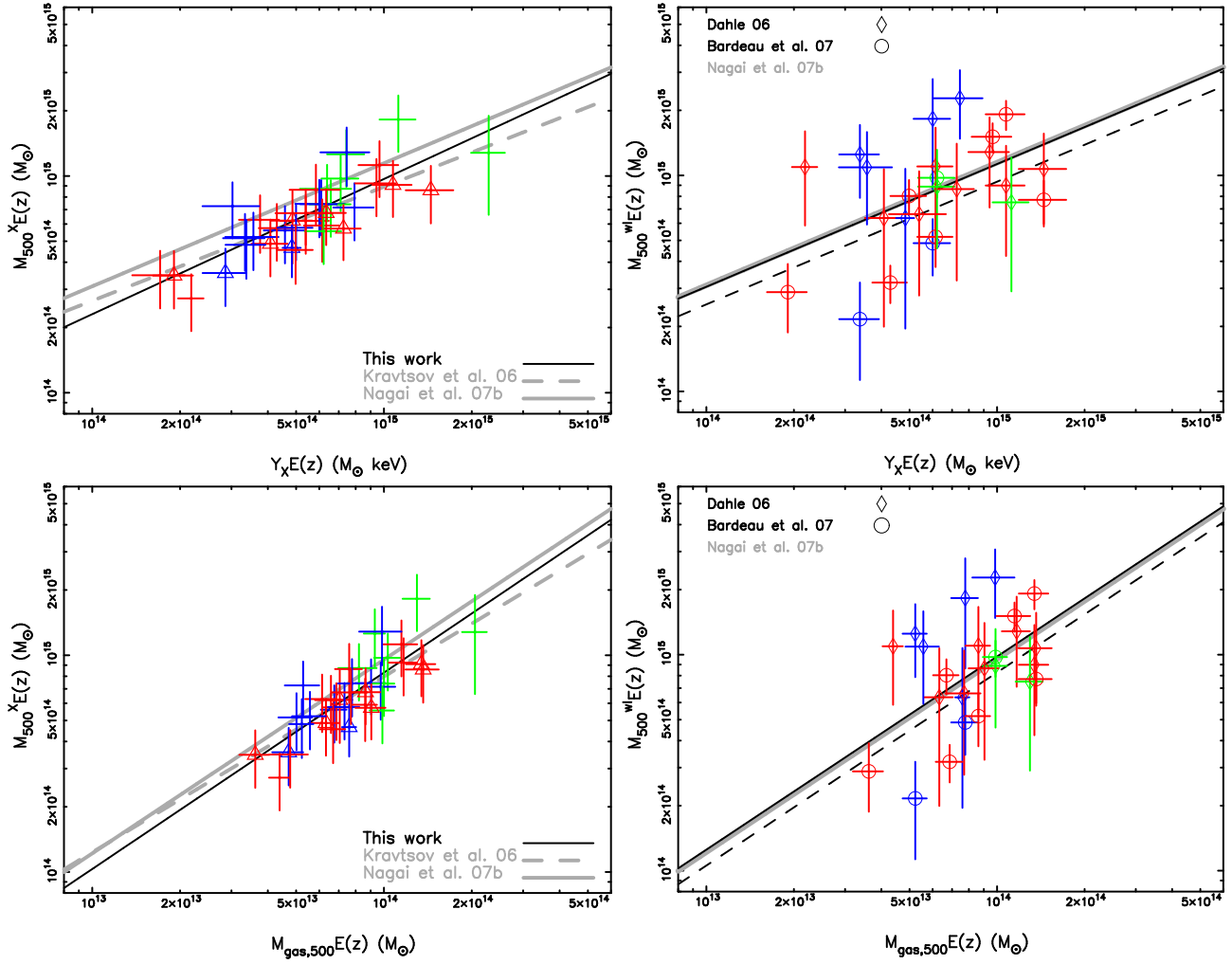


Fig. 1. Mass– Y_X (upper panels) and mass–gas mass (lower panels) relations using X-ray masses (left panels) and weak lensing masses (right panels). The CCCs are marked by triangles in the left panels. The best-fit power law in the right panels (solid, using weak lensing masses; dashed, using X-ray masses) with their slopes fixed to the values as found in simulations in order to compare the normalization (Table 2). The clusters appearing “primary with small secondary” or “off-center” morphology are in green, appearing “elliptical” or “complex” morphology are in blue, and appearing “single” morphology are in red using the classification in Jones & Forman (1992).

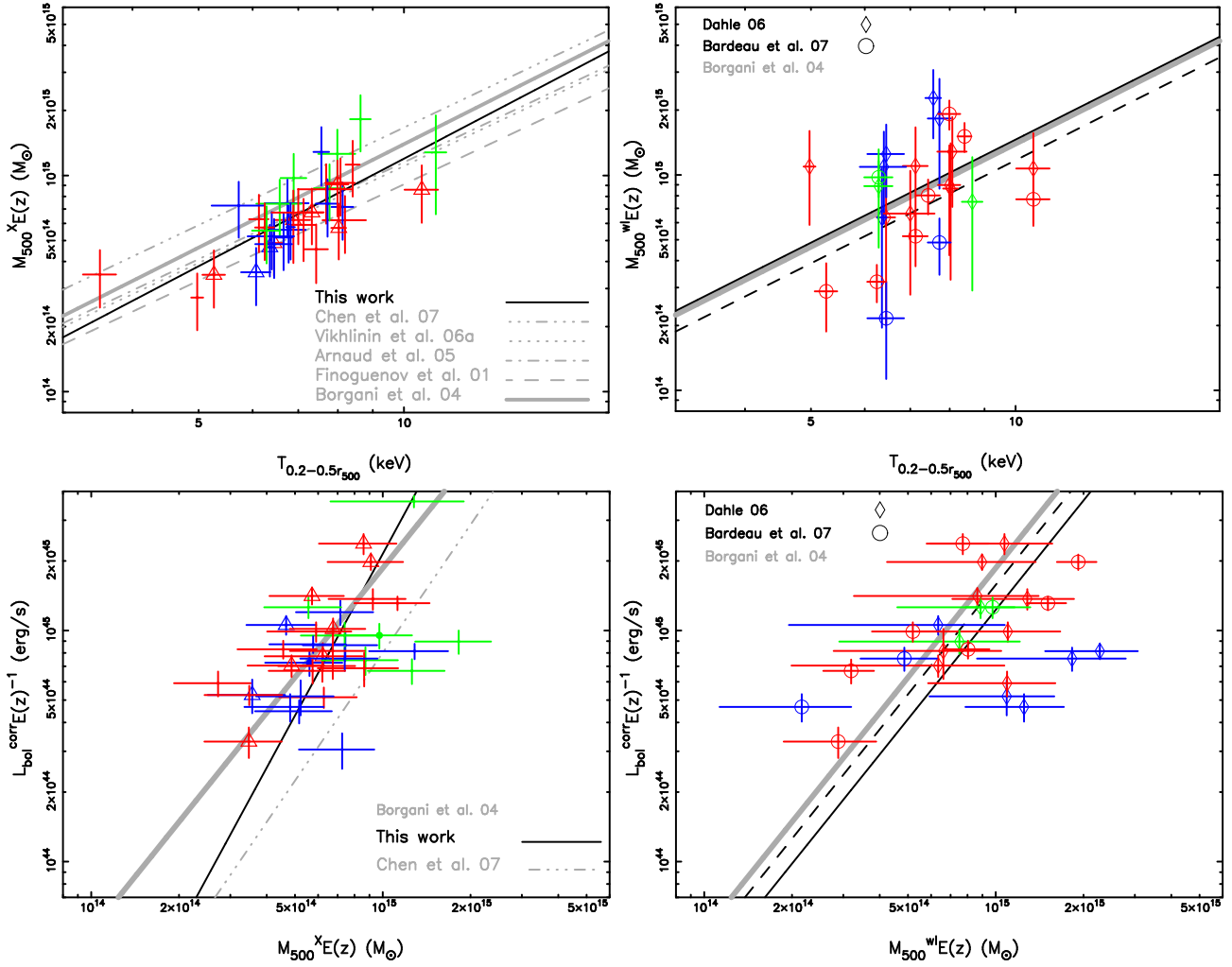


Fig. 2. Mass–temperature (upper panels) and luminosity–mass (lower panels) relations using X-ray masses (left panels) and weak lensing masses (right panels). The CCCs are marked by triangles in the left panels. The best-fit power law in the right panels (solid, using weak lensing masses; dashed, using X-ray masses) with their slopes fixed to the values as found in simulations in order to compare the normalization (Table 2). The colors have the same meaning as those in Fig. 1.

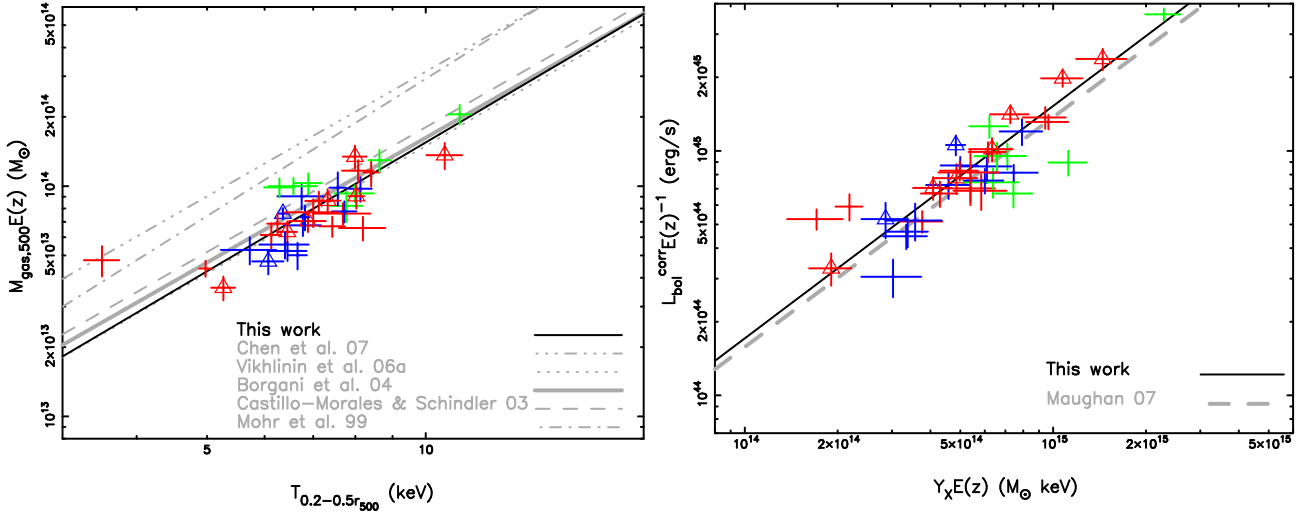


Fig. 3. *Left:* Gas mass–temperature relation. *Right:* Luminosity– Y_X relation. The CCCs are marked by triangles.

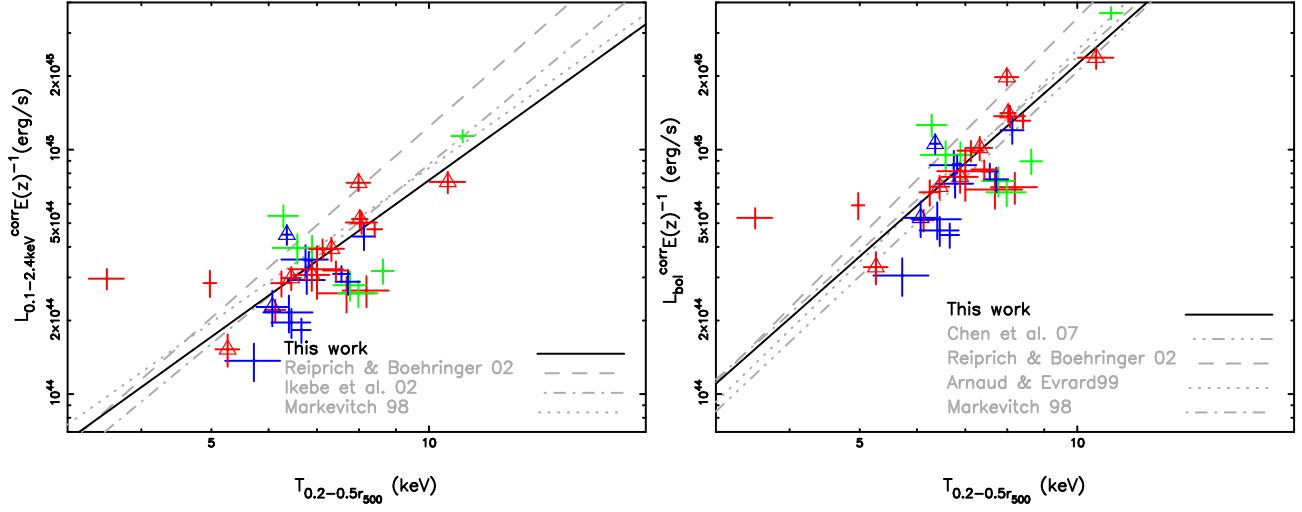


Fig. 4. X-ray luminosity in the 0.1–2.4 keV band versus temperature (left) and bolometric X-ray luminosity versus temperature (right). The CCCs are marked by triangles. The colors have the same meaning as those in Fig. 1.

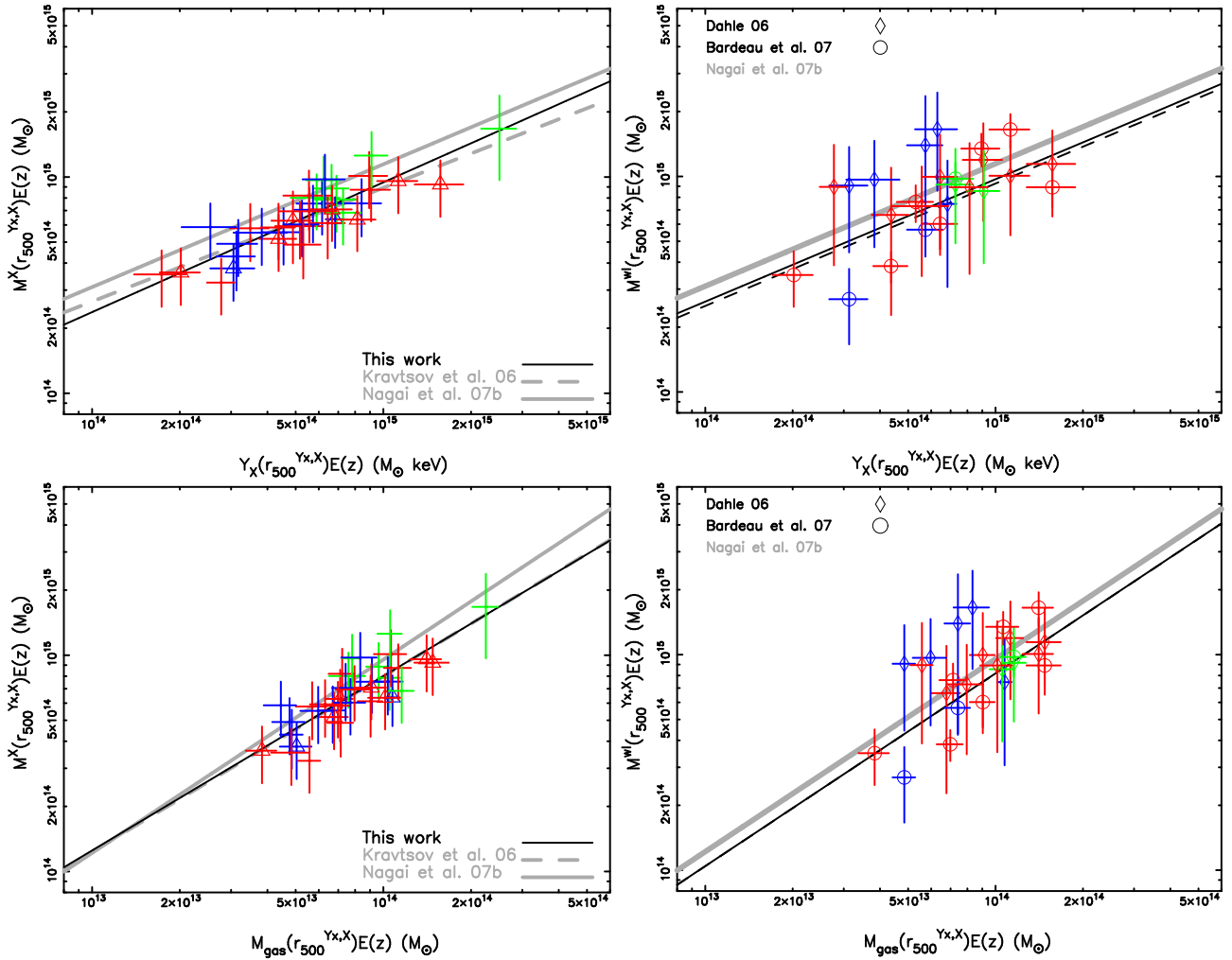


Fig. 5. See caption in Fig. 1 except that the weak lensing masses, X-ray masses and Y_X parameters are determined within the radii ($r_{500}^{Y_X,X}$) determined by the method described in § 4 (also see Table 3).

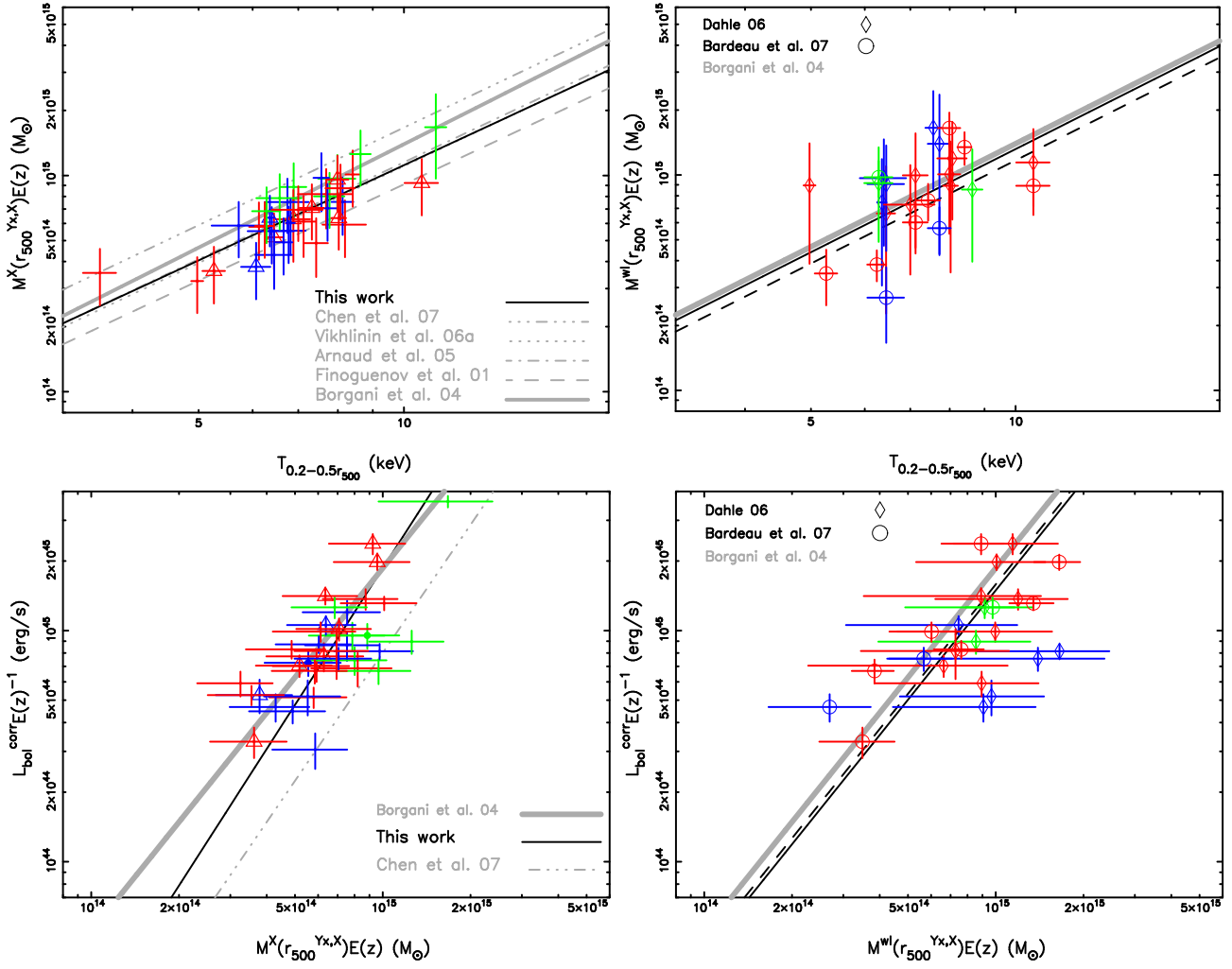


Fig. 6. See caption in Fig. 2 except that the weak lensing masses, X-ray masses and Y_X parameters are determined within the radii ($r_{500}^{Y_X, X}$) determined by the method described in § 4 (also see Table 3).

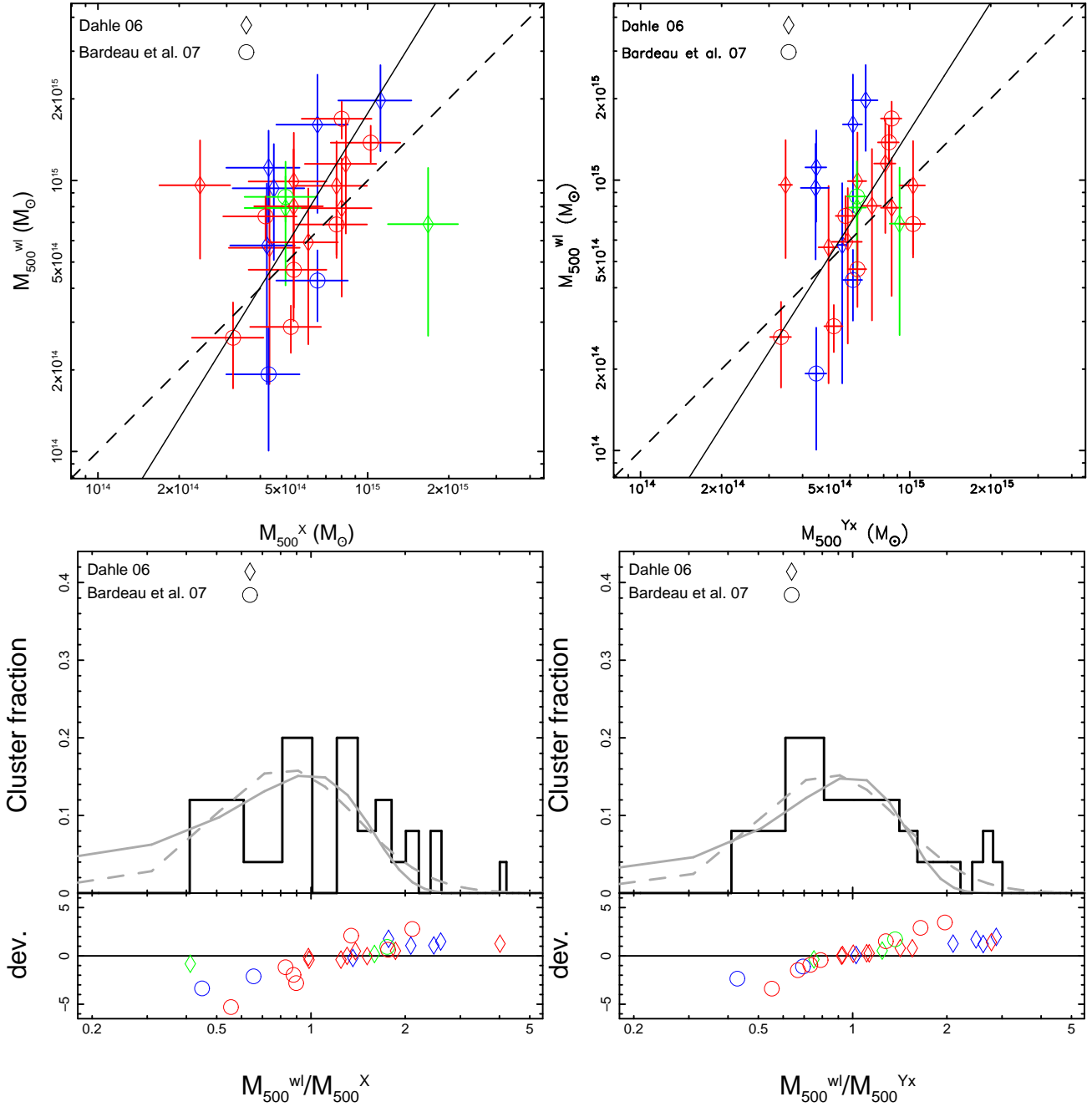


Fig. 7. *Upper left:* M_{500}^{wl} versus M_{500}^X (a best-fit slope of 1.61 ± 0.39). *Upper right:* M_{500}^{wl} versus M_{500}^{Yx} (a best-fit slope of 1.57 ± 0.38). M_{500}^{Yx} is derived from Y_X with the slope fixed to 0.568 (the prediction from simulations in Nagai et al. 2007b) fitting M - Y_X relation for our sample. *Lower panels:* Normalized differential cluster number count as a function of the M_{500}^{wl} to M_{500}^X ratio and M_{500}^{wl} to M_{500}^{Yx} ratio, respectively, with their Gaussian fits (gray, solid curves denote the fits with x-axis in linear space, and dashed curves in logarithmic space). The lower parts of the lower panels show the M_{500}^{wl} versus M_{500}^X discrepancy and M_{500}^{wl} versus M_{500}^{Yx} discrepancy, respectively, normalized to the error bar of M_{500}^{wl} . The colors have the same meaning as those in Fig. 1.

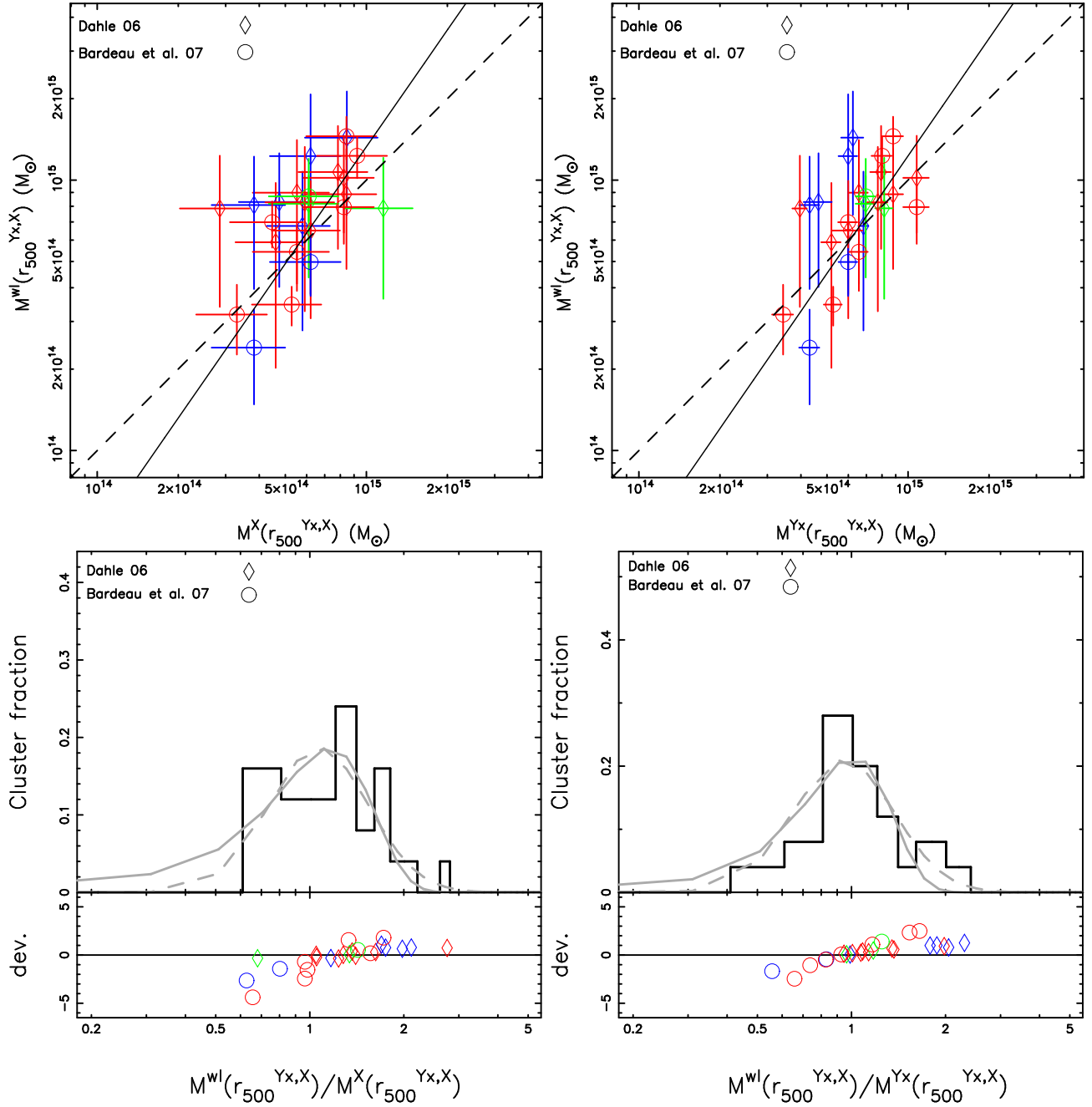


Fig. 8. See caption in Fig. 7 except that the weak lensing masses and X-ray masses are determined within the radii ($r_{500}^{Yx,X}$) determined by the method described in § 4.

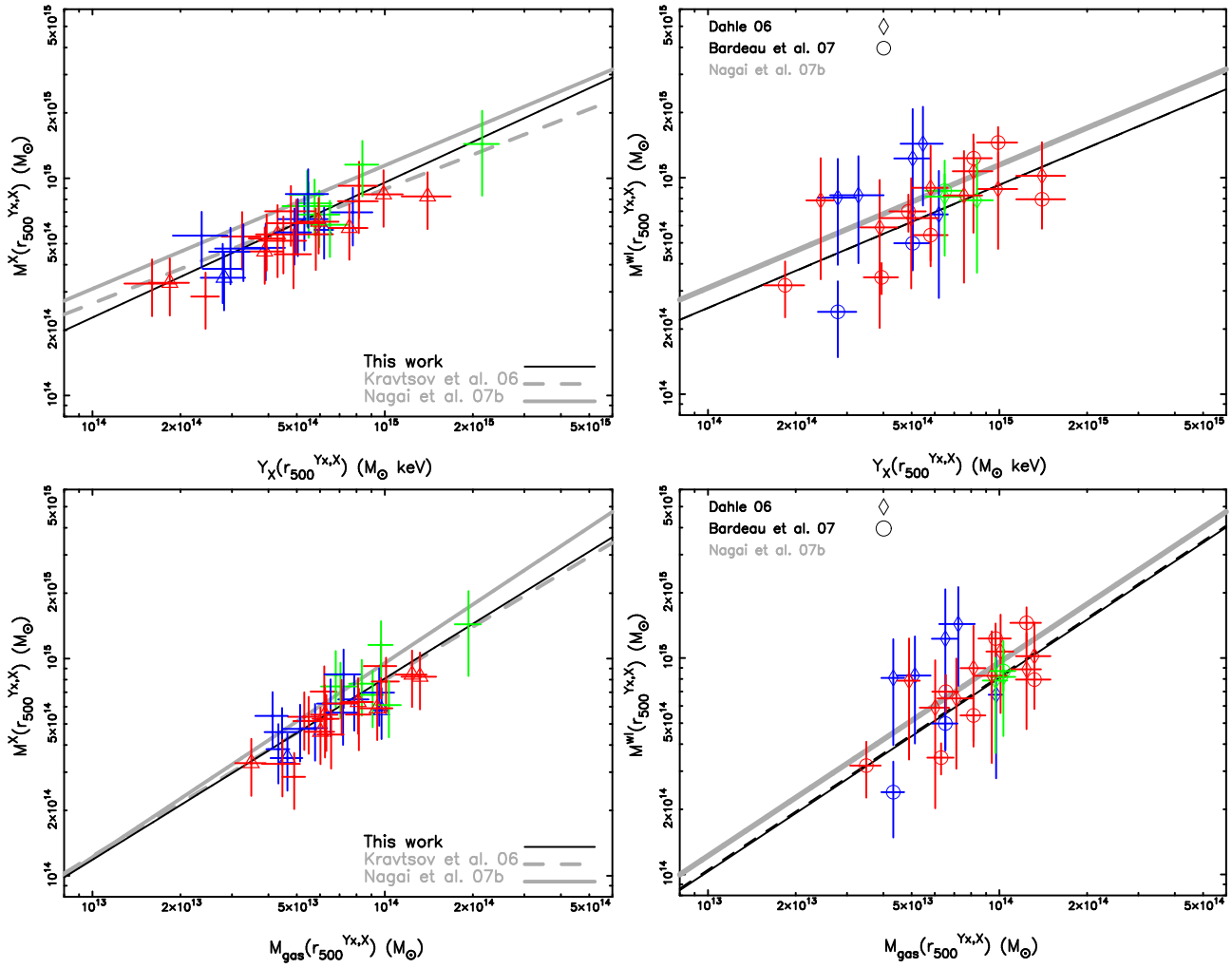


Fig. 9. See caption in Fig. 5 except that no LSS evolution correction is applied in the mass–observable relations.

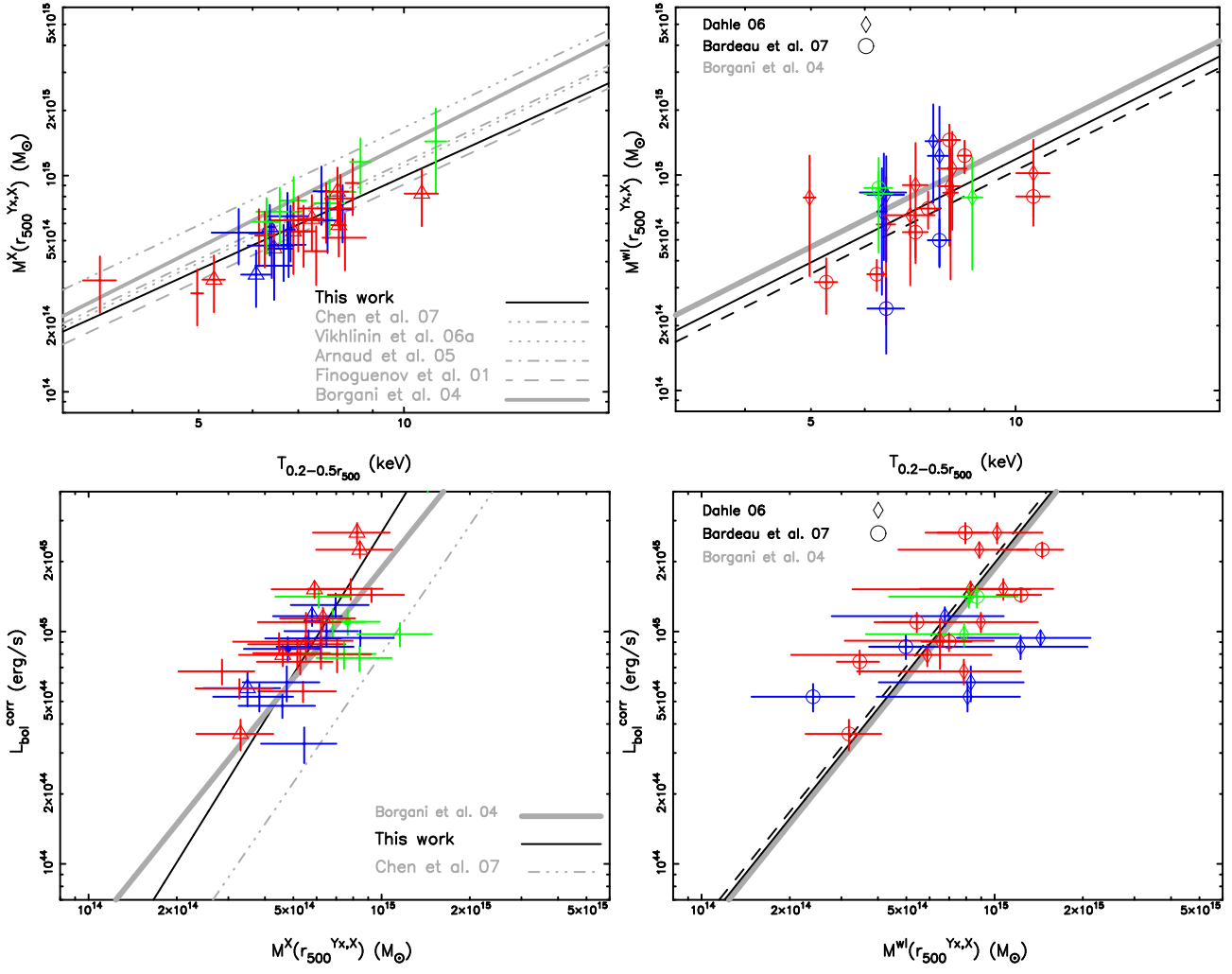


Fig. 10. See caption in Fig. 6 except that no LSS evolution correction is applied in the mass–observable relations.

Appendix A: X-ray mass modeling

The X-ray mass modeling described here helps to understand the measurement uncertainties of the X-ray quantities used for studies of the scaling relations.

We show the ROSAT luminosity versus redshift distribution for the LoCuSS sample in Fig. A.1 and the observational information of the *XMM-Newton* data for the 37 LoCuSS clusters in Table A.1. The primary parameters of all 37 LoCuSS galaxy clusters are given in Table A.2.

A.1. Density contrast

To determine the global cluster parameters, one needs a fiducial outer radius that was defined as follows. The mean cluster density contrast is the average density with respect to the critical density,

$$\Delta(< r) = \frac{3M(< r)}{4\pi r^3 \rho_c(z)}. \quad (\text{A.1})$$

The critical density at redshift z is $\rho_c(z) = \rho_{c0} E^2(z)$, where $E^2(z) = \Omega_m(1+z)^3 + \Omega_\Lambda + (1 - \Omega_m - \Omega_\Lambda)(1+z)^2$. r_Δ is the radius within which the density contrast is Δ . M_Δ is the total mass within r_Δ . For $\Delta = 500$, r_{500} is the radius within which the density contrast is 500 and M_{500} is the total mass within r_{500} .

A.2. Temperature profiles

XMM-Newton (as well as *Chandra*), in contrast to earlier telescopes, has a less energy-dependent, smaller PSF, more reliable to study cluster temperature profiles. We de-projected the spectra (see the method in Zhang et al. 2007) and performed the spectral fitting in XSPEC to obtain the radial profiles of the temperature and metallicity. In Figs. A.2–A.4 in the electronic edition of the Journal (together with Fig. 2 in Zhang et al. 2006, and Fig. 1 and Figs. B.1–B.5 in Zhang et al. 2007 for the whole sample) we show the radial temperature profiles. The temperature profiles are approximated by

$$T(r) = P_3 \exp[-(r - P_1)^2/P_2] + P_6(1 + r^2/P_4^2)^{-P_5} + P_7, \quad (\text{A.2})$$

motivated by the qualitative appearance of the observed temperature distributions of clusters of galaxies. P_i , $i = 1, \dots, 7$, are used for parameterization.

A CCC often shows both a peaked surface brightness profile and a steep temperature drop towards the cluster center. Our sample does not show pronounced CCC and non-CCC bimodal distribution. For studies of the segregation of the X-ray scaling relations we empirically define the CCC as the cluster whose temperature drop is greater than 30 per cent of the peak temperature towards the cluster center. Nine clusters are therefore CCCs in this sample. There might be more CCCs in the sample if the sample would be constructed using the higher resolution temperature measurements.

The X-ray surface brightness isophotes are also sensitive to cluster populations. We therefore also used the classification of the cluster morphologies in Jones & Forman (1992) and divided the sample to 5 types (Table B.1): “single”, “primary

with a small secondary”, “elliptical”, “off-center” and “complex” based on the smoothness of its X-ray surface brightness isophotes in the 0.7–2 keV band. Therefore “single” approximately denotes relaxed clusters, “primary with a small secondary”, “off-center”, “elliptical” and “complex” denote merging clusters.

About 80 per cent CCCs are relaxed clusters (“single” defined in § 6 using surface brightness isophotes). As we show later, these 9 CCCs often show shorter central cooling time, larger cooling radii (scaled to r_{500}) and lower central entropies compared to the non-CCCs in the sample (Table B.1).

A.3. Surface brightness profiles

A β model (e.g. Cavaliere & Fusco-Femiano 1976; Jones & Forman 1984) is often used to describe electron density profiles in clusters. To obtain an acceptable fit for all clusters in the sample, we adopt a double- β model of the electron number density profile, $n_e(r) = n_{e01}(1 + r^2/r_{c1}^2)^{-3\beta/2} + n_{e02}(1 + r^2/r_{c2}^2)^{-3\beta/2}$, where $n_{e0} = n_{e01} + n_{e02}$ is the central electron number density (see Table B.1), β the slope parameter, and r_{c1} and r_{c2} the core radii of the inner and outer components, respectively. The β value is derived by fitting the outer component, and it is used for the inner component since the inner component is insensitive to the slope. The soft band (e.g. 0.5–2 keV for 9 REFLEX-DXL clusters and 0.7–2 keV for the remaining 28 clusters) X-ray surface brightness profile model $S(R)$, in which R is the projected radius, is linked to the radial profile of the ICM electron number density $n_e(r)$ and emissivity function as an integral performed along the line-of-sight for galaxy clusters. For massive clusters (i.e. $T > 3.5$ keV) the cooling function can be treated as a temperature independent quantity in the soft band, and the surface brightness profile is thus described as follows,

$$S_X(R) \propto \int_R^\infty n_p n_e dl. \quad (\text{A.3})$$

For the whole sample, the best-fit “mekal” model of the spectra limited to $0.2r_{500} < R < 0.5r_{500}$ is used to convert the surface brightness profile to derive the density distribution. We fitted the observed surface brightness profile by this integral convolved with the *XMM-Newton* PSF matrices (Figs. A.5–A.7 in the electronic edition of the Journal, Fig. 3 in Zhang et al. 2006, and Fig. 1 and Figs. B.1–B.5 in Zhang et al. 2007 for the whole sample) and obtained the parameters of the double- β model of the electron density profile. The fit was performed within the truncation radius (r_t , see Table A.2) corresponding to a S/N of 3 of the observational surface brightness profile. The truncation radii r_t are often larger than r_{500} . The cluster cores, referring to the core of the inner component of the double- β model, span a broad range up to $0.2 r_{500}$.

A.4. Mass distribution

The ICM can be used to trace the cluster potential. We assume that, (1) the ICM is in hydrostatic equilibrium within the gravitational potential dominated by DM, (2) the DM distribution is spherically symmetric, and (3) the kinematic term is approximated to zero in hydrostatic equilibrium. The cluster mass is

then calculated from the X-ray measured ICM density and temperature distributions by,

$$\frac{1}{\mu m_p n_e(r)} \frac{d[n_e(r)T(r)]}{dr} = -\frac{GM(< r)}{r^2}, \quad (\text{A.4})$$

where $\mu = 0.62$ is the mean molecular weight per hydrogen atom. The Boltzmann constant is included in T as the temperature is in units of keV. Following the method in Zhang et al. (2007), we use a set of input parameters of the approximation functions, in which β , n_{e0i} , r_{ci} ($i = 1, 2$) represent the electron number density profile $n_e(r)$ and P_i ($i = 1, \dots, 7$) represent the temperature profile $T(r)$, respectively, to compute the mean cluster mass. The mass uncertainties are propagated using the uncertainties of the electron number density and temperature measurements by Monte Carlo simulations as follows (see also Zhang et al. 2007). For each cluster, we simulated the electron density and temperature profiles of a sample of 100 clusters using observed electron density and temperature profiles and their errors. The mass profiles and other properties of the 100 simulated clusters were calculated to derive the errors.

The derived mass profile was used to calculate the density contrast profile to derive M_{500} and r_{500} (see Table B.1). In Figs. A.8–A.10 in the electronic edition of the Journal (together with Fig. 5 in Zhang et al. 2006, and Fig. 1 and Figs. B.1–B.5 in Zhang et al. 2007 for the whole sample), we present the observed mass profiles.

A.5. Gas mass fraction distribution

The gas mass fraction is an important parameter for cluster physics, e.g. heating and cooling processes, and cosmological applications using galaxy clusters (e.g. Vikhlinin et al. 2002; Allen et al. 2004). The gas mass fraction distribution is defined as $f_{\text{gas}}(< r) = M_{\text{gas}}(< r)/M(< r)$. The gas mass, total mass and gas mass fraction at r_{500} are given in Table B.1. We obtain an average gas mass fraction of 0.121 ± 0.004 at r_{500} for the sample.

As observed, the gas mass fraction at r_{500} is generally lower than the universal baryon fraction, $f_b = \Omega_b/\Omega_m = 0.176 \pm 0.019$, based on the WMAP three year results in Spergel et al. (2006). This is because the baryons in galaxy clusters reside mostly in hot gas together with a small fraction of stars as implied in observations (0.003–0.022 in groups, Gastaldello et al. 2007) and simulations (15 per cent of f_{gas} , e.g. Kravtsov et al. 2005). In principle, Ω_m can be determined from the baryon fraction, $f_b = f_{\text{gas}} + f_{\text{gal}}$, in which a contribution from stars in galaxies is given by $f_{\text{gal}} = 0.02 \pm 0.01 h_{50}^{-1}$ (White et al. 1993). The average gas mass fraction at r_{500} for the sample supports a low matter density Universe as also shown in e.g. Allen et al. (2002), Ettori et al. (2003) and Vikhlinin et al. (2003).

Table A.1.

Name	X-ray centroid						Id	Date	Filter		Frame		Net exposure (ks)		
	R.A.			dec.					MOS	pn	pn	MOS1	MOS2	pn	
RXCJ0043.4-2037	00	43	24.5	-20	43	31.2	0042340201	2002-01-04	Thin	Thin	EFF	11.4	11.4	7.1	
RXCJ0232.2-4420	02	32	18.8	-44	32	51.9	0042340301	2002-07-11	Thin	Thin	EFF	12.7	12.1	8.7	
RXCJ0307.0-2840	03	07	02.2	-28	07	55.2	0042340501	2001-02-16	Thin	Thin	EFF	12.4	12.7	9.3	
RXCJ0516.7-5430	05	16	35.2	-54	16	36.8	0205330301	2004-01-13	Thin	Thin	FF	10.6	11.1	8.9	
RXCJ0528.9-3927	05	28	52.5	-39	28	16.7	0042340801	2001-09-15	Thin	Thin	EFF	7.2	6.9	3.7	
RXCJ0532.9-3701	05	32	55.9	-37	32	34.5	0042341801	2002-10-07	Thin	Thin	EFF	10.5	11.3	7.3	
RXCJ0547.6-3152	05	47	38.3	-31	47	28.8	0201900901	2004-03-07	Thin	Thin	EFF	21.8	22.1	17.6	
RXCJ0645.4-5413	06	45	30.0	-54	45	42.1	0201901201	2004-05-07	Thin	Thin	EFF	11.6	12.2	9.6	
RXCJ0658.5-5556	06	58	30.2	-55	58	33.7	0112980201	2000-10-21	Thin	Thin	EFF	25.7	23.7	21.1	
RXCJ0945.4-0839	09	45	25.1	-08	45	11.7	0017540101	2001-12-02	Medium	Medium	FF	7.1	6.4	4.4	
RXCJ0958.3-1103	09	58	21.9	-11	58	48.2	0201903501	2004-06-17	Thin	Thin	EFF	7.9	7.9	5.3	
RXCJ2129.6+0005	21	29	39.8	+00	29	18.5	0093030201	2002-10-29	Medium	Medium	EFF	38.4	39.4	25.6	
RXCJ2218.6-3853	22	18	39.9	-38	18	43.6	0201903001	2004-10-24	Thin	Thin	EFF	20.4	20.3	12.0	
RXCJ2234.5-3744	22	34	27.1	-37	34	07.5	0018741701	2001-05-03	Thin	Thin	FF	6.7	6.6	4.2	
RXCJ2308.3-0211	23	08	22.3	-02	08	32.1	0205330501	2004-06-05	Thin	Thin	FF	9.6	10.0	7.8	
RXCJ2337.6+0016	23	37	37.8	+00	37	15.5	0042341301	2001-12-06	Thin	Thin	EFF	12.4	12.0	8.3	
Abell68	00	37	06.2	+09	37	28.7	0084230201	2001-12-14	Medium	Medium	EFF	24.9	23.8	18.2	
Abell115	00	55	50.1	+26	55	35.7	0203220101	2004-07-16	Medium	Medium	EFF	36.0	36.8	29.5	
Abell209	01	31	52.6	-13	31	35.5	0084230301	2001-01-15	Medium	Medium	EFF	17.3	16.1	12.8	
Abell267	01	52	42.0	+01	52	41.2	0084230401	2002-01-02	Medium	Medium	EFF	17.2	17.1	12.4	
Abell383	02	48	03.3	-03	48	43.6	0084230501	2002-08-17	Medium	Medium	EFF	28.1	28.0	21.5	
Abell773	09	17	52.9	+51	17	19.4	0084230601	2001-04-26	Medium	Medium	EFF	13.0	14.7	15.9	
Abell781	09	20	24.8	+30	20	05.7	0150620201	2003-04-22	Medium	Medium	FF	14.0	14.1	11.6	
Abell901	09	55	57.7	-09	55	06.3	0148170101	2003-05-06	Thin	Thin	FF	19.4	18.6	53.2	
Abell963	10	17	03.2	+39	17	56.5	0084230701	2001-11-02	Medium	Medium	EFF	23.8	24.7	17.9	
Abell1413	11	55	18.3	+23	55	12.7	0112230501	2000-12-06	Thin	Thin	FF	23.6	24.4	18.8	
Abell1689	13	11	29.3	-01	11	26.7	0093030101	2001-12-24	Thin	Thin	EFF	36.8	37.0	32.6	
Abell1758	13	32	44.6	+50	32	46.5	0142860201	2002-11-12	Medium	Medium	FF	38.1	40.1	19.4	
Abell1763	13	35	18.1	+41	35	03.9	0084230901	2002-12-13	Medium	Medium	EFF	12.3	12.0	9.3	
Abell1835	14	01	01.9	+02	01	35.5	0098010101	2000-06-28	Thin	Thin	FF	25.3	25.3	24.7	
Abell1914	14	26	00.8	+37	26	38.8	0112230201	2002-12-18	Thin	Medium	EFF	20.5	21.2	14.5	
Abell2204	16	32	47.1	+05	32	32.3	0112230301	2001-09-12	Medium	Medium	FF	17.5	18.5	14.3	
Abell2218	16	35	53.8	+66	35	32.4	0112980101	2002-09-28	Thin	Thin	EFF	16.7	16.9	13.8	
Abell2261	17	22	26.0	+32	22	47.4	0093031001	2003-08-29	Thin	Thin	EFF	2.7	2.9	0.9	
Abell2390	21	53	37.1	+17	53	46.4	0111270101	2001-06-19	Thin	Thin	FF	10.3	10.0	8.8	
Abell2667	23	51	39.2	-26	51	03.5	0148990101	2003-06-21	Medium	Medium	FF	22.2	22.9	14.1	
Z7160	14	57	15.2	+22	57	31.2	0108670201	2002-08-03	Medium	Medium	FF	31.2	31.6	26.3	

The cluster center is in sky coordinates in epoch J2000. The MOS data are in EE mode except that the MOS1 data of Abell1835 are in window mode, which cannot be used for this work.

Table A.2. Primary parameters. Column (1): cluster name; Col. (2): optical redshift (e.g. Böhringer et al. 2004; Smith et al. 2005; Bardeau et al. 2007); Col. (3): hydrogen column density (Dickey & Lockman 1990); Col. (4): truncation radius corresponding to a S/N of 3 of the observational surface brightness profile; Col. (5): volume averaged radial temperature profile of $0.2-0.5r_{500}$; Cols. (6–7): Spectroscopic temperature and metallicity in the annulus of $0.2-0.5r_{500}$. Cols. (8–10): bolometric luminosity including the $< 0.2r_{500}$ region, excluding the $< 0.2r_{500}$ region, and corrected for the $< 0.2r_{500}$ region, respectively.

Name	z_{opt}	N_{H} 10^{22} cm^{-2}	r_{t} /'	$T_{0.2-0.5r_{500}}$ keV	$T_{0.2-0.5r_{500}}^{\text{spec}}$ keV	$Z_{0.2-0.5r_{500}}^{\text{spec}}$ Z_{\odot}	$L_{\text{bol}}^{\text{incc}}$ 10^{45} erg/s	$L_{\text{bol}}^{\text{excc}}$ 10^{45} erg/s	$L_{\text{bol}}^{\text{corr}}$ 10^{45} erg/s
RXCJ0043.4-2037	0.292	0.0154	7.0	6.8 ± 0.4	7.0 ± 0.4	0.17 ± 0.06	1.05 ± 0.10	0.59 ± 0.07	0.84 ± 0.10
RXCJ0232.2-4420	0.284	0.0250	6.8	6.9 ± 0.3	6.6 ± 0.3	0.23 ± 0.07	1.85 ± 0.14	0.75 ± 0.08	1.10 ± 0.14
RXCJ0307.0-2840	0.258	0.0136	4.7	6.9 ± 0.4	7.1 ± 0.4	0.26 ± 0.08	1.31 ± 0.12	0.61 ± 0.08	0.88 ± 0.12
RXCJ0516.7-5430	0.294	0.0686	6.4	6.7 ± 0.5	6.7 ± 0.5	0.25 ± 0.10	1.09 ± 0.15	0.80 ± 0.11	1.00 ± 0.15
RXCJ0528.9-3927	0.284	0.0212	5.8	6.6 ± 0.5	6.6 ± 0.5	0.20 ± 0.09	1.45 ± 0.15	0.88 ± 0.10	1.10 ± 0.15
RXCJ0532.9-3701	0.275	0.0290	7.0	8.2 ± 0.6	7.7 ± 0.6	0.28 ± 0.09	1.27 ± 0.12	0.55 ± 0.07	0.81 ± 0.12
RXCJ0547.6-3152	0.148	0.0205	7.7	6.1 ± 0.2	6.0 ± 0.2	0.22 ± 0.03	0.72 ± 0.06	0.39 ± 0.04	0.55 ± 0.06
RXCJ0645.4-5413	0.164	0.0651	8.1	8.1 ± 0.3	7.6 ± 0.3	0.11 ± 0.04	1.78 ± 0.16	1.01 ± 0.12	1.30 ± 0.16
RXCJ0658.5-5556	0.296	0.0653	8.9	11.1 ± 0.4	10.7 ± 0.4	0.14 ± 0.04	4.95 ± 0.24	2.99 ± 0.18	4.21 ± 0.24
RXCJ0945.4-0839	0.153	0.0359	7.6	5.7 ± 0.5	5.3 ± 0.5	0.11 ± 0.10	0.42 ± 0.06	0.24 ± 0.04	0.33 ± 0.06
RXCJ0958.3-1103	0.167	0.0540	7.4	6.1 ± 0.3	5.8 ± 0.3	0.27 ± 0.06	0.91 ± 0.09	0.42 ± 0.06	0.57 ± 0.09
RXCJ2129.6+0005	0.235	0.0428	6.8	6.4 ± 0.2	6.3 ± 0.2	0.27 ± 0.03	1.43 ± 0.09	0.58 ± 0.06	0.79 ± 0.09
RXCJ2218.6-3853	0.141	0.0138	7.3	6.7 ± 0.2	6.2 ± 0.2	0.27 ± 0.05	0.66 ± 0.05	0.34 ± 0.04	0.48 ± 0.05
RXCJ2234.5-3744	0.151	0.0122	7.9	7.8 ± 0.4	7.5 ± 0.4	0.22 ± 0.08	1.09 ± 0.11	0.57 ± 0.07	0.80 ± 0.11
RXCJ2308.3-0211	0.297	0.0445	7.3	7.7 ± 0.7	7.6 ± 0.7	0.41 ± 0.16	1.21 ± 0.13	0.56 ± 0.08	0.80 ± 0.13
RXCJ2337.6+0016	0.275	0.0382	7.0	8.0 ± 0.5	7.5 ± 0.5	0.19 ± 0.07	1.00 ± 0.09	0.54 ± 0.06	0.77 ± 0.09
Abell68	0.255	0.0493	6.1	7.7 ± 0.3	7.3 ± 0.3	0.12 ± 0.05	1.14 ± 0.10	0.61 ± 0.07	0.86 ± 0.10
Abell115	0.197	0.0543	8.0	6.4 ± 0.1	6.2 ± 0.1	0.20 ± 0.03	1.43 ± 0.11	1.05 ± 0.09	1.16 ± 0.11
Abell209	0.209	0.0164	7.4	7.1 ± 0.3	7.1 ± 0.3	0.22 ± 0.04	1.33 ± 0.11	0.84 ± 0.08	1.10 ± 0.11
Abell267	0.230	0.0280	5.3	6.5 ± 0.4	6.2 ± 0.4	0.25 ± 0.08	0.77 ± 0.07	0.36 ± 0.05	0.52 ± 0.07
Abell383	0.187	0.0392	7.7	5.3 ± 0.2	4.7 ± 0.2	0.18 ± 0.06	0.81 ± 0.05	0.27 ± 0.04	0.36 ± 0.05
Abell773	0.217	0.0144	7.7	8.1 ± 0.4	8.3 ± 0.4	0.30 ± 0.06	2.09 ± 0.16	1.06 ± 0.11	1.53 ± 0.16
Abell781	0.298	0.0194	6.5	6.4 ± 0.5	6.5 ± 0.5	0.18 ± 0.10	0.63 ± 0.10	0.52 ± 0.09	0.60 ± 0.10
Abell901	0.163	0.0499	4.6	3.6 ± 0.2	3.2 ± 0.2	0.12 ± 0.09	1.60 ± 0.05	0.35 ± 0.03	0.57 ± 0.05
Abell963	0.206	0.0140	6.1	6.3 ± 0.2	6.5 ± 0.2	0.28 ± 0.05	1.14 ± 0.09	0.55 ± 0.06	0.74 ± 0.09
Abell1413	0.143	0.0219	8.4	6.8 ± 0.1	6.6 ± 0.1	0.27 ± 0.03	1.38 ± 0.08	0.68 ± 0.06	0.93 ± 0.08
Abell1689	0.184	0.0182	8.0	8.4 ± 0.2	8.5 ± 0.2	0.26 ± 0.04	2.84 ± 0.10	0.93 ± 0.06	1.44 ± 0.10
Abell1758	0.280	0.0106	6.0	7.6 ± 0.2	7.9 ± 0.2	0.19 ± 0.04	1.05 ± 0.07	0.66 ± 0.05	0.94 ± 0.07
Abell1763	0.228	0.0936	7.5	6.3 ± 0.3	5.8 ± 0.3	0.20 ± 0.05	1.65 ± 0.15	1.14 ± 0.11	1.41 ± 0.15
Abell1835	0.253	0.0232	7.0	8.0 ± 0.3	8.4 ± 0.3	0.23 ± 0.04	5.32 ± 0.17	1.51 ± 0.10	2.25 ± 0.17
Abell1914	0.171	0.0095	8.2	8.6 ± 0.3	8.8 ± 0.3	0.19 ± 0.05	2.17 ± 0.11	0.62 ± 0.06	0.97 ± 0.11
Abell2204	0.152	0.0567	9.0	8.0 ± 0.2	7.6 ± 0.2	0.27 ± 0.03	3.39 ± 0.12	1.09 ± 0.08	1.52 ± 0.12
Abell2218	0.176	0.0324	7.7	7.4 ± 0.3	6.6 ± 0.3	0.21 ± 0.04	1.11 ± 0.08	0.68 ± 0.06	0.90 ± 0.08
Abell2261	0.224	0.0328	8.1	7.0 ± 0.6	6.6 ± 0.6	0.33 ± 0.18	1.39 ± 0.22	0.67 ± 0.13	0.91 ± 0.22
Abell2390	0.233	0.0680	7.7	10.6 ± 0.6	11.6 ± 0.6	0.24 ± 0.06	4.09 ± 0.27	1.95 ± 0.17	2.66 ± 0.27
Abell2667	0.230	0.0165	7.6	7.3 ± 0.3	7.0 ± 0.3	0.29 ± 0.04	2.16 ± 0.13	0.83 ± 0.08	1.14 ± 0.13
Z7160	0.258	0.0316	8.0	5.0 ± 0.1	4.7 ± 0.1	0.32 ± 0.04	1.70 ± 0.08	0.50 ± 0.05	0.67 ± 0.08

The global temperature and luminosity are uniformly calculated as described in Appendix B.2 and Appendix B.4 for all 37 LoCuSS clusters. In Zhang et al. (2006, 2007), the temperature and luminosity are defined differently.

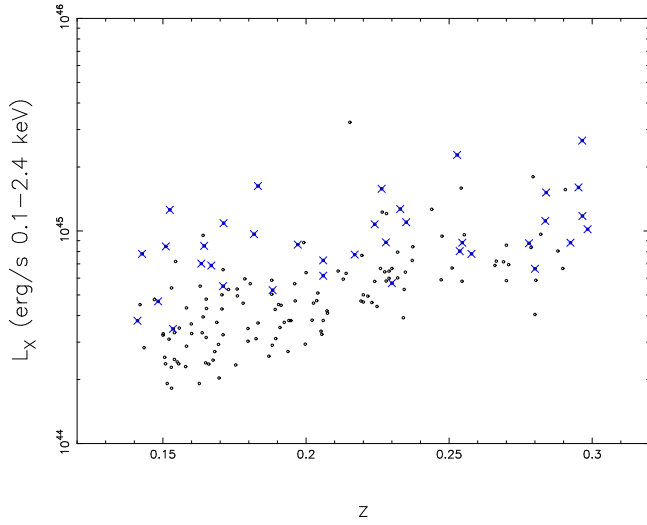


Fig. A.1. ROSAT luminosity versus redshift for the LoCuSS sample. The crosses denote the 37 LoCuSS clusters observed by *XMM-Newton*.

Appendix B: Scaled profiles of the X-ray properties: a structural similarity

Simulations (e.g. Navarro et al. 1997, 2004) suggest a self-similar structure for galaxy clusters within hierarchical structure formation scenarios. The scaled profiles of the X-ray properties and their scatter can be used to quantify the structural variations, to probe the regularity of galaxy clusters, and thus to understand the scatter in the X-ray scaling relations, which is of prime importance for cosmological applications involving clusters of galaxies.

Because the observational truncation radii (r_t) in the surface brightness profiles are above r_{500} but below r_{200} for most clusters in the sample, we use r_{500} for radial scaling.

The following redshift evolution corrections due to LSS growth are usually used to account for the dependence on the evolution of the cosmological parameters,

$$\begin{aligned} S_X \cdot E^{-3}(z) &\propto f(T), \\ S \cdot E^{4/3}(z) &\propto f(T), \\ P \cdot E^{-2}(z) &\propto f(T), \\ L \cdot E^{-1}(z) &\propto f(T), \\ M \cdot E(z) &\propto f(T), \\ M_{\text{gas}} \cdot E(z) &\propto f(T), \\ Y_X \cdot E(z) &\propto f(T), \\ r \cdot E(z) &\propto f(T), \end{aligned}$$

where $Y_X = M_{\text{gas}} \cdot T$ is an X-ray analog for the integrated SZ flux (e.g. Kravtsov et al. 2006; also see Sunyaev & Zeldovich 1972). The function $f(T)$ denotes the best-fit power law parameterization. $\Delta_{c,z}/\Delta_{c,0}$ factor³ is dropped out compared to the redshift evolution corrections used in Zhang et al. (2006, 2007) for convenience, and for easier comparison between our sample and published samples.

³ $\Delta_{c,z} = 18\pi^2 + 82(\Omega_{m,z} - 1) - 39(\Omega_{m,z} - 1)^2$ is the analytic approximation derived from the top-hat spherical collapse model for a flat Universe (Bryan & Norman 1998) and $\Omega_{m,z}$ the cosmic density parameter at redshift z .

B.1. Scaled temperature profiles

We scaled the radial temperature profiles by $T_{0.2-0.5r_{500}}$ and r_{500} (Fig. B.1). Within $0.2r_{500}$, we observed a temperature drop to at least 70 per cent of the maximum value towards the cluster center for 9 clusters (defined as CCCs). Previous observations have shown that temperature measurements on scales below $0.2r_{500}$ tend to show peculiarities linked to the cluster dynamical history (e.g. Finoguenov et al. 2005; Zhang et al. 2005a, 2005b). For example, the temperatures of merging clusters can be boosted (Smith et al. 2005, Poole et al. 2006, 2007). However, the boosting affects mainly the cluster cores. Using global temperatures excluding the $< 0.2r_{500}$ region can thus (1) tighten the scaled profiles of the X-ray properties, (2) reduce the scatter in the X-ray scaling relations, and (3) improve agreement between normalization of the X-ray scaling relations for the CCCs and non-CCCs, respectively.

We used the $1-\sigma$ boundary of the scaled radial temperature profiles to compute the confidence zone for the mean temperature profile. The average temperature profile for the whole sample gives $T(r) \propto r^{0.13 \pm 0.04}$, and for the CCC subsample $T(r) \propto r^{0.38 \pm 0.04}$, respectively, in the $r < 0.2r_{500}$ region. Because the temperature profiles are not PSF corrected, the significance of the cool cores could be more pronounced considering the PSF effects. The temperature behavior in the cluster cores for the CCC subsample is very similar to the behavior for the nearby CCC sample in Sanderson et al. (2006) giving $T(r) \propto r^{0.4}$ based on *Chandra* observations. In the outskirts ($0.2r_{500} < r < r_{500}$), the whole sample shows a structurally similar behavior giving $T(r) \propto r^{-0.28 \pm 0.19}$ with 30 per cent scatter. The average temperature profile decreases down to 80 per cent of the maximum value with intrinsic scatter of ~ 30 per cent at $\sim r_{500}$.

Studies of the cluster temperature distributions indicate a similar universal temperature profile with a significant decline beyond cluster cores in observations (e.g. Markevitch et al. 1998; De Grandi & Molendi 2002; Vikhlinin et al. 2005; Zhang et al. 2004, 2005a, 2006, 2007; Pratt et al. 2007) and simulations (e.g. Borgani et al. 2004).

Accurate temperature distributions (15 per cent uncertainties) are measured up to $0.5r_{500}$ for our sample. We found steepening of the average temperature distribution using the parameterization of the temperature distributions, giving slopes from 0.04 ± 0.03 at $0.2r_{500}$ to 0.16 ± 0.03 at $0.5r_{500}$ (the errors for the slope are the statistical formal errors). The slope should have been calculated from the observational data points for the temperature profile as done for the density profile based on a better spatially resolved temperature profile. With deep *Chandra* observations, Vikhlinin et al. (2005) found more significant steepening of the temperature distributions in the outskirts.

B.2. Global temperature

As indicated by the scaled temperature profiles for this sample and also explained in Zhang et al. (2007), the temperature measurements limited to $0.2-0.5r_{500}$ are less affected by the cool cores and are thus used as cluster global temperatures. We

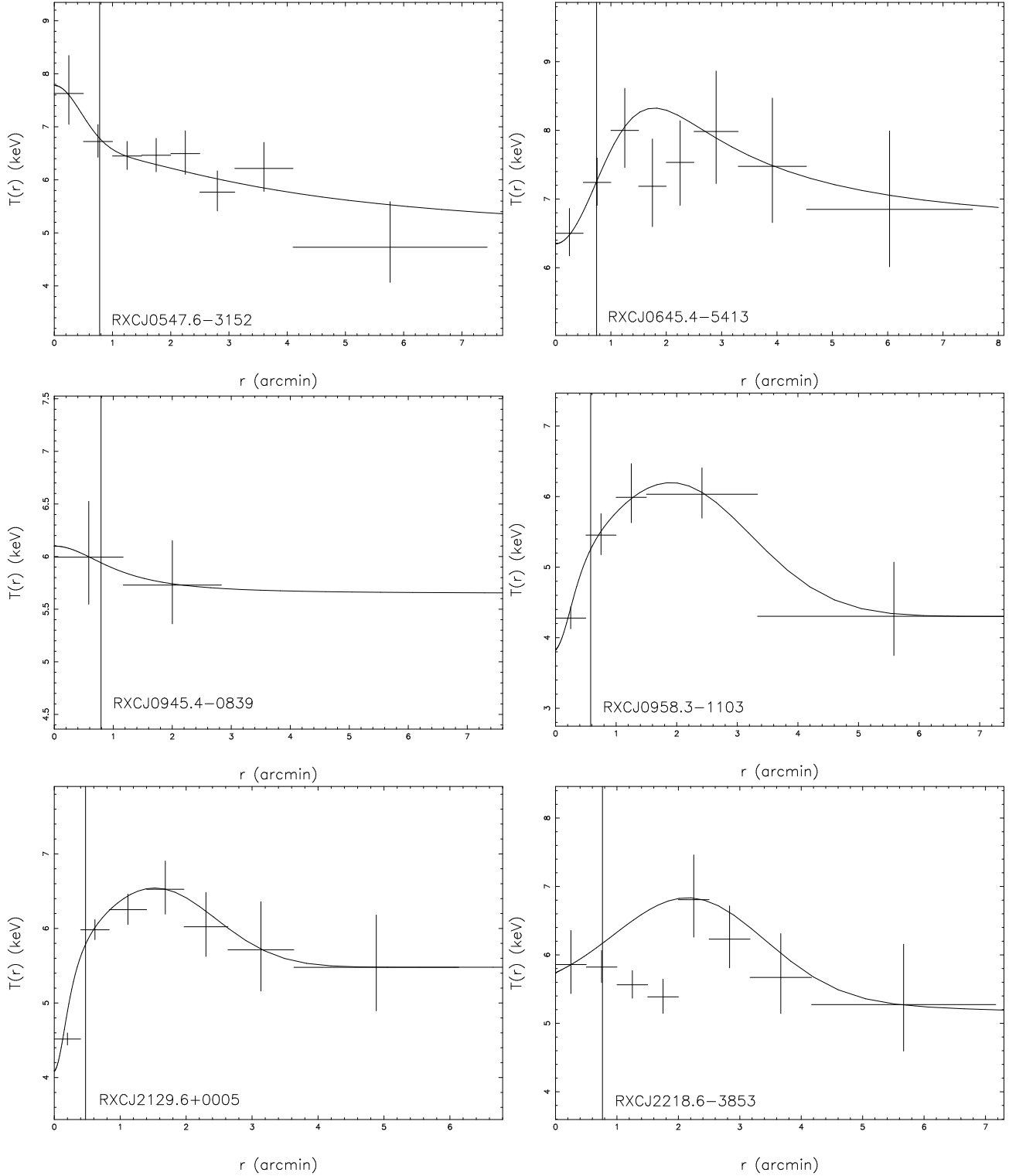


Fig. A.2. De-projected temperature profiles approximated by the parameterization $T(r) = P_3 \exp[-(r - P_1)^2/P_2] + P_6(1 + r^2/P_4^2)^{-P_5} + P_7$ crossing all the data points (solid). The vertical line denotes $0.1r_{500}$.

present the spectroscopic global temperature ($T_{0.2-0.5r_{500}}^{\text{spec}}$) and metallicity ($Z_{0.2-0.5r_{500}}^{\text{spec}}$) in the annulus of $0.2-0.5r_{500}$ together with the volume average of the radial temperature profile limited to the radial range of $0.2-0.5r_{500}$ ($T_{0.2-0.5r_{500}}$) in Table A.2. $T_{0.2-0.5r_{500}}$ is used as the cluster global temperature for stud-

ies of the structural similarity of the X-ray properties and the scaling relations. We present the spectral measurements, temperature versus metallicity, from all radial bins in Fig. B.3, and observed no obvious correlation between cluster temperature and metallicity though the mass range is relatively small.

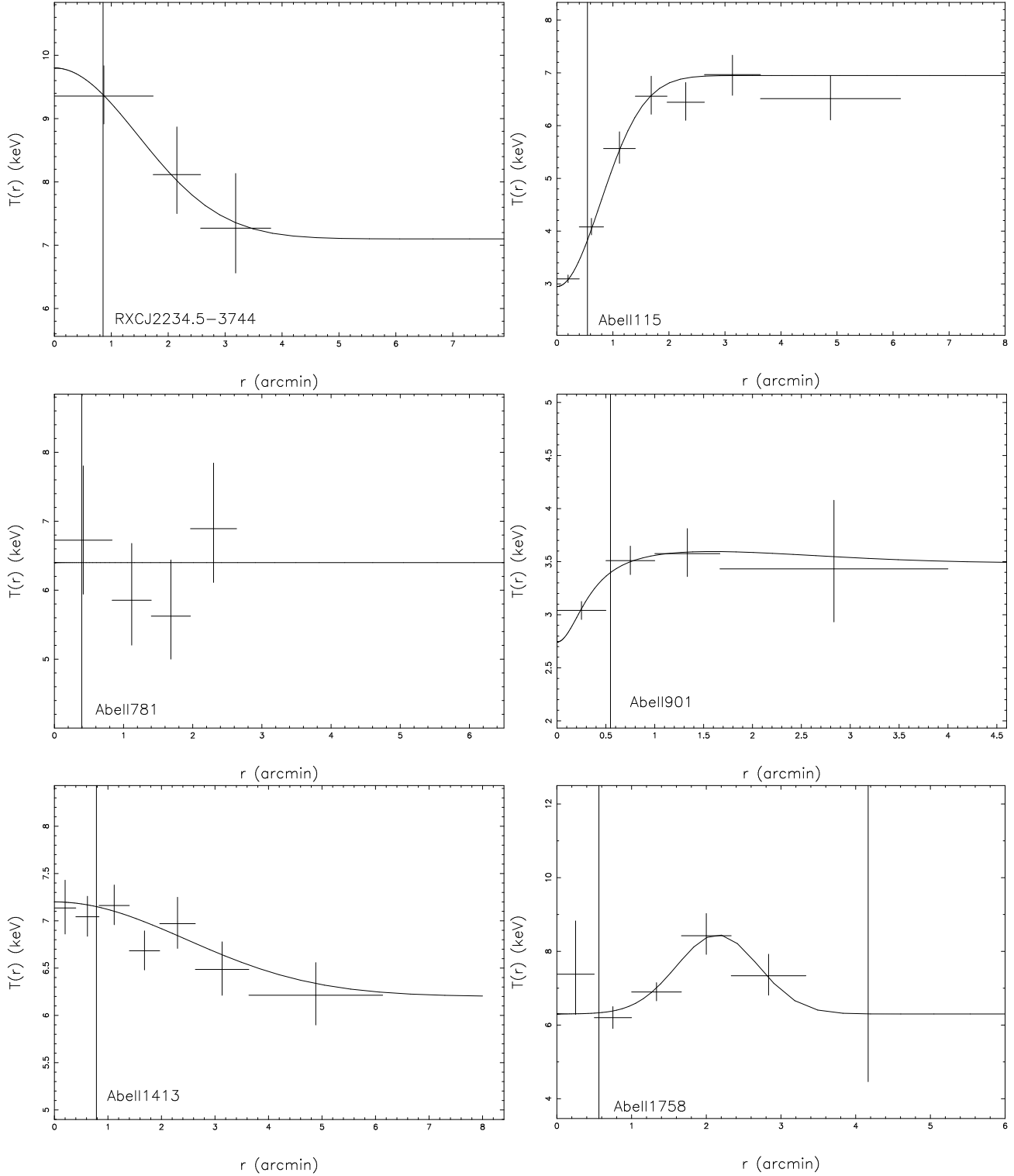


Fig. A.3. See caption in Fig. A.2.

B.3. Scaled surface brightness profiles

The standard self-similar model gives $S_X \propto \int_R^\infty n_e^2 dl \propto M_{\text{gas}}^2 \cdot M^{-5/3} \propto T^{0.5}$ as $M \propto M_{\text{gas}} \propto T^{1.5}$. The scaling becomes steeper ($S_X \propto T^{1.1}$) using the empirical relations ($M \propto T^{1.5}$ in e.g. Arnaud et al. 2005, $M_{\text{gas}} \propto T^{1.8}$ in e.g. Mohr et al. 1999; Vikhlinin et al. 1999). We present the empirical scaling $S_X \propto$

$T^{1.1}$ scaled surface brightness profiles in Fig. B.2. We found a less scattered structurally similar behavior at $R > 0.2r_{500}$ for the scaled surface brightness profiles compared to the profiles scaled by $S_X \propto T^{0.5}$.

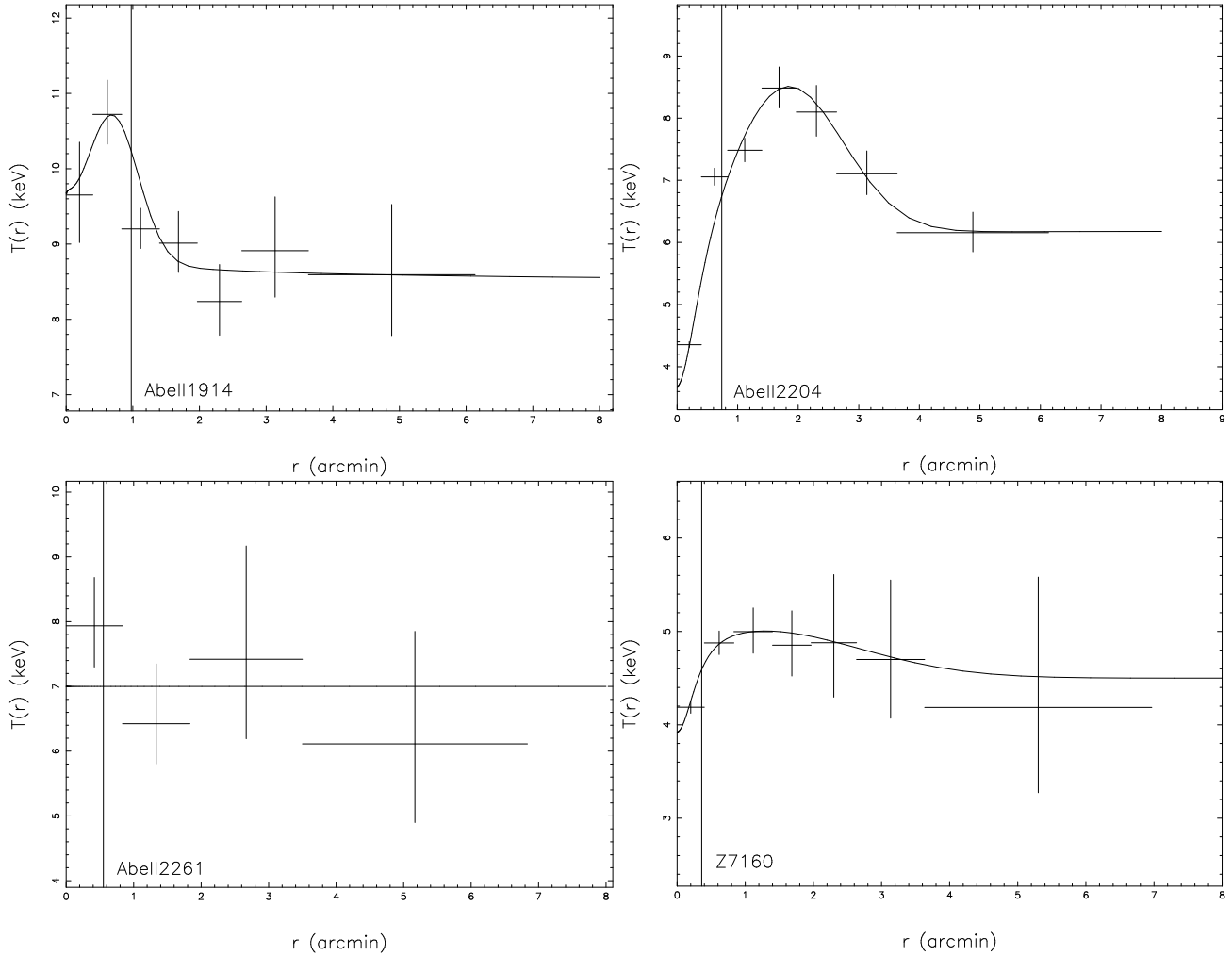


Fig. A.4. See caption in Fig. A.2.

B.4. Global luminosities

The bolometric X-ray luminosity (here we use the 0.01–100 keV band) is given by $L_{\text{bol}} \propto \int \tilde{\Lambda}(r)n_e^2(r)dV$, practically an integral of the X-ray surface brightness to $2.5r_{500}$ ($L_{\text{bol}}^{\text{incc}}$ in Table A.2). The value $2.5r_{500}$ is used because the virial radii are about $2.2\text{--}2.6r_{500}$ using our mass modeling. The luminosity varies by less than 10 per cent when setting the truncation radius to values between r_{500} and $2.5r_{500}$. The best-fit “mekal” model for the spectra extracted in the annulus limited to $0.2\text{--}0.5r_{500}$ is used to convert the count rate to real flux. Using different converting “mekal” models, e.g. different temperature ($T_{0.2\text{--}0.5r_{500}}$ or $T_{0.1\text{--}0.5r_{500}}^{\text{spec}}$ or $T_{0.2\text{--}0.5r_{500}}^{\text{spec}}$ or $T_{<2/3r_t}^{\text{spec}}$) and metallicity ($Z_{0.1\text{--}0.5r_{500}}^{\text{spec}}$ or $Z_{0.2\text{--}0.5r_{500}}^{\text{spec}}$ or $Z_{<2/3r_t}^{\text{spec}}$) causes up to 20 per cent difference in the X-ray luminosity, in which the difference is more significant for pronounced CCCs.

The core radii populate a broad range of values up to $0.2 r_{500}$. The X-ray luminosity is sensitive to the presence of a cool core. It can thus be used to probe the evolution of a cool cores. We present the bolometric luminosities including and excluding the $R < 0.2r_{500}$ region ($L_{\text{bol}}^{\text{incc}}$ and $L_{\text{bol}}^{\text{excc}}$ in Table A.2. The fractions of the X-ray luminosity attributed to

the $R < 0.2r_{500}$ region span a broad range up to ~ 80 per cent. This introduces large uncertainties in the use of the luminosity $L_{\text{bol}}^{\text{incc}}$ as a mass indicator. The X-ray luminosity excluding the $< 0.2r_{500}$ region ($L_{\text{bol}}^{\text{excc}}$) is much less dependent on the presence of the cool core. However, to better re-produce the cluster luminosity and the normalization of the luminosity–temperature/mass relation, we use the X-ray luminosity corrected for the cool core by assuming⁴ $S_X(R) = S_X(0.2r_{500})$ for the $R < 0.2r_{500}$ region ($L_{\text{bol}}^{\text{corr}}$ in Table A.2). Using $L_{\text{bol}}^{\text{corr}}$ for the X-ray scaling relations we obtain reduced scatter and consistent normalization for the CCCs and non-CCCs as shown later. The luminosity is lower (by up to 10 per cent) assuming a constant luminosity in the cluster core instead of a β model, especially for the pronounced CCCs. However, the luminosity corrected for the cool core by the β model still introduces relatively significant scatter dominated by the CCCs due to the correlation between core radius and slope in the β model.

⁴ This assumption was used only in the calculation for $L_{\text{bol}}^{\text{corr}}$, not for any other quantity.

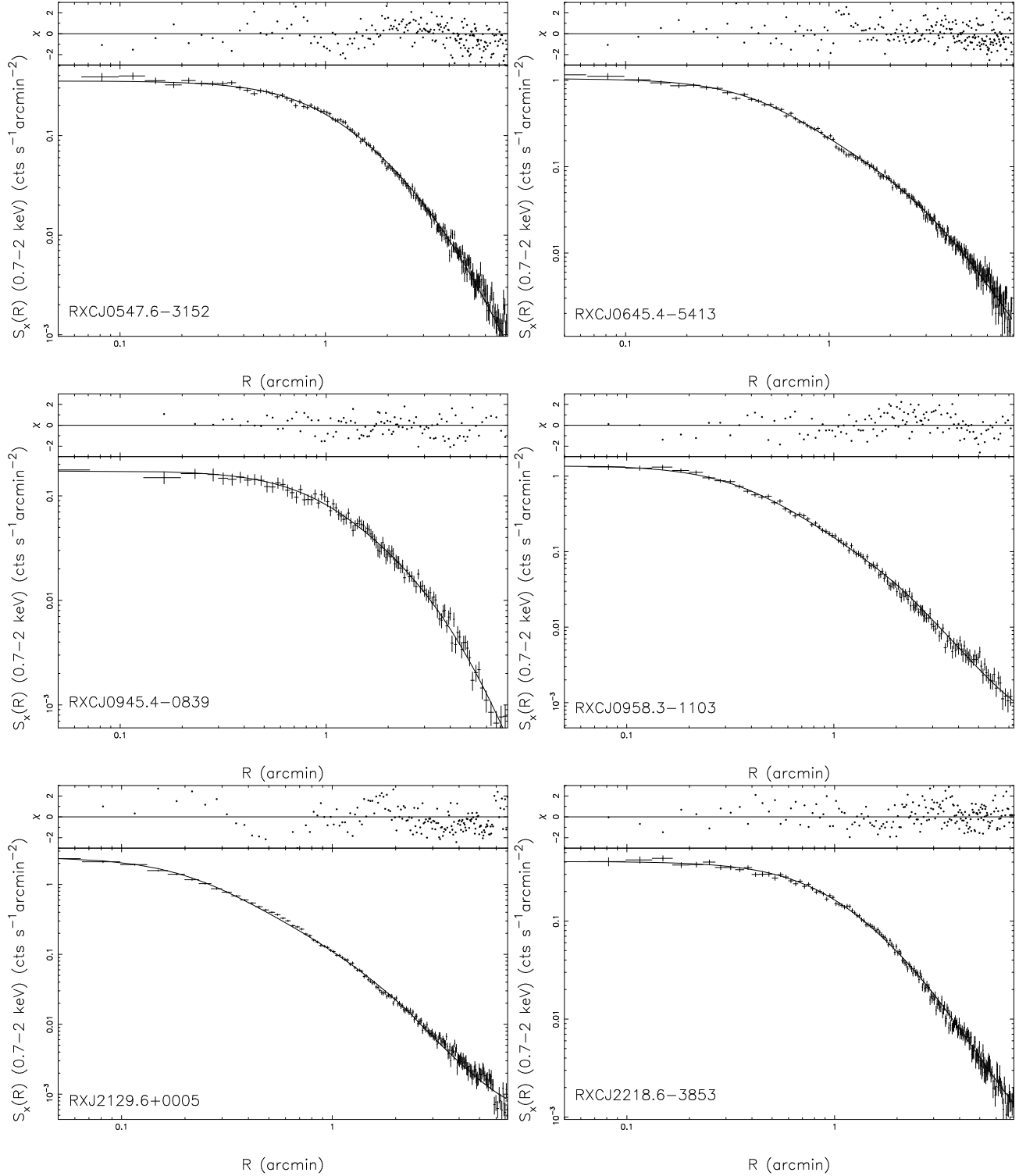


Fig. A.5. Surface brightness profiles parameterized by double- β model.

B.5. Gas profiles in the outskirts

The generally adopted β model ($\beta = 2/3$) gives $n_e \propto r^{-2}$. However, Vikhlinin et al. (1999) found a mild trend for β to increase as a function of cluster temperature, which gives $\beta \sim 0.80$ and $n_e \propto r^{-2.4}$ for clusters around 10 keV. Bahcall (1999) also found that the electron number density scales as

$n_e \propto r^{-2.4}$ at large radii. Zhang et al. (2006, 2007) confirmed their conclusion that $n_e \propto r^{-2.42}$ for the REFLEX-DXL clusters and $n_e \propto r^{-2.2 \pm 0.1}$ for the pilot LoCuSS sample. Due to the gradual change in the slope, one should be cautious when using a single slope double- β model which might introduce a systematic error in the cluster mass measurements (as also described in e.g. Horner 2001). The power law fit of the ICM density

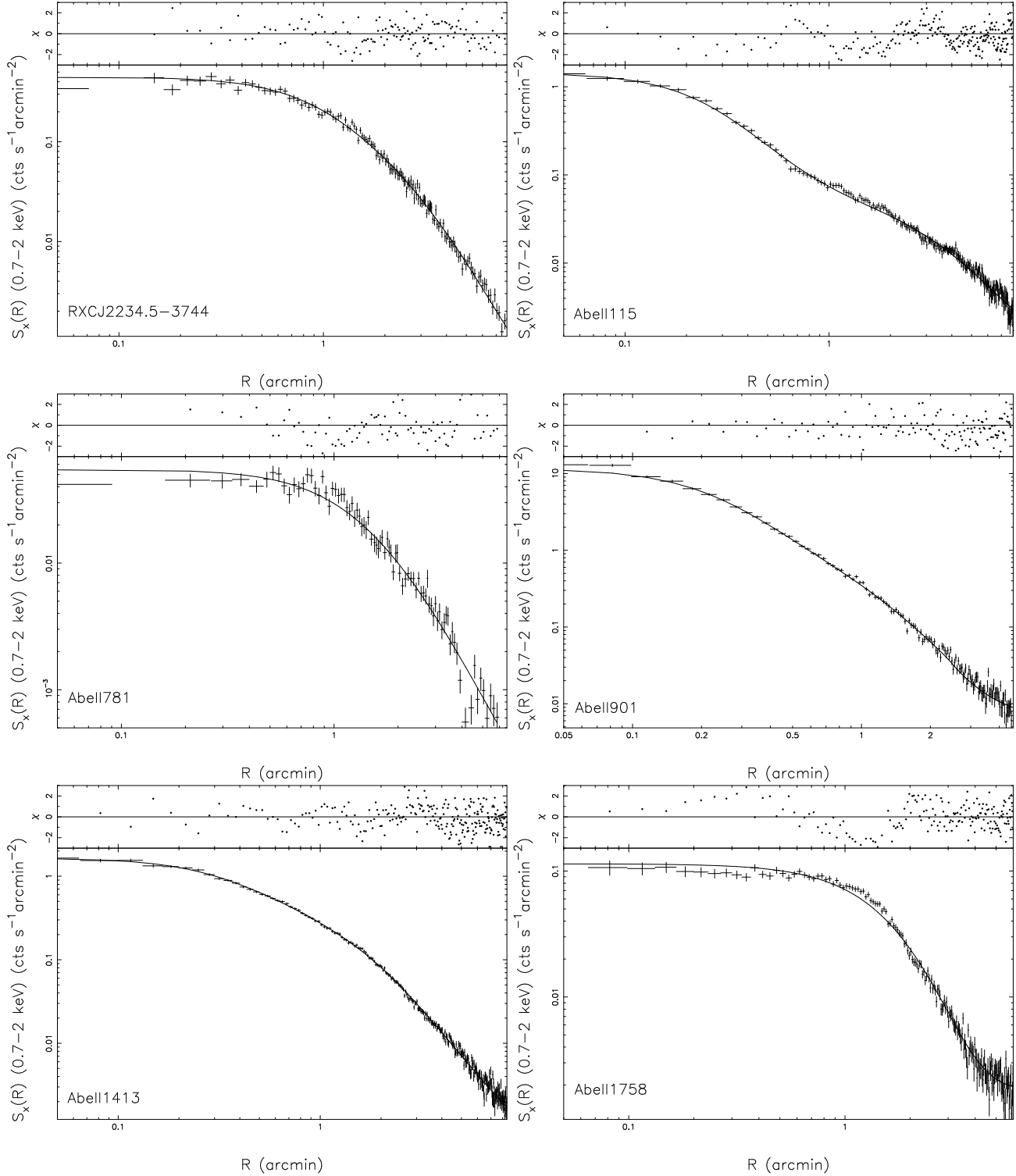


Fig. A.6. See caption in Fig. A.5.

distributions at r_{500} for the present sample gives an average of $n_e \propto r^{-2.21 \pm 0.05}$.

We made an additional attempt to check the difference in the mass modeling using a single- β model and a double- β model for CCCs caused by the steepening of the slope on large radial scales. We used a single- β model with the value of the core radius fixed to results for the outer component in the

double- β model to model the electron number density distribution. It often gives a higher value for the slope than the free fitting slope of the double- β model by a few per cent, and up to 10 per cent for the most pronounced CCC. Therefore the cluster total mass M_{500}^X can be higher by up to 20 per cent due to the steepening ICM density in the outskirts. To suppress this mass bias, we performed the modeling as follows. We first fitted the

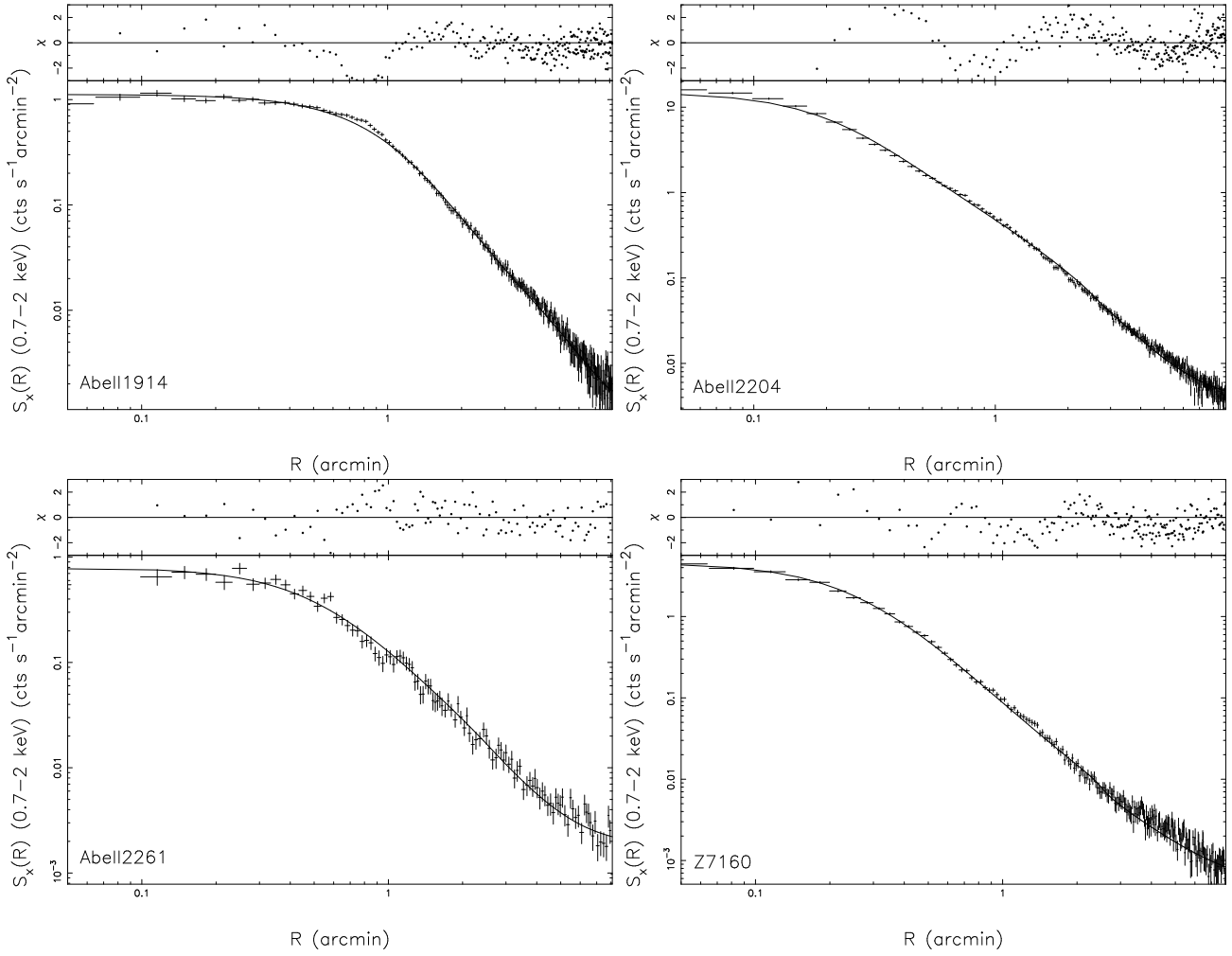


Fig. A.7. See caption in Fig. A.5.

outer region ($> 0.5r_{500}$) using a single- β model. We then fitted the whole radial range with a single slope, double- β model with its slope fixed to the best-fit value for the $> 0.5r_{500}$ region (cf. Appendix A.3). As the slope is locally fitted, there should not be a significant bias due to the beta slope steepening in our X-ray mass modeling. With deeper observations, the thing that can possibly be improved in the X-ray mass modeling to reduce the systematics is the slope of the temperature profile at r_{500} . However, the Monte-Carlo error estimation method accounts for this to some extent (also cf. Croston et al. 2007).

B.6. Scaled cooling time profiles

The cooling time is derived by the total energy of the gas divided by the energy loss rate

$$t_c = \frac{2.5n_g T}{n_e^2 \tilde{\Lambda}} \quad (\text{B.1})$$

where $\tilde{\Lambda}$, n_g , n_e and T are the radiative cooling function, gas number density, electron number density and temperature, respectively. We compute the upper limit of the age of the cluster as an integral from the cluster redshift z up to $z = 100$.

Cooling regions are those showing cooling time less than the upper limit of the cluster age. The boundary radius of such a region is called the cooling radius. The cooling radius is zero when the cooling time in the cluster center is larger than the upper limit of the cluster age. The cooling time at the resolved inner most radii of the surface brightness profiles and cooling radii are given in Table B.1.

In Fig. B.3, we show the cooling time profiles with their radii scaled to r_{500} . The CCCs show larger cooling radii in units of r_{500} , and show much shorter central cooling times than the non-CCCs. The scaled cooling time profiles show a structurally similar behavior above $0.2r_{500}$ for the sample. The best-fit power law above $0.2r_{500}$ gives $t_c(r) \propto r^{1.58 \pm 0.01}$ for the whole sample. The cooling time profiles within $0.2r_{500}$ show large scatter spreading over 2 magnitudes without showing pronounced CCC and non-CCC bimodal distribution. Similar studies for nearby clusters based on *Chandra* data can be found in Sanderson et al. (2006) and Dunn & Fabian (2006).

The cooling time is calculated towards the cluster center to the inner most bin for which the surface brightness profile is resolved. There can be large uncertainties in the cooling time at the inner most bins where the temperature measurements are

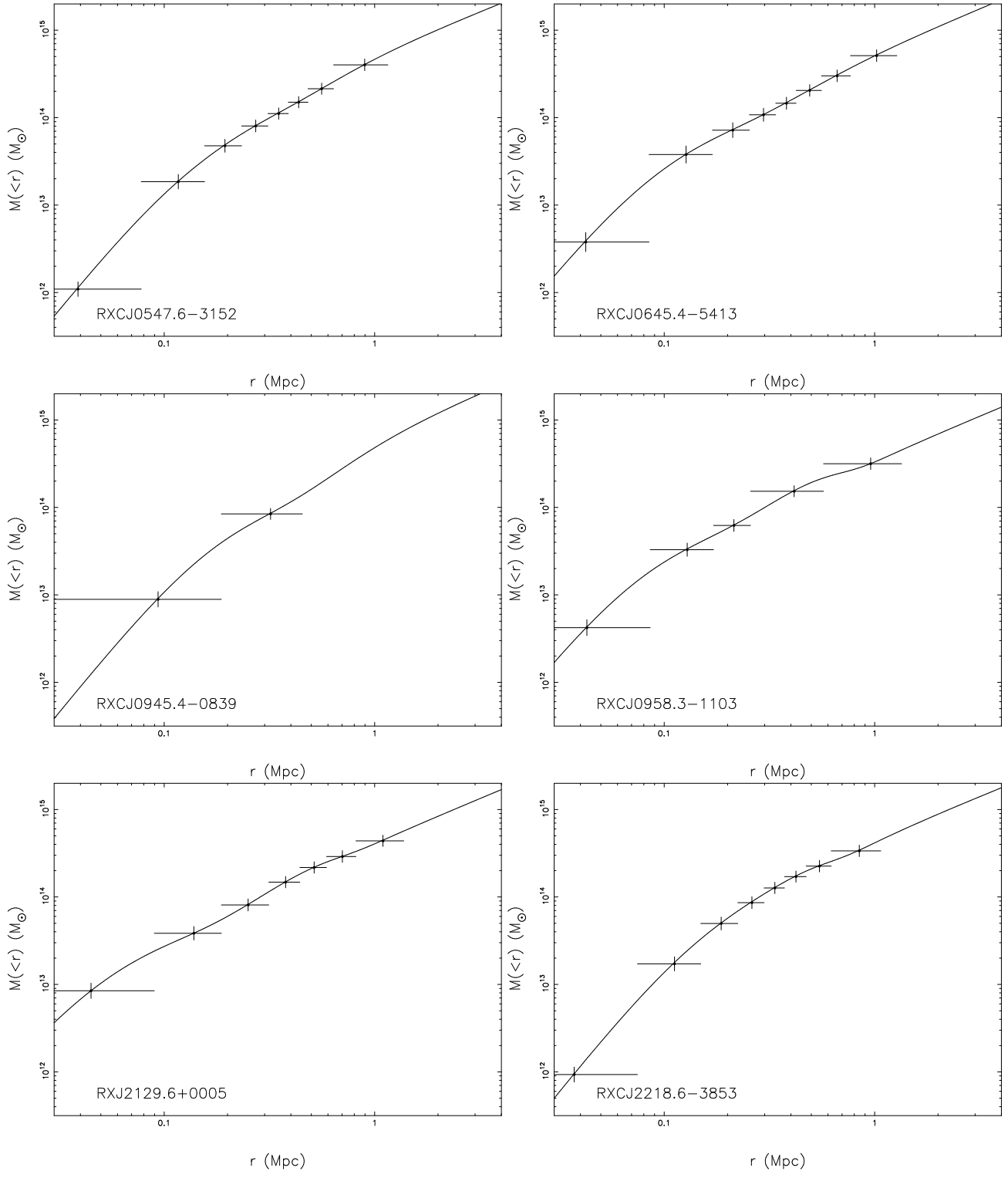


Fig. A.8. Mass profiles with their mass data points binned as the temperature measurements to demonstrate the error bars.

not resolved. The spatial resolution is important to calculate the proper cooling time in the cluster center. When the cluster core is not well resolved, the value calculated from the measured temperature and electron number density gives the upper limit of the cooling time, especially for the CCCs, which show sharply peaked surface brightness profiles.

B.7. Scaled entropy profiles

The entropy is the key to the understanding of the thermodynamical history since it results from shock heating of the gas during cluster formation. The observed entropy is generally defined as $S = Tn_e^{-2/3}$ for clusters (e.g. Ponman et al. 1999). Radiative cooling can raise the entropy of the ICM (e.g. Pearce

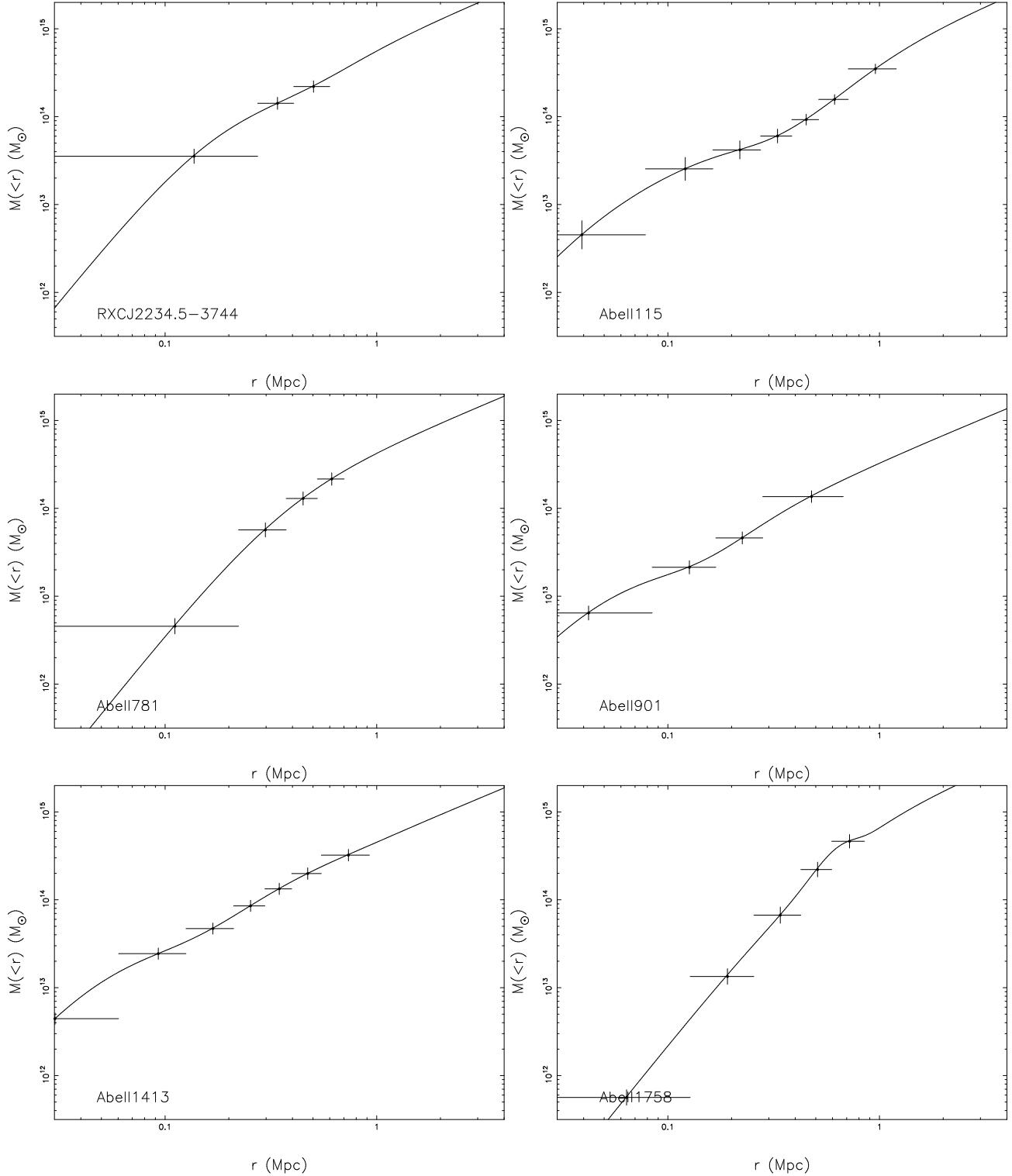


Fig. A.9. See caption in Fig. A.8.

et al. 2000) or produce a deficit below the S – T relation from the self-similar prediction (e.g. Lloyd-Davies et al. 2000).

According to the standard self-similar model the entropy scales as $S \propto T$ (e.g. Ponman et al. 1999). We investigated the entropy–temperature relation (S – T) using $S_{0.2r_{500}}$ as the central entropy and $T_{0.2-0.5r_{500}}$ as the cluster temperature. The CCCs

show slightly lower central entropies compared to the S – T scaling law.

Ponman et al. (2003) suggested to scale the entropy as $S \propto T^{0.65}$ based on observations for nearby clusters. We show the S – T relations in Fig. B.4 and Table B.2. The $S_{0.2r_{500}}$ – T relation ($S_{0.2r_{500}} \propto T^{1.32 \pm 0.16}$) for our sample agrees better with the stan-

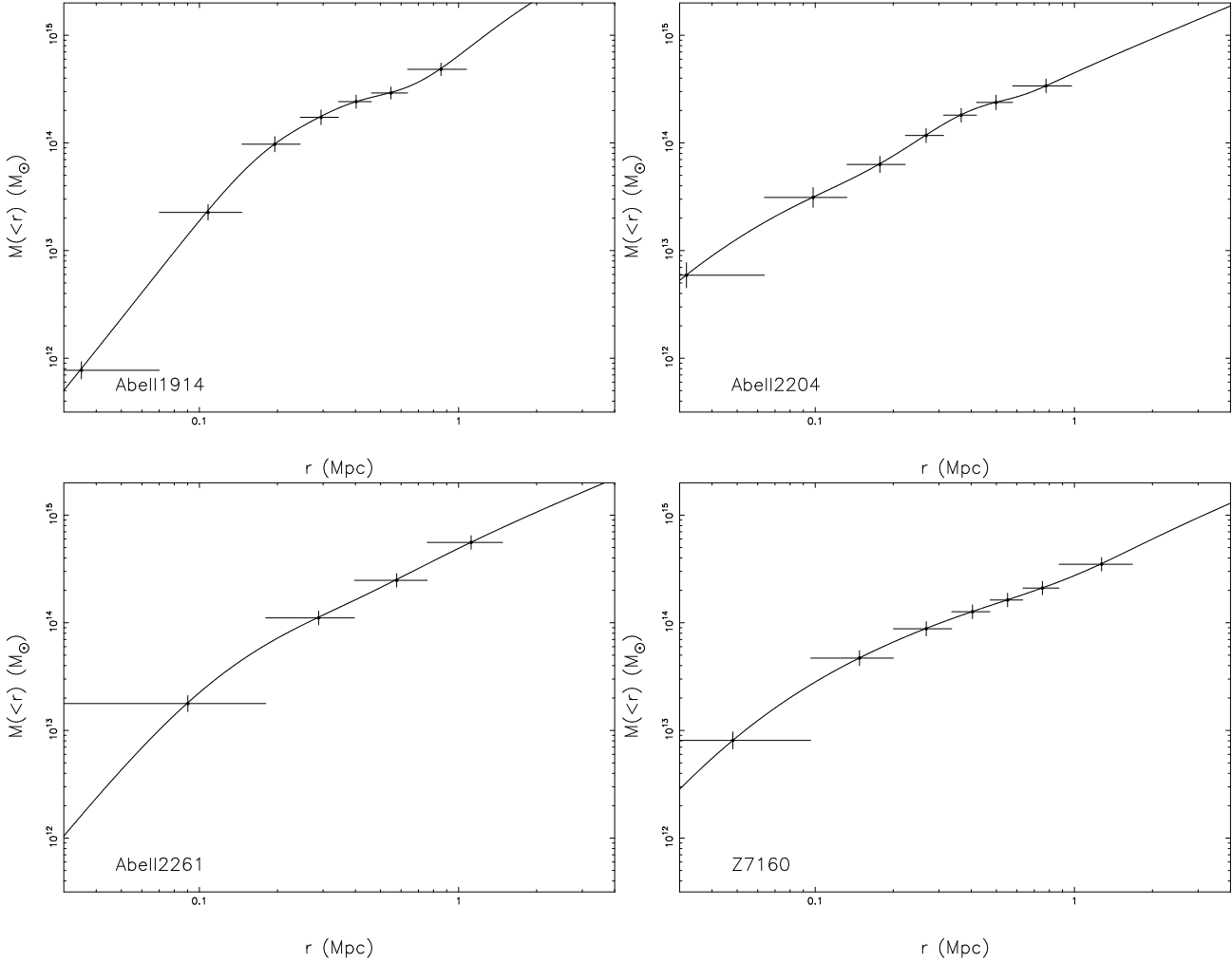


Fig. A.10. See caption in Fig. A.8.

standard self-similar model $S \propto T$. The CCCs ($S_{0.2r_{500}} \propto T^{0.63 \pm 0.20}$) show better agreement with the empirically determined scaling (Ponman et al. 2003) $S \propto T^{0.65}$. The $S-T$ relation becomes less steep using the entropies at $0.3r_{500}$ (Fig. B.4). Pratt et al. (2006) found that further away from the cluster center, the scatter in the entropy of the $S-T$ relation decreases. This is not evident for our sample due to the limited radial temperature bins. There is no noticeable evolution in the $S-T$ relation (e.g. using $S_{0.3r_{500}}$) comparing our sample to the nearby relaxed cluster sample in Pratt et al. (2006) after the redshift evolution correction due to LSS growth has been applied.

As $S \propto T$ and $M_{\text{gas}} \propto T^{1.5}$ according to the standard self-similarity, one derives $S \propto (TM_{\text{gas}})^{0.5} \propto Y_X^{0.5}$. In Fig. B.4, we present both the entropy and the pressure at $0.2r_{500}$, $0.3r_{500}$ and r_{500} versus X-ray analog of the SZ flux. The best-fit power law is given in Table B.2. The CCCs show large scatter in $S-T$, $S-Y_X$ and $P-Y_X$ relations. The $P-Y_X$ relations show least segregation between CCCs and non-CCCs, especially at r_{500} .

We scaled the radial entropy profiles using the empirically scaling (Ponman et al. 2003) $S \propto T^{0.65}$ and r_{500} . As shown in Fig. B.5, the scaled entropy profiles for the sample are structurally similar above $0.2r_{500}$ and show least scatter around $0.2-$

$0.5r_{500}$. After the redshift correction, we obtained an agreement between the scaled entropy profiles for this sample, the Birmingham-CfA sample (Ponman et al. 2003), and the cluster sample in Pratt et al. (2006). There is no evident evolution in the scaled entropy profiles after the redshift evolution correction due to LSS growth has been applied.

The scaled entropy profiles for our sample give the best fit $S(r) \propto r^{1.00 \pm 0.03}$ above $0.2r_{500}$. A similar power law was also found as $S \propto r^{0.97}$ by Ettori et al. (2002), and $S \propto r^{0.95}$ by Piffaretti et al. (2005), respectively. The spherical accretion shock model predicts $S \propto r^{1.1}$ (e.g. Tozzi & Norman 2001; Kay 2004). The combined fit of the entropy profiles for the 9 CCCs in our sample gives $S \propto r^{1.05 \pm 0.04}$, close to the prediction of the spherical accretion shock model and consistent with the relaxed nearby clusters in Pratt et al. (2006) giving $S \propto r^{1.08}$.

B.8. Scaled total mass and gas mass profiles

The mass profiles were scaled with respect to M_{500}^X and r_{500} , respectively (Fig. B.6). We found least scatter at radii above $0.2r_{500}$. In the inner regions ($< 0.2r_{500}$), the mass profiles show large scatter spreading one magnitude. This might be due to

the complex dynamics near the cluster center. As found in the strong lensing studies based on high quality HST data (Smith et al. 2005), the cluster cores can be very complicated with multi-clump DM halos.

Similar to the mass profiles, the scaled gas mass profiles appear structurally similar at radii above $0.2r_{500}$ but show smaller scatter (a few per cent) than the scaled mass profiles.

B.9. Summary of the structural similarity

In summary, we observed the structural similarity of the scaled profiles of the X-ray properties outside the cluster cores. It supports simulations that major mergers are not common recently (e.g. Cohn & White 2005), while the structurally similar behavior shows an empirical structural similarity, which is in agreement with simulations (e.g. Poole et al. 07) that the signatures of merger impact are retained by the cluster for a substantial fraction of cosmic time.

There is large scatter in the cluster cores for the scaled profiles of the X-ray properties, but no pronounced CCC and non-CCC bimodal distributions. The peculiarities in the cluster cores for the individual clusters may explain the large scatter in the scaled profiles within cluster cores where the ICM does not always trace DM.

As found in Majerowicz et al. (2002), the cluster total mass for the pronounced CCC Abell 1835 is lower by less than 10 per cent than the mass derived ignoring the temperature drop in the cluster center. Therefore the cluster total masses on large radial scales are relatively insensitive to the cluster cores. The scaling relations can be less sensitive to the peculiarities in the cluster cores by (1) measuring the global temperatures excluding the cluster cores, (2) and calculating the luminosities corrected for the cluster cores.

**Appendix C: Mass–observable relations at
different radius**

Table B.1. Deduced properties of 37 LoCuSS galaxy clusters. Column (1): cluster name; Col. (2): electron number density of the inner most radial bin; Col. (3): entropy at $0.2r_{500}$; Col. (4): inner most radial bin of the surface brightness profile; Col. (5): cooling time measured at r_{cen} ; Col. (6): cooling radius; Col. (7): r_{500} ; Cols. (8–10): gas mass, total mass and gas mass fraction at r_{500} , Col. (11): cluster morphology using the cluster classification in Jones & Forman (1992), 0 denotes “single”, 1 denotes “primary with small secondary”, 2 denotes “elliptical”, 3 denotes “off-center” and 4 denotes “complex”.

Name	n_{e0}	$S_{0.2r_{500}}$	r_{cen}	t_c	r_{cool}	r_{500}	$M_{\text{gas},500}$	M_{500}^X	$f_{\text{gas},500}$	Mor.
	10^{-3} cm^{-3}	keV cm^2	kpc	Gyr	r_{500}	Mpc	$10^{14} M_{\odot}$	$10^{14} M_{\odot}$		
RXCJ0043.4-2037	5.8 ± 0.4	391 ± 23	8.76	7.8 ± 0.3	0.11	1.08	0.58 ± 0.06	4.83 ± 1.43	0.121 ± 0.066	2
RXCJ0232.2-4420	14.1 ± 0.1	402 ± 16	47.14	3.3 ± 0.2	0.14	1.30	0.89 ± 0.09	8.43 ± 2.48	0.106 ± 0.057	1
RXCJ0307.0-2840	10.2 ± 0.3	359 ± 22	12.01	3.6 ± 0.3	0.15	1.14	0.62 ± 0.06	5.47 ± 2.01	0.113 ± 0.083	0 ^c
RXCJ0516.7-5430	2.9 ± 0.2	474 ± 29	17.59	15.5 ± 0.4	0.00	1.19	0.78 ± 0.09	6.40 ± 1.83	0.121 ± 0.068	2
RXCJ0528.9-3927	10.6 ± 0.4	423 ± 25	12.87	4.2 ± 0.3	0.12	1.19	0.87 ± 0.07	6.40 ± 1.87	0.135 ± 0.071	3
RXCJ0532.9-3701	13.2 ± 0.5	555 ± 38	8.38	3.3 ± 0.3	0.12	1.13	0.57 ± 0.07	5.40 ± 1.59	0.106 ± 0.062	0
RXCJ0547.6-3152	5.3 ± 0.2	433 ± 31	2.32	8.3 ± 0.3	0.10	1.21	0.57 ± 0.07	5.84 ± 1.73	0.098 ± 0.058	0
RXCJ0645.4-5413	14.9 ± 1.0	513 ± 38	1.78	2.7 ± 0.3	0.12	1.26	0.90 ± 0.11	6.60 ± 1.95	0.136 ± 0.080	2
RXCJ0658.5-5556	6.1 ± 0.2	495 ± 26	8.84	8.2 ± 0.2	0.11	1.42	1.76 ± 0.17	10.99 ± 5.31	0.160 ± 0.178	3
RXCJ0945.4-0839	3.8 ± 0.2	500 ± 37	3.37	10.3 ± 0.2	0.05	1.27	0.49 ± 0.07	6.73 ± 1.95	0.073 ± 0.043	2
RXCJ0958.3-1103	21.6 ± 0.9	337 ± 22	2.56	1.4 ± 0.3	0.16	0.99	0.43 ± 0.05	3.29 ± 0.97	0.132 ± 0.077	2 ^c
RXCJ2129.6+0005	50.4 ± 1.4	332 ± 22	2.36	0.6 ± 0.3	0.16	1.06	0.56 ± 0.06	4.33 ± 1.27	0.130 ± 0.073	0 ^c
RXCJ2218.6-3853	6.2 ± 0.3	450 ± 32	2.22	6.1 ± 0.3	0.12	1.14	0.47 ± 0.06	4.83 ± 1.42	0.097 ± 0.058	2
RXCJ2234.5-3744	6.0 ± 0.3	580 ± 45	3.33	8.2 ± 0.3	0.08	1.35	0.76 ± 0.11	8.11 ± 2.36	0.094 ± 0.057	1
RXCJ2308.3-0211	9.2 ± 0.3	486 ± 49	13.27	5.0 ± 0.3	0.11	1.24	0.65 ± 0.07	7.42 ± 2.28	0.088 ± 0.051	0
RXCJ2337.6+0016	5.7 ± 0.3	710 ± 43	12.59	8.2 ± 0.3	0.05	1.43	0.81 ± 0.07	10.95 ± 3.22	0.074 ± 0.039	3
Abell68	6.4 ± 0.3	487 ± 35	3.55	6.6 ± 0.2	0.10	1.21	0.68 ± 0.07	6.51 ± 1.93	0.105 ± 0.060	2
Abell115	35.4 ± 1.4	430 ± 19	2.06	0.8 ± 0.2	0.12	1.07	0.69 ± 0.04	4.23 ± 1.14	0.163 ± 0.072	4 ^c
Abell209	5.7 ± 0.2	369 ± 26	3.74	6.3 ± 0.3	0.14	1.15	0.78 ± 0.08	5.33 ± 1.71	0.146 ± 0.089	0
Abell267	7.4 ± 0.4	364 ± 32	3.29	4.9 ± 0.4	0.15	1.06	0.47 ± 0.04	4.29 ± 1.30	0.109 ± 0.060	2
Abell383	54.8 ± 1.5	302 ± 14	1.98	0.5 ± 0.2	0.16	0.98	0.33 ± 0.04	3.17 ± 0.94	0.104 ± 0.061	0 ^c
Abell773	7.4 ± 0.4	433 ± 40	3.15	5.7 ± 0.5	0.14	1.33	1.05 ± 0.12	8.30 ± 2.45	0.126 ± 0.070	0
Abell781	1.8 ± 0.1	536 ± 61	6.28	22.1 ± 1.1	0.00	1.05	0.48 ± 0.06	4.49 ± 1.33	0.107 ± 0.064	4
Abell901	113.6 ± 1.7	158 ± 10	1.78	0.2 ± 0.4	0.24	0.99	0.44 ± 0.07	3.22 ± 0.96	0.137 ± 0.085	0
Abell963	14.3 ± 0.8	393 ± 18	2.14	2.6 ± 0.2	0.14	1.14	0.62 ± 0.06	5.19 ± 1.52	0.120 ± 0.066	0
Abell1413	25.3 ± 1.0	400 ± 23	1.59	1.7 ± 0.3	0.14	1.18	0.68 ± 0.08	5.38 ± 1.57	0.127 ± 0.073	2
Abell1689	30.0 ± 0.9	505 ± 24	1.95	1.5 ± 0.2	0.13	1.44	1.05 ± 0.14	10.26 ± 2.96	0.102 ± 0.060	0
Abell1758	2.4 ± 0.2	487 ± 39	3.80	16.7 ± 0.3	0.00	1.43	0.85 ± 0.14	11.15 ± 3.37	0.077 ± 0.050	2
Abell1763	6.5 ± 0.3	402 ± 47	4.00	6.1 ± 0.5	0.13	1.12	0.88 ± 0.08	4.96 ± 1.46	0.178 ± 0.094	1
Abell1835	63.9 ± 1.3	351 ± 22	2.50	0.6 ± 0.3	0.18	1.30	1.18 ± 0.14	8.01 ± 2.32	0.148 ± 0.084	0 ^c
Abell1914	10.5 ± 0.5	629 ± 56	1.84	4.7 ± 0.3	0.11	1.71	1.19 ± 0.13	16.76 ± 4.87	0.071 ± 0.039	3
Abell2204	143.7 ± 2.3	401 ± 28	1.68	0.2 ± 0.3	0.17	1.17	0.84 ± 0.10	5.31 ± 1.52	0.158 ± 0.086	0 ^c
Abell2218	5.8 ± 0.2	444 ± 50	3.26	8.0 ± 0.5	0.12	1.07	0.61 ± 0.06	4.18 ± 1.27	0.147 ± 0.085	0
Abell2261	12.4 ± 0.9	408 ± 49	3.95	3.4 ± 0.5	0.14	1.19	0.69 ± 0.10	6.02 ± 1.73	0.114 ± 0.068	0
Abell2390	40.3 ± 1.6	484 ± 33	2.31	0.9 ± 0.3	0.14	1.29	1.22 ± 0.16	7.67 ± 2.28	0.159 ± 0.095	0 ^c
Abell2667	40.8 ± 1.4	398 ± 27	2.33	0.8 ± 0.3	0.15	1.19	0.77 ± 0.09	6.02 ± 1.74	0.128 ± 0.073	0 ^c
Z7160	65.1 ± 1.5	218 ± 13	2.53	0.5 ± 0.3	0.21	0.87	0.39 ± 0.03	2.39 ± 0.70	0.161 ± 0.084	0
Average	—	—	—	—	—	—	—	—	0.121 ± 0.004	

1. The errors are calculated using the uncertainties of the electron number density and temperature measurements by Monte Carlo simulations. For each cluster, we simulated electron density and temperature profiles of a sample of 100 clusters using observed electron density and temperature profiles. The mass profiles and other properties of the 100 simulated clusters were calculated to derive the errors. In Zhang et al. (2006), the errors are simply propagated for the REFLEX-DXL clusters.

2. ^c in Col. (11) denotes CCCs.

Table B.2. Power law, $Y = Y_0 X^\gamma$, parameterized entropy–temperature, entropy– Y_X and pressure– Y_X relations.

X	Y	Y_0	γ	Scatter (dex)				Sample
				mean		average		
				X	Y	X	Y	
$\frac{T_{0.2-0.5r_{500}}}{\text{keV}}$	$\frac{S_{0.2r_{500}}}{\text{keV cm}^2} E(z)^{4/3}$	$10^{1.55 \pm 0.13}$	1.32 ± 0.16	0.03	0.03	0.05	0.06	whole sample
		$10^{1.45 \pm 0.15}$	1.45 ± 0.17	0.03	0.03	0.04	0.06	non-CCC subsample
		$10^{2.09 \pm 0.17}$	0.63 ± 0.20	0.31	0.18	0.15	0.09	CCC subsample
$\frac{T_{0.2-0.5r_{500}}}{\text{keV}}$	$\frac{S_{0.3r_{500}}}{\text{keV cm}^2} E(z)^{4/3}$	$10^{2.01 \pm 0.10}$	0.97 ± 0.11	0.03	0.03	0.05	0.05	whole sample
		$10^{1.87 \pm 0.11}$	1.14 ± 0.13	0.03	0.03	0.04	0.04	non-CCC subsample
		$10^{2.46 \pm 0.14}$	0.44 ± 0.17	0.13	0.16	0.13	0.06	CCC subsample
$\frac{T_{0.2-0.5r_{500}}}{\text{keV}}$	$\frac{S_{r_{500}}}{\text{keV cm}^2} E(z)^{4/3}$	$10^{2.57 \pm 0.22}$	1.00 ± 0.26	0.21	0.23	0.10	0.22	whole sample
		$10^{2.44 \pm 0.27}$	1.18 ± 0.32	0.04	0.23	0.09	0.22	non-CCC subsample
		$10^{2.90 \pm 0.27}$	0.54 ± 0.32	0.38	0.41	0.23	0.22	CCC subsample
$\frac{Y_X}{M_\odot \text{keV}} E(z)$	$\frac{S_{0.2r_{500}}}{\text{keV cm}^2} E(z)^{4/3}$	$10^{-5.53 \pm 1.27}$	0.56 ± 0.09	0.07	0.10	0.15	0.08	whole sample
		$10^{-6.69 \pm 1.61}$	0.64 ± 0.11	0.18	0.03	0.12	0.08	non-CCC subsample
		$10^{-5.63 \pm 0.90}$	0.22 ± 0.06	0.29	0.10	0.45	0.10	CCC subsample
$\frac{Y_X}{M_\odot \text{keV}} E(z)$	$\frac{S_{0.3r_{500}}}{\text{keV cm}^2} E(z)^{4/3}$	$10^{-2.50 \pm 0.82}$	0.36 ± 0.06	0.09	0.03	0.17	0.06	whole sample
		$10^{-3.80 \pm 1.07}$	0.45 ± 0.07	0.08	0.03	0.15	0.06	non-CCC subsample
		$10^{6.25 \pm 0.79}$	1.50 ± 0.05	0.32	0.14	0.42	0.07	CCC subsample
$\frac{Y_X}{M_\odot \text{keV}} E(z)$	$\frac{S_{r_{500}}}{\text{keV cm}^2} E(z)^{4/3}$	$10^{-1.91 \pm 1.44}$	0.36 ± 0.10	0.09	0.23	0.68	0.22	whole sample
		$10^{-3.15 \pm 1.87}$	0.54 ± 0.32	0.11	0.23	0.23	0.21	non-CCC subsample
		$10^{0.67 \pm 1.53}$	0.18 ± 0.10	0.22	0.42	0.27	0.22	CCC subsample
$\frac{Y_X}{M_\odot \text{keV}} E(z)$	$\frac{P_{0.2r_{500}}}{\text{keV cm}^{-3}} E(z)^{-2}$	$10^{-9.26 \pm 1.31}$	0.50 ± 0.09	0.05	0.08	0.18	0.10	whole sample
		$10^{-8.43 \pm 1.50}$	0.44 ± 0.10	0.08	0.08	0.20	0.10	non-CCC subsample
		$10^{-10.90 \pm 2.83}$	0.61 ± 0.19	0.22	0.20	0.17	0.10	CCC subsample
$\frac{Y_X}{M_\odot \text{keV}} E(z)$	$\frac{P_{0.3r_{500}}}{\text{keV cm}^{-3}} E(z)^{-2}$	$10^{-8.95 \pm 1.02}$	0.46 ± 0.07	0.10	0.08	0.16	0.08	whole sample
		$10^{-8.15 \pm 1.18}$	0.41 ± 0.08	0.08	0.08	0.17	0.08	non-CCC subsample
		$10^{-10.41 \pm 1.67}$	0.56 ± 0.11	0.24	0.16	0.17	0.09	CCC subsample
$\frac{Y_X}{M_\odot \text{keV}} E(z)$	$\frac{P_{r_{500}}}{\text{keV cm}^{-3}} E(z)^{-2}$	$10^{-8.32 \pm 1.88}$	0.35 ± 0.13	0.19	0.08	0.36	0.13	whole sample
		$10^{-8.47 \pm 2.10}$	0.36 ± 0.14	0.25	0.08	0.38	0.12	non-CCC subsample
		$10^{-8.47 \pm 3.45}$	0.37 ± 0.23	0.37	0.27	0.50	0.18	CCC subsample
$\frac{r}{r_{500}}$	$\frac{S}{\text{keV cm}^2} E(z)^{4/3} \left(\frac{T_{0.2-0.5r_{500}}}{10 \text{keV}} \right)^{-0.65}$	$10^{3.46 \pm 0.01}$	1.00 ± 0.03	—	—	—	—	whole sample
		$10^{3.46 \pm 0.02}$	0.99 ± 0.04	—	—	—	—	non-CCC subsample
		$10^{3.46 \pm 0.02}$	1.05 ± 0.04	—	—	—	—	CCC subsample

Here we provide both the mean scatter derived by a Gaussian fit to the histogram and the average scatter.

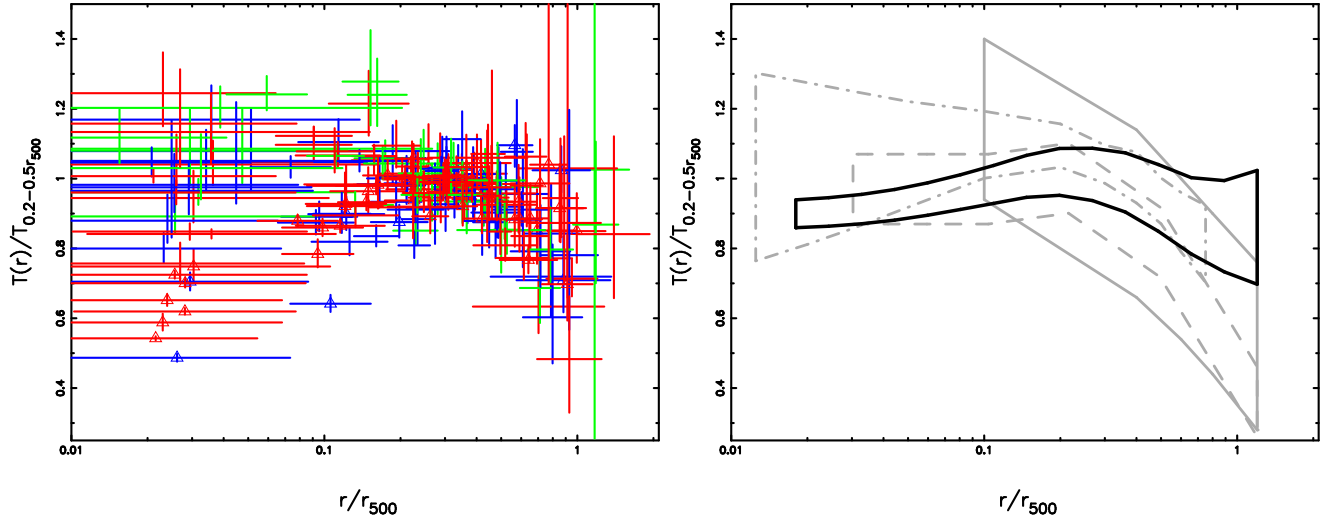


Fig. B.1. *Left:* Scaled radial temperature profiles for the sample. The CCCs are marked by triangles. The colors have the same meaning as those in Fig. 1. *Right:* An average temperature profile of the sample of 37 LoCuSS clusters (black, solid) compared to the temperature profile ranges in Markevitch et al. (1998, gray, solid), Vikhlinin et al. (2005, gray, dashed), and Pratt et al. (2007, gray, dash-dotted).

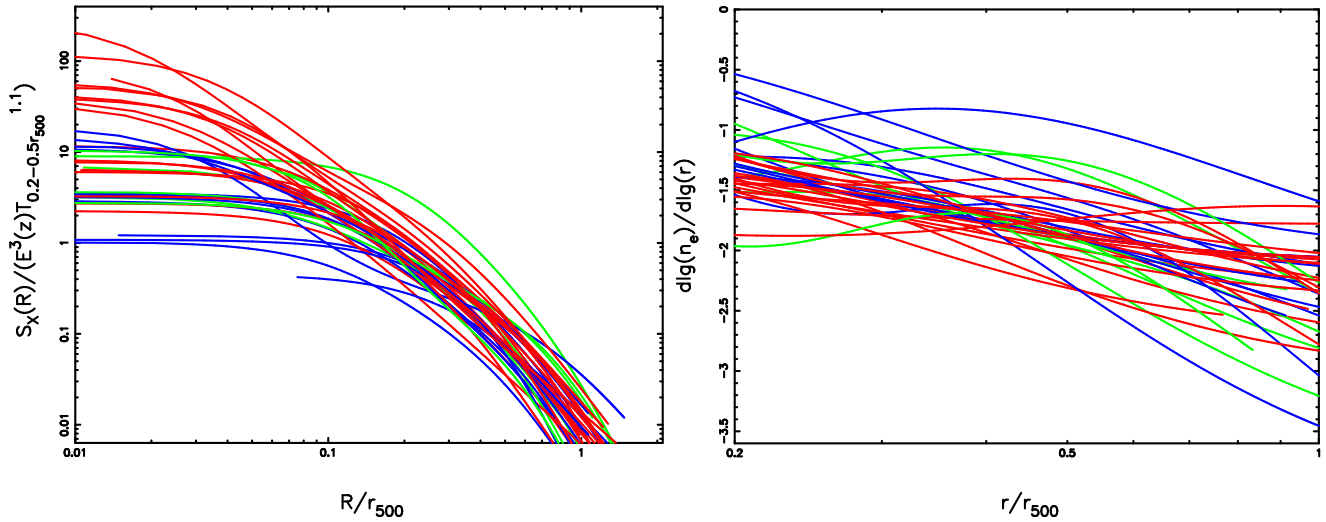


Fig. B.2. *Left:* Surface brightness profile fits scaled according to the empirical scaling, $S_X \propto T^{1.1}$. *Right:* Power law slope of the electron number density profiles. The colors have the same meaning as those in Fig. 1.

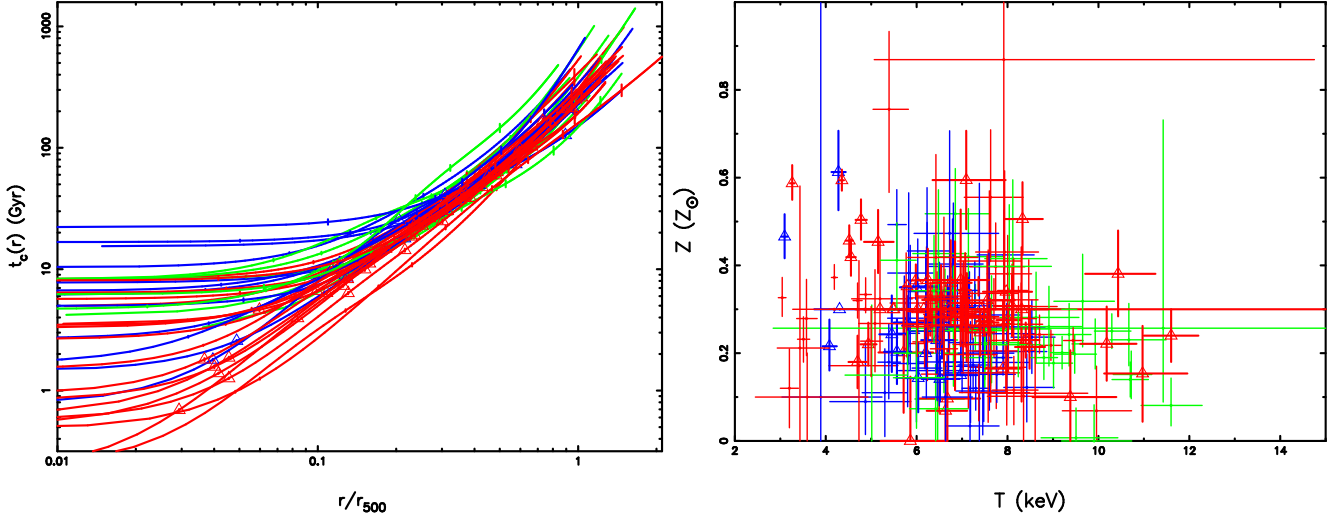


Fig. B.3. Cooling time profiles. The CCCs are marked by triangles. The colors have the same meaning as those in Fig. 1.

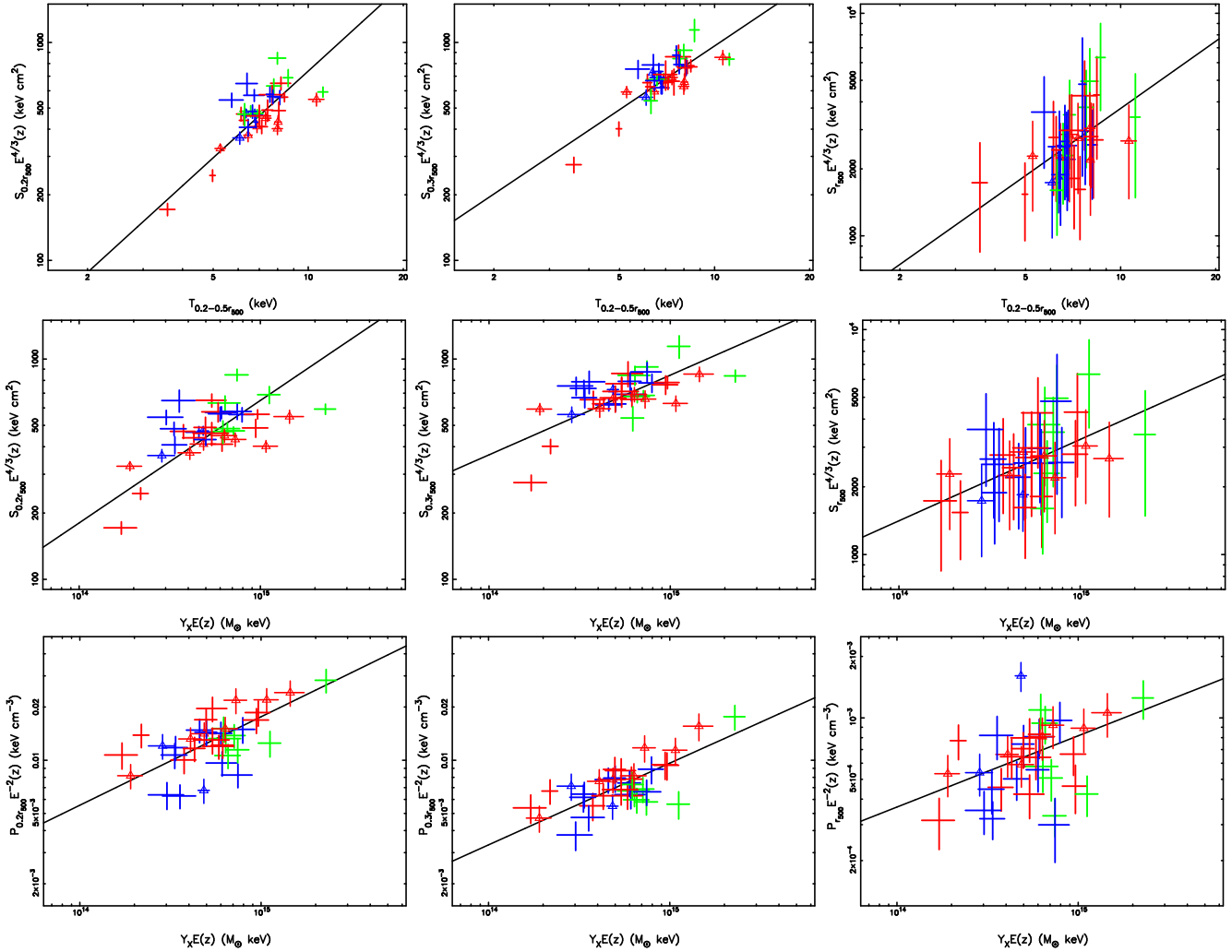


Fig. B.4. Entropy (upper and middle panels) and pressure (lower panels) versus temperature (upper panels) and X-ray analog of the SZ flux (middle and lower panels). The lines denote the best fit for our sample. The CCCs are marked by triangles. The colors have the same meaning as those in Fig. 1.

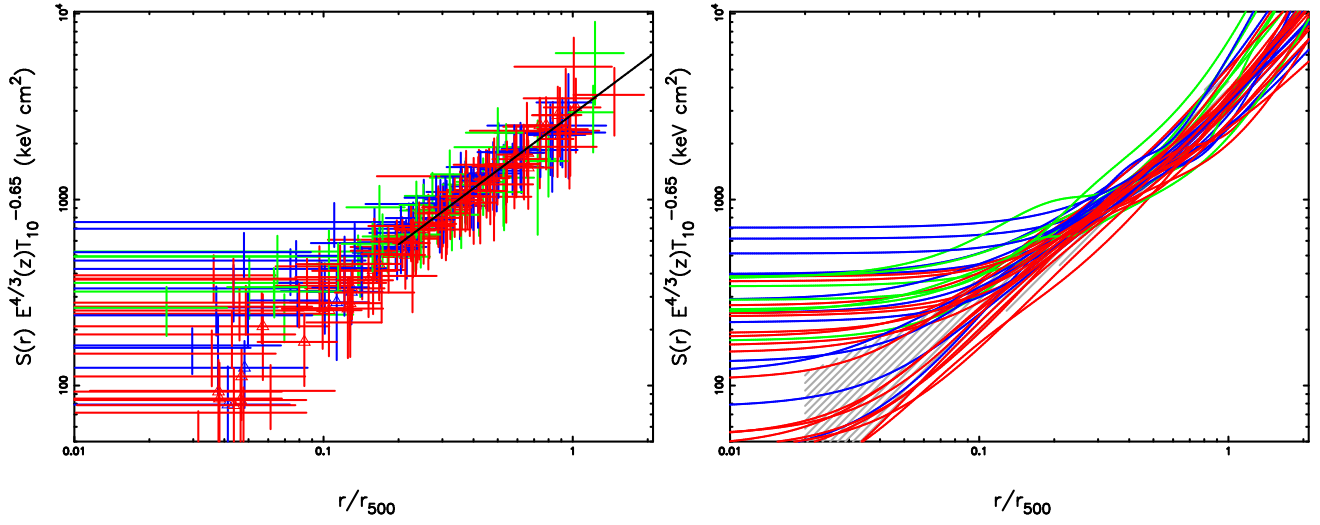


Fig. B.5. *Left:* Scaled entropy profiles for the sample and the combined best fit. *Right:* Scaled entropy profile fits for the sample compared to the sample in Pratt et al. (2006, gray, hatched). The CCCs are marked by triangles in the left panel. The colors have the same meaning as those in Fig. 1. T_{10} denotes $T_{0.2-0.5r_{500}}/10$ keV.

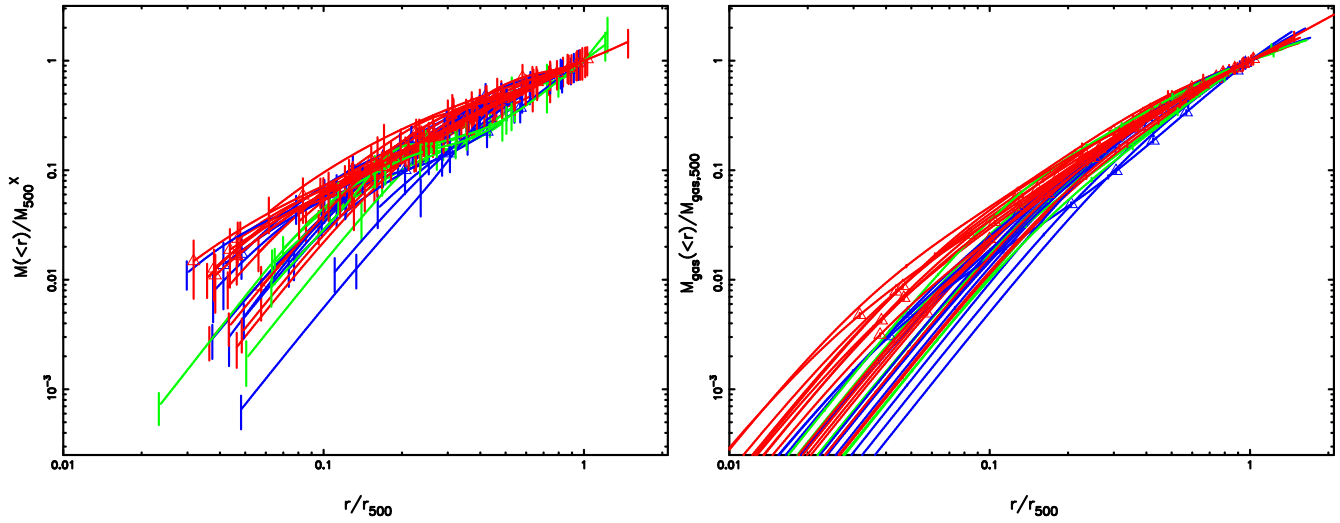


Fig. B.6. Scaled total mass profiles (left) and gas mass profiles (right). The CCCs are marked by triangles. The colors have the same meaning as those in Fig. 1. The error bars (a few per cent) of the gas mass profiles are too small to be seen in the right panel.

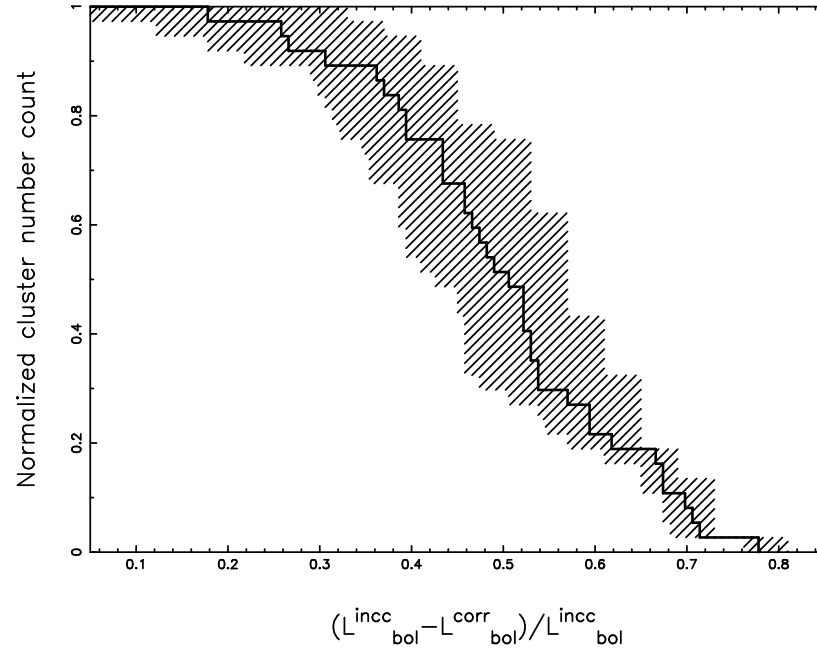


Fig. B.7. Normalized cumulative cluster number count as a function of the fraction of the total bolometric luminosity attributed to the $< 0.2r_{500}$ region.

Table C.1. Deduced properties of 37 LoCuSS galaxy clusters at the radii ($r_{500}^{Y_X, X}$) determined by the method described in § 4. Column (1): cluster name; Col. (2): $r_{500}^{Y_X, X}$; Cols. (3): X-ray mass at $r_{500}^{Y_X, X}$. Cols. (4–5): weak lensing masses at $r_{500}^{Y_X, X}$ for the D06 and B07 clusters.

Name	$r_{500}^{Y_X, X}$ Mpc	$M^X(r_{500}^{Y_X, X})$ $10^{14} M_\odot$	$M^{wl}(r_{500}^{Y_X, X})$ $10^{14} M_\odot$	
			D06	B07
RXCJ0043.4-2037	1.07	4.78 ± 1.40	—	—
RXCJ0232.2-4420	1.22	7.66 ± 2.20	—	—
RXCJ0307.0-2840	1.15	5.51 ± 2.01	—	—
RXCJ0516.7-5430	1.20	6.49 ± 1.83	—	—
RXCJ0528.9-3927	1.23	6.80 ± 1.98	—	—
RXCJ0532.9-3701	1.08	5.16 ± 1.51	—	—
RXCJ0547.6-3152	1.13	5.39 ± 1.60	—	—
RXCJ0645.4-5413	1.32	6.97 ± 2.07	—	—
RXCJ0658.5-5556	1.55	14.38 ± 6.07	—	—
RXCJ0945.4-0839	1.09	5.44 ± 1.57	—	—
RXCJ0958.3-1103	1.05	3.48 ± 1.02	—	—
RXCJ2129.6+0005	1.13	4.60 ± 1.34	5.51 ± 3.87	—
RXCJ2218.6-3853	1.09	4.59 ± 1.34	—	—
RXCJ2234.5-3744	1.26	7.44 ± 2.13	—	—
RXCJ2308.3-0211	1.19	7.05 ± 2.16	—	—
RXCJ2337.6+0016	1.18	8.41 ± 2.41	—	—
Abell68	1.16	6.20 ± 1.82	11.41 ± 8.49	4.68 ± 1.25
Abell115	1.31	5.79 ± 1.53	6.30 ± 3.99	—
Abell209	1.19	5.52 ± 1.74	8.41 ± 5.09	5.08 ± 1.29
Abell267	0.99	3.83 ± 1.16	7.53 ± 4.13	2.27 ± 0.92
Abell383	1.02	3.30 ± 0.97	—	2.95 ± 0.92
Abell773	1.28	7.84 ± 2.25	10.01 ± 5.14	—
Abell781	1.10	4.75 ± 1.39	7.69 ± 4.27	—
Abell901	1.00	3.27 ± 0.96	—	—
Abell963	1.16	5.28 ± 1.52	—	3.31 ± 0.57
Abell1413	1.23	5.63 ± 1.63	—	—
Abell1689	1.32	9.24 ± 2.69	—	11.54 ± 2.13
Abell1758	1.18	8.46 ± 2.55	13.34 ± 6.91	—
Abell1763	1.25	6.11 ± 1.77	7.64 ± 3.81	8.03 ± 1.66
Abell1835	1.36	8.43 ± 2.45	8.33 ± 4.17	13.41 ± 2.62
Abell1914	1.37	11.56 ± 3.30	7.40 ± 4.23	—
Abell2204	1.29	5.90 ± 1.69	7.76 ± 5.00	—
Abell2218	1.13	4.47 ± 1.36	—	6.63 ± 1.36
Abell2261	1.22	6.21 ± 1.76	6.09 ± 3.43	—
Abell2390	1.39	8.25 ± 2.41	9.56 ± 4.39	7.52 ± 1.56
Abell2667	1.24	6.31 ± 1.81	—	—
Z7160	1.04	2.85 ± 0.83	7.29 ± 4.46	—

“D06” denotes the clusters in the D06 subsample, and “B07” the B07 subsample, respectively. We used the error of M_{500}^{wl} as the error for the weak lensing masses here.

Table C.2. Deduced properties of 37 LoCuSS galaxy clusters at the radii ($r_{500}^{Y_X, \text{wl}}$) determined by the method described in § 6.2.3. Column (1): cluster name; Col. (2): $r_{500}^{Y_X, \text{wl}}$; Cols. (3): X-ray mass at $r_{500}^{Y_X, \text{wl}}$. Cols. (4–5): weak lensing masses at $r_{500}^{Y_X, \text{wl}}$ for the D06 and B07 clusters.

Name	$r_{500}^{Y_X, \text{wl}}$ Mpc	$M^X(r_{500}^{Y_X, \text{wl}})$ $10^{14} M_\odot$	$M^{\text{wl}}(r_{500}^{Y_X, \text{wl}})$ $10^{14} M_\odot$	
			D06	B07
RXCJ0043.4-2037	1.06	4.72 ± 1.40	—	—
RXCJ0232.2-4420	1.20	7.54 ± 2.20	—	—
RXCJ0307.0-2840	1.14	5.44 ± 2.01	—	—
RXCJ0516.7-5430	1.18	6.37 ± 1.83	—	—
RXCJ0528.9-3927	1.22	6.68 ± 1.98	—	—
RXCJ0532.9-3701	1.07	5.10 ± 1.51	—	—
RXCJ0547.6-3152	1.12	5.32 ± 1.60	—	—
RXCJ0645.4-5413	1.30	6.89 ± 2.07	—	—
RXCJ0658.5-5556	1.53	13.77 ± 6.07	—	—
RXCJ0945.4-0839	1.08	5.36 ± 1.57	—	—
RXCJ0958.3-1103	1.04	3.44 ± 1.02	—	—
RXCJ2129.6+0005	1.12	4.55 ± 1.34	5.45 ± 3.87	—
RXCJ2218.6-3853	1.08	4.53 ± 1.34	—	—
RXCJ2234.5-3744	1.24	7.34 ± 2.13	—	—
RXCJ2308.3-0211	1.18	6.96 ± 2.16	—	—
RXCJ2337.6+0016	1.17	8.28 ± 2.41	—	—
Abell68	1.15	6.13 ± 1.82	11.28 ± 8.49	4.64 ± 1.25
Abell115	1.29	5.68 ± 1.53	6.23 ± 3.99	—
Abell209	1.18	5.46 ± 1.74	8.33 ± 5.09	5.03 ± 1.29
Abell267	0.98	3.77 ± 1.16	7.45 ± 4.13	2.26 ± 0.92
Abell383	1.01	3.27 ± 0.97	—	2.92 ± 0.92
Abell773	1.27	7.72 ± 2.25	9.92 ± 5.14	—
Abell781	1.09	4.67 ± 1.39	7.59 ± 4.27	—
Abell901	0.99	3.24 ± 0.96	—	—
Abell963	1.15	5.21 ± 1.52	—	3.29 ± 0.57
Abell1413	1.22	5.57 ± 1.63	—	—
Abell1689	1.31	9.14 ± 2.69	—	11.43 ± 2.13
Abell1758	1.17	8.34 ± 2.55	13.19 ± 6.91	—
Abell1763	1.24	5.99 ± 1.77	7.56 ± 3.81	7.93 ± 1.66
Abell1835	1.35	8.34 ± 2.45	8.25 ± 4.17	13.25 ± 2.62
Abell1914	1.36	11.35 ± 3.30	7.34 ± 4.23	—
Abell2204	1.28	5.82 ± 1.69	7.67 ± 5.00	—
Abell2218	1.12	4.41 ± 1.36	—	6.58 ± 1.36
Abell2261	1.21	6.14 ± 1.76	6.04 ± 3.43	—
Abell2390	1.37	8.15 ± 2.41	9.46 ± 4.39	7.45 ± 1.56
Abell2667	1.23	6.23 ± 1.81	—	—
Z7160	1.03	2.82 ± 0.83	7.20 ± 4.46	—

“D06” denotes the clusters in the D06 subsample, and “B07” the B07 subsample, respectively. We used the error of M_{500}^{wl} as the error for the weak lensing masses here.

Table C.3. Deduced properties of 37 LoCuSS galaxy clusters at the radii ($r_{500}^{Y_{X,si}}$) determined by the method described in § 6.2.4. Column (1): cluster name; Col. (2): $r_{500}^{Y_{X,si}}$; Cols. (3): X-ray mass at $r_{500}^{Y_{X,si}}$. Cols. (4–5): weak lensing masses at $r_{500}^{Y_{X,si}}$ for the D06 and B07 clusters.

Name	$r_{500}^{Y_{X,si}}$ Mpc	$M^X(r_{500}^{Y_{X,si}})$ $10^{14}M_{\odot}$	$M^{wl}(r_{500}^{Y_{X,si}})$ $10^{14}M_{\odot}$	
			D06	B07
RXCJ0043.4-2037	1.15	5.21 ± 1.52	—	—
RXCJ0232.2-4420	1.30	8.39 ± 2.42	—	—
RXCJ0307.0-2840	1.23	6.02 ± 2.16	—	—
RXCJ0516.7-5430	1.29	7.24 ± 2.04	—	—
RXCJ0528.9-3927	1.33	7.67 ± 2.21	—	—
RXCJ0532.9-3701	1.15	5.53 ± 1.62	—	—
RXCJ0547.6-3152	1.21	5.84 ± 1.73	—	—
RXCJ0645.4-5413	1.42	7.54 ± 2.23	—	—
RXCJ0658.5-5556	1.69	18.47 ± 6.80	—	—
RXCJ0945.4-0839	1.17	6.02 ± 1.73	—	—
RXCJ0958.3-1103	1.13	3.75 ± 1.09	—	—
RXCJ2129.6+0005	1.21	4.97 ± 1.44	5.89 ± 3.87	—
RXCJ2218.6-3853	1.17	4.97 ± 1.45	—	—
RXCJ2234.5-3744	1.35	8.11 ± 2.31	—	—
RXCJ2308.3-0211	1.28	7.65 ± 2.32	—	—
RXCJ2337.6+0016	1.26	9.26 ± 2.67	—	—
Abell68	1.24	6.71 ± 1.97	12.27 ± 8.49	4.98 ± 1.25
Abell115	1.42	6.51 ± 1.73	6.77 ± 3.99	—
Abell209	1.27	5.97 ± 1.82	8.98 ± 5.09	5.43 ± 1.29
Abell267	1.06	4.25 ± 1.27	8.08 ± 4.13	2.40 ± 0.92
Abell383	1.10	3.53 ± 1.03	—	3.18 ± 0.92
Abell773	1.38	8.76 ± 2.52	10.71 ± 5.14	—
Abell781	1.19	5.19 ± 1.53	8.30 ± 4.27	—
Abell901	1.07	3.51 ± 1.03	—	—
Abell963	1.24	5.75 ± 1.65	—	3.47 ± 0.57
Abell1413	1.33	6.07 ± 1.75	—	—
Abell1689	1.41	9.97 ± 2.91	—	12.29 ± 2.13
Abell1758	1.26	9.33 ± 2.80	14.35 ± 6.91	—
Abell1763	1.35	6.93 ± 1.99	8.18 ± 3.81	8.71 ± 1.66
Abell1835	1.46	9.08 ± 2.59	8.86 ± 4.17	14.53 ± 2.62
Abell1914	1.47	13.04 ± 3.74	7.87 ± 4.23	—
Abell2204	1.39	6.35 ± 1.81	8.27 ± 5.00	—
Abell2218	1.21	4.88 ± 1.48	—	6.99 ± 1.36
Abell2261	1.32	6.74 ± 1.95	6.51 ± 3.43	—
Abell2390	1.49	8.88 ± 2.58	10.20 ± 4.39	7.95 ± 1.56
Abell2667	1.33	6.82 ± 1.95	—	—
Z7160	1.12	3.08 ± 0.88	7.85 ± 4.46	—

“D06” denotes the clusters in the D06 subsample, and “B07” the B07 subsample, respectively. We used the error of M_{500}^{wl} as the error for the weak lensing masses here.

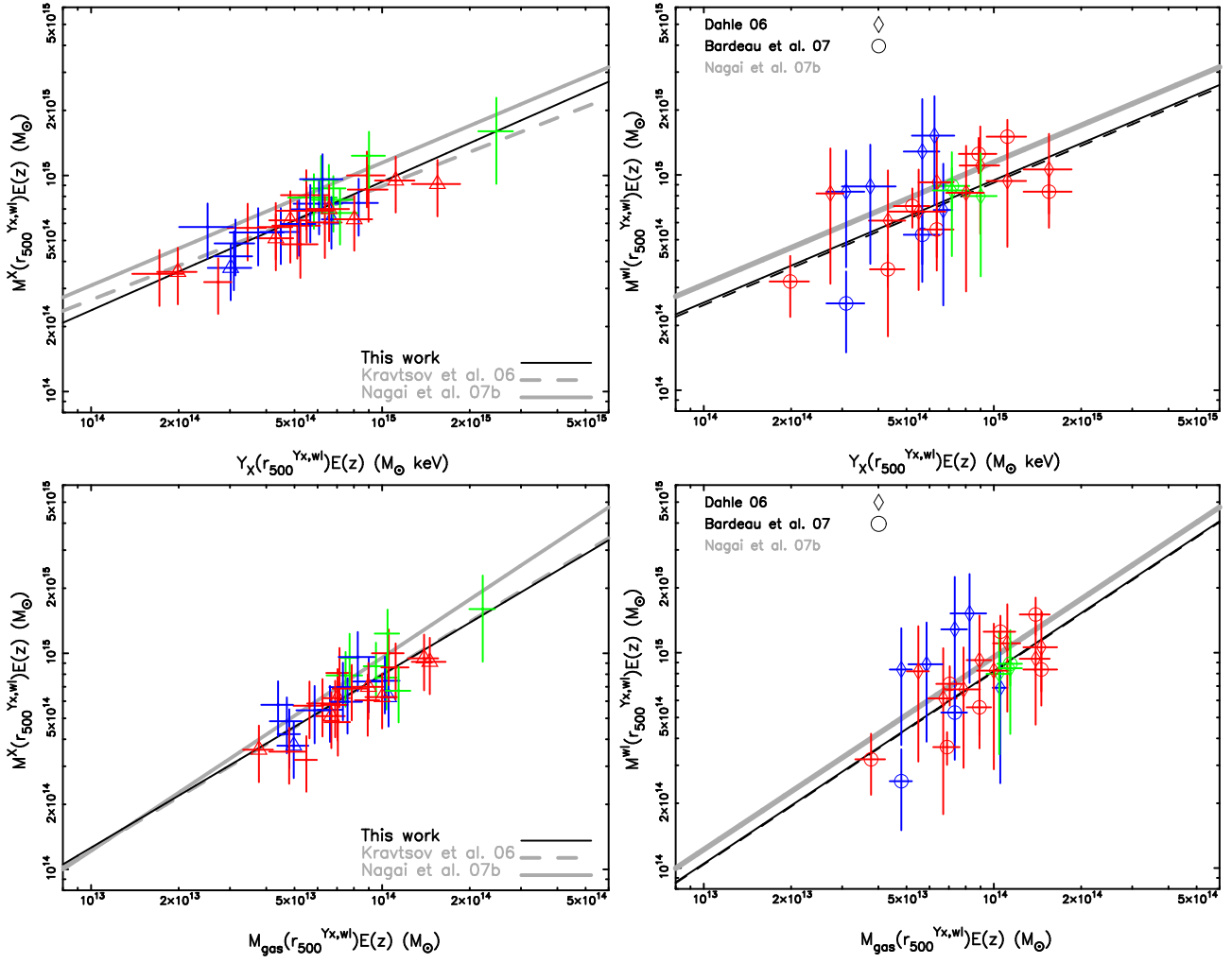


Fig. C.1. See caption in Fig. 5 except that the radius ($r_{500}^{Y_X, wl}$) is determined by the method described in § 6.2.3.

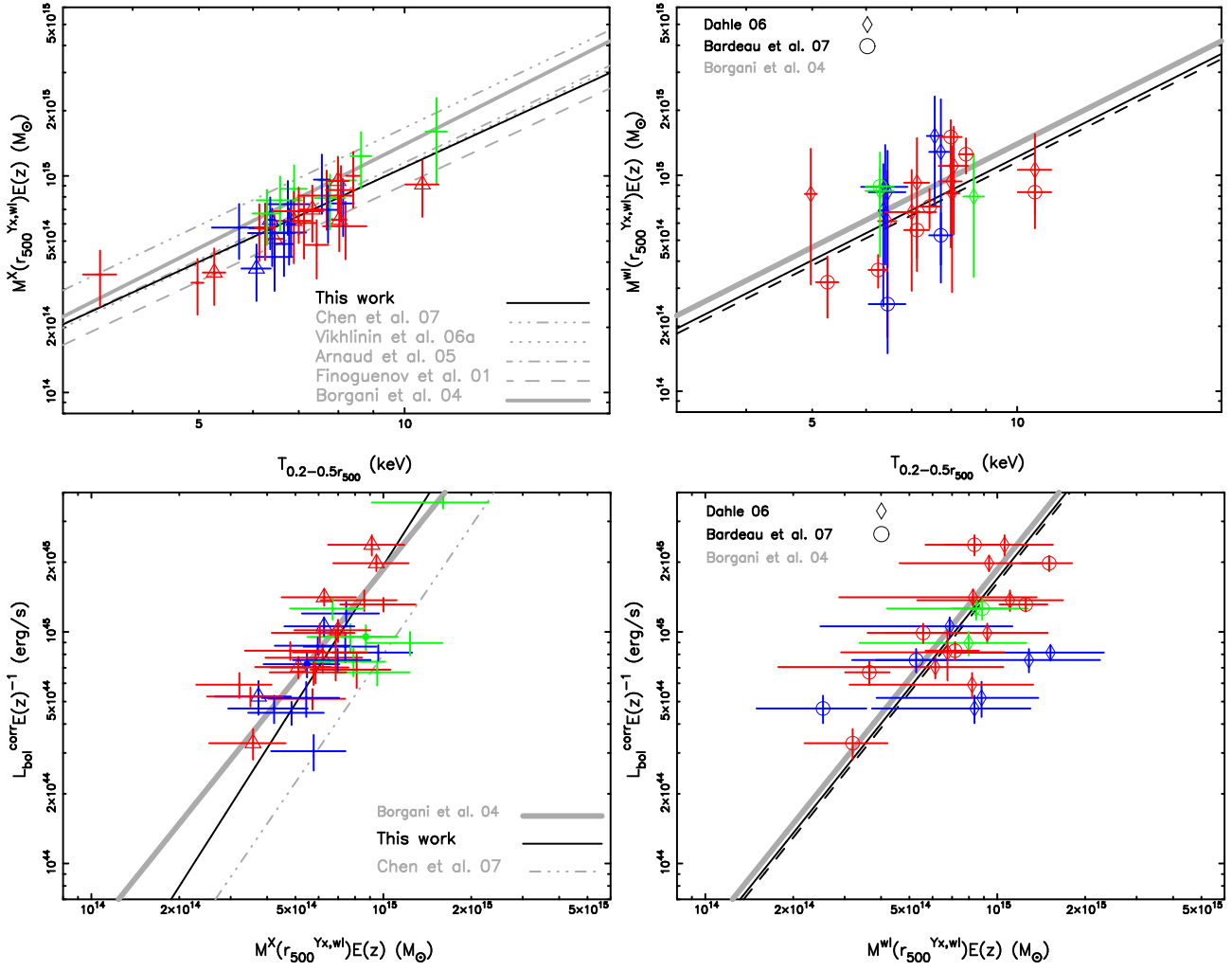


Fig. C.2. See caption in Fig. 6 except that the radius ($r_{500}^{Yx,wl}$) is determined by the method described in § 6.2.3.

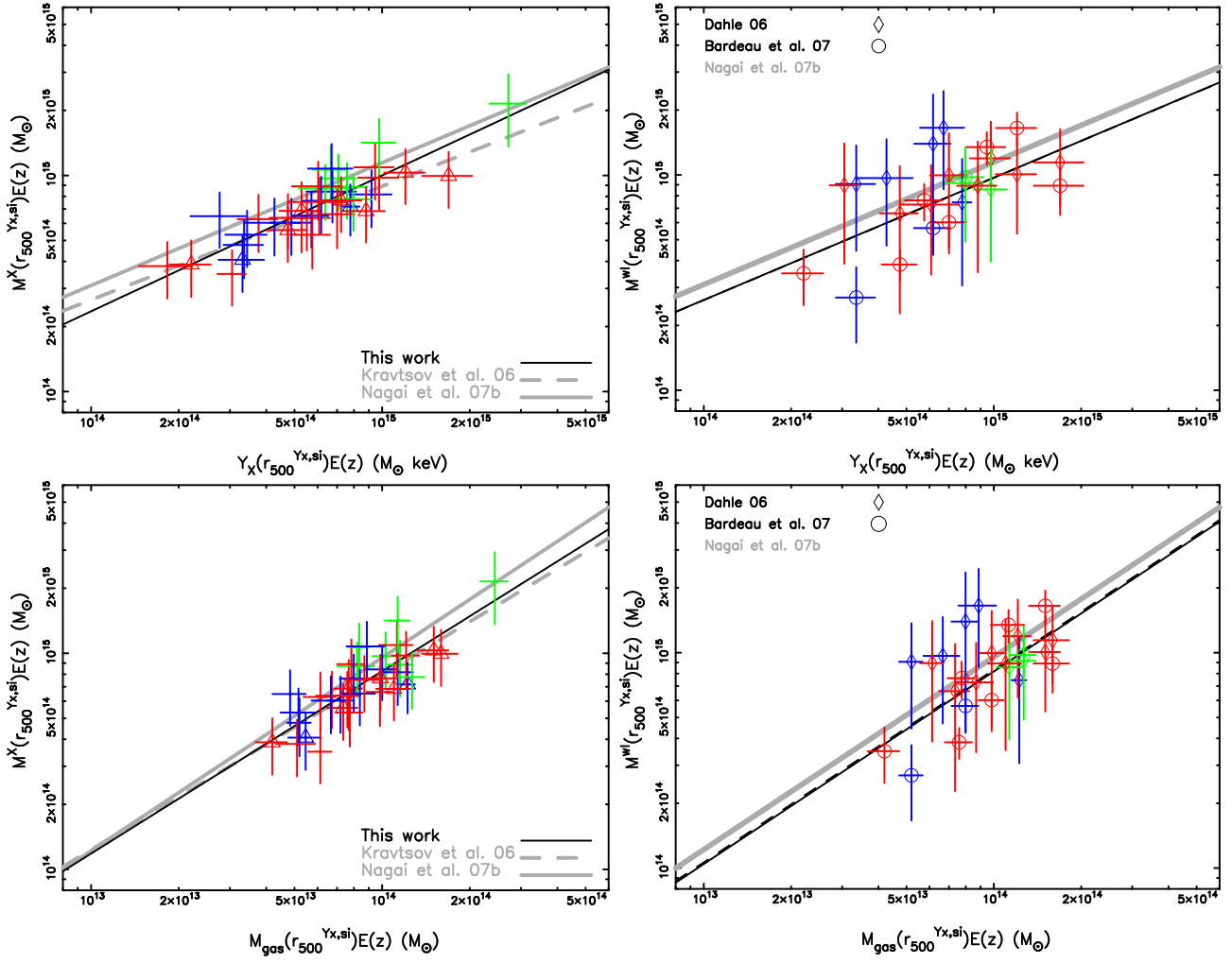


Fig. C.3. See caption in Fig. 5 except that the radius ($r_{500}^{Y_{X,si}}$) is determined by the method described in § 6.2.4 but combining the $Y_X(r)$ profile and the $M-Y_X$ relation from simulations in Nagai et al. (2007b).

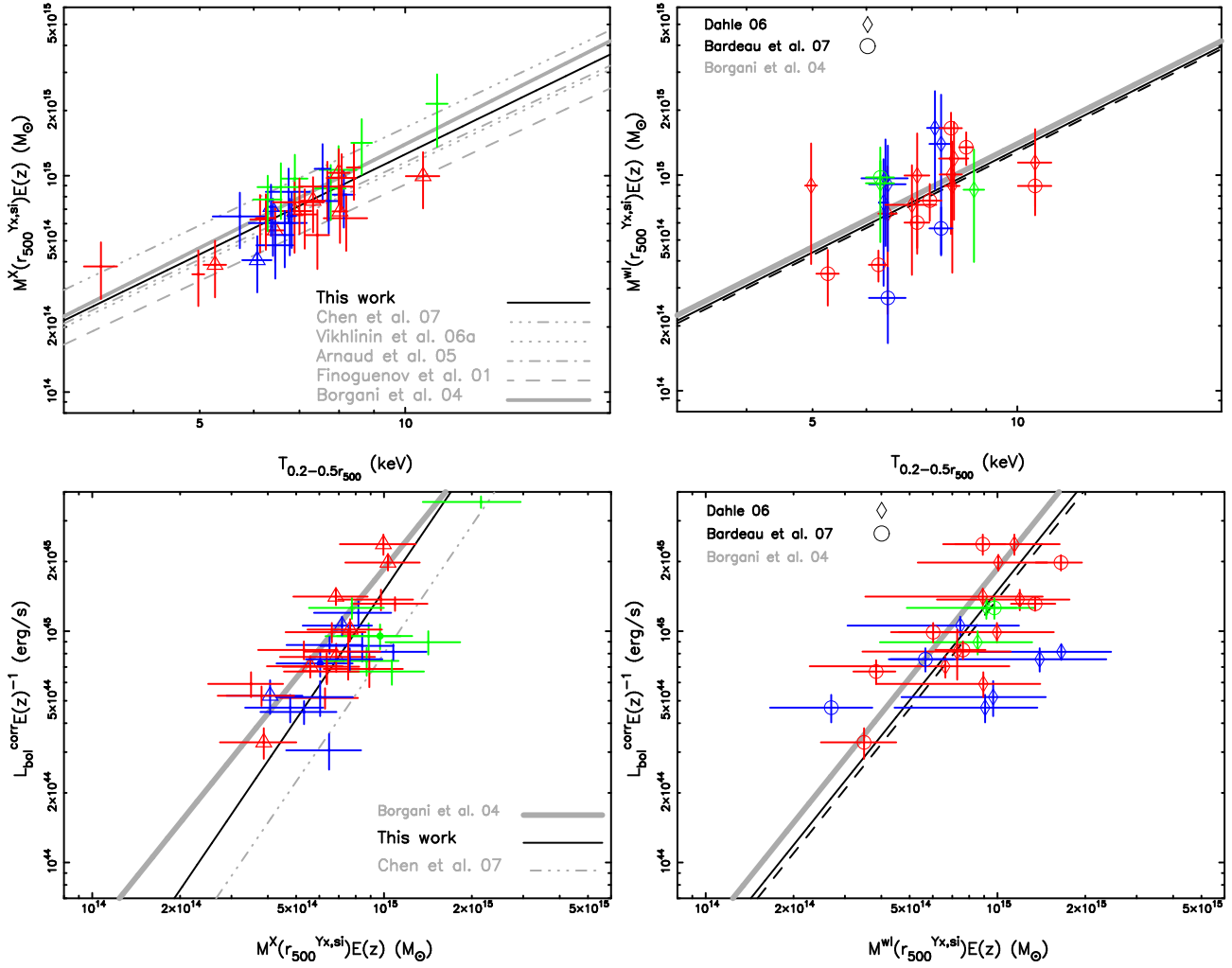


Fig. C.4. See caption in Fig. 6 except that the radius ($r_{500}^{Y_{X,si}}$) is determined by the method described in § 6.2.4 but combining the $Y_X(r)$ profile and the M - Y_X relation from simulations in Nagai et al. (2007b).

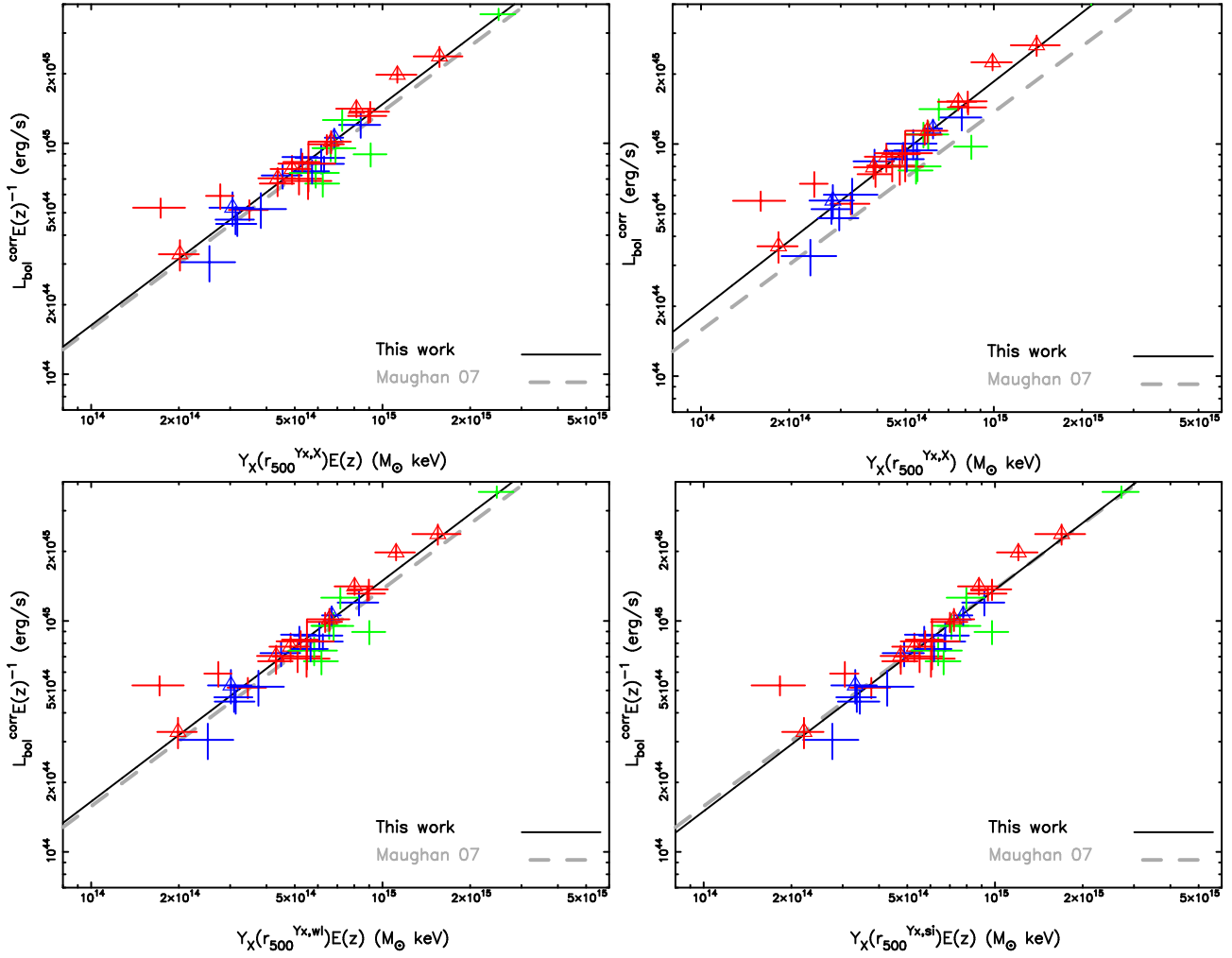


Fig. C.5. Luminosity– Y_X relation. The CCCs are marked by triangles. The clusters appearing “primary with small secondary” or “off-center” morphology are in green, appearing “elliptical” or “complex” morphology are in blue, and appearing “single” morphology are in red using the classification in Jones & Forman (1992). The Y_X parameters are measured at $r_{500}^{Y_X,X}$ in the upper panels, at $r_{500}^{Y_X,wl}$ in the left lower panel, and at $r_{500}^{Y_X,sl}$ in the right lower panel. In § 4, § 6.2.3 and § 6.2.4, we gave the description of the derivation of the radius by combining the $Y_X(r)$ profile and the M – Y_X relation.